ON-CHIP MICRORESONATOR FREQUENCY COMBS: GENERATION DYNAMICS, POWER TRANSFER, AND TIME-DOMAIN CHARACTERIZATION

A Dissertation

Submitted to the Faculty

of

Purdue University

by

Pei-Hsun Wang

In Partial Fulfillment of the

Requirements for the Degree

of

Doctor of Philosophy

May 2016

Purdue University

West Lafayette, Indiana

For my family and those who have been in part of my life

ACKNOWLEDGMENTS

I would like to thank my advisor, Professor Andrew M. Weiner, for his guidance. With his inspiration and support, I was able to conducted high-impact research during my time at Purdue. Prof. Weiner instructed me in a thoughtful way without constraining my ideas and opinions. I would also like to thank Dr. Daniel E. Leaird for his prompt technical support and suggestions and also thank Professor Minghao Qi for his collaboration on this work.

I could not accomplish this work without support from my colleagues, both in Ultrafast Optics and Optical Fiber Communication Laboratory and Prof. Qi's group. I would like to acknowledge Dr. Xiaoxiao Xue, Dr. Fahmida Ferdous, Dr. Yang Liu, Dr. Andrew J. Metcalf, Steve Chen, Jose A. Jaramillo-Villegas, Abdullah Al Noman Ovi, and Cong Wang for their valuable discussion, ideas, and support. I would also like to thank Dr. Yi Xian, Dr. Houxun Miao (NIST), Dr. Li Fan, Dr. Leo T. Varghese, Dr. Jian Wang, Ben Niu, and Kyunghun Han for silicon nitride microring fabrication and device preparation.

I also thank Dr. Joseph Lukens and Amir Rashidinejad, fellow students who joined the group with me the same time in Fall 2011. They shared life experience and relieved my initial stress as an international student. I especially thank Joseph, as an office mate who stayed with me in the same office for the most of time during my PhD study and gave me opportunities to practice English. I was fortunate to work with all other members of Prof. Weiner's group since Fall 2011 as well, especially Prof. Victor Torres-Company, Dr. Hyoung-Jun Kim, Dr. Rui Wu, Dr. Amir Dezfooliyan, Dr. Dennis Lee, Dr. Yihan Li, Justin Wirth, Bohao Liu, Ogaga D. Odele, Poolad Imany, Oscar Sandoval, Eric Topel, and Keith McKinzie. I would like to thank my committee members, Professor Evgueni E. Narimanov and Professor Peter Bermel,

for their suggestions on both my preliminary and final examinations. I also thank Dee Dee Dexter for her diligent help making meetings and travel possible.

I thank my family, especially my mother Shengkang, for their love and continuous support. My special thanks go to my girlfriend, Fangling, for her love and accompany even at my worst. Finally, I thank my friends and those who have been in part of my life. They shaped and made me who I am.

Pei-Hsun Wang

West Lafayette, Indiana

January 2016

TABLE OF CONTENTS

Page

Page

LIST OF TABLES

LIST OF FIGURES

Figure Page

Figure Page

Figure Page

ABSTRACT

Wang, Pei-Hsun Ph.D., Purdue University, May 2016. On-chip Microresonator Frequency Combs: Generation Dynamics, Power Transfer, and Time-domain Characterization. Major Professor: Andrew M. Weiner.

Over the last two decades, optical frequency combs from a mode-locked laser have been used as a ruler in frequency domain for extremely precise measurements. With a series of peaks equally spaced in optical frequency, it gives a significant improvement on the increasing demands of optical frequency metrology, telecommunication, optical clocks and measurements on the atomic level. However, optical frequency combs, based on fiber or free-space optics, are now restricted by further downsizing the optical paths and therefore, with these conventional combs, it is hard to achieve a repetition rate in radio frequencies ranging from several tens GHz to THz.

Recently, high-quality (Q) microresonators offer the potential for on-chip comb generation with a repetition rate from tens GHz to several THz. These frequency combs may also support the generation of octave-spanning comb spectra in compact and chip-level devices. This novel Kerr comb technology benefits the developments of integrated photonics. Here, in this thesis, the author discusses the microresonator-based frequency combs from silicon nitride waveguide microrings. Owing to its compatibility with CMOS-compatible fabrication process and large Kerr nonlinearity, silicon nitride has attracted considerable attention for on-chip comb generation.

The thesis is organized as follows: Chapter 1 gives brief reviews of optical frequency combs and the properties of silicon nitride waveguide resonators. In Chapter 2, on-chip comb generation and the properties of the generated combs, including communication performance, intensity noise, and time-domain characterization, are investigated. A drop-port study and power transfer in microrings are presented in

Chapter 3. The comb-enhanced coupling, comb threshold, and comb efficiency at the through port are also discussed. In Chapter 4, the author compares the comb generation in both normal and anomalous cavity dispersion. Time-domain autocorrelation measurements will be demonstrated to characterize the comb generation in different dispersion regimes. In Chapter 5, the mode-locking transition and soliton formation in anomalous dispersion regime will be discussed. A short, bright, and close to transform-limited pulse is identified in time with a drop-port geometry. Finally, a summary is given in Chapter 6.

1. INTRODUCTION

1.1 Optical Frequency Comb

Optical frequency combs consist of a series of multiple, discrete frequency components with an equal spacing in optical spectra. This precise distance in frequency provides prominent advantages for applications including broadband sensing [1–3], optical frequency metrology [4–6], precision measurements [7], and short pulse generation [8]. Previously, there are several mechanisms to generate optical frequency combs. First, through the stabilization of a pulse train generated by a mode-locked laser, frequency combs could be self-referenced to have stabilized frequency with repetition rate typically below $\approx$ 3 GHz [9]. In another way, based on strong phase modulation driven by a radio frequency (RF) waveform, frequency combs with higher repetition rate (mostly in the range of a few tens of GHz) could be initiated from a continuous-wave (CW) laser [10–13].

Each mode of a frequency comb could be described by the following equation [4]:

$$f_m = m f_{rep} + f_{ceo} \tag{1.1}$$

where f_{rep} is the repetition rate of the laser cavity and f_{ceo} is the carrier envelope offset frequency, whose value is typically selected to obey $f_{ceo} < f_{rep}$ in order to deterministically choose the mode number m. Figures 1.1 show the schematic diagrams for a comb source from a mode-locked laser. In Fig. 1.1(a), the blue trace stands for the optical spectrum of a mode-locked laser with a Gaussian envelope where f_{rep} is the repetition rate determined by the cavity length. The absolute frequency of each line from the mode-locked laser is offset from the multiples of the repetition rate by the carrier envelope offset frequency (f_{ceo}). The corresponding time-domain behavior is shown in Fig. 1.1(b). The period of the time-domain waveform is then determined by the laser repetition rate (f_{rep}).

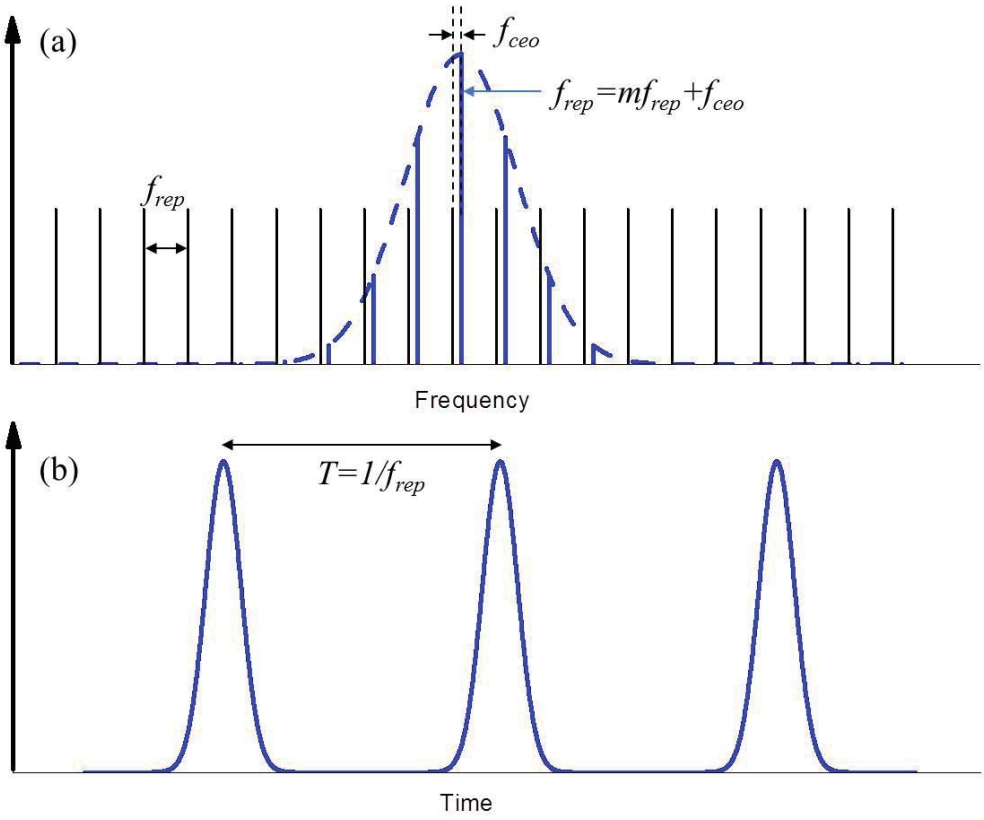

Fig. 1.1. Schematic diagrams for an ideal comb source. (a) The mode-locked laser with Gaussian spectrum. (b) The corresponding time-domain intensity.

1.2 Microresonator-based Comb Sources

On-chip resonators with high-Q resonances have been demonstrated since 2003 [14]. The circulation of the electromagnetic field enables storage of optical power at a cavity resonance and leads to a wide range of applications. Recently, thanks to the techniques of micro-fabrication and micro-lithography, optical frequency combs have been studied with different geometries, such as toroidal microresonators, disk resonators, crystalline resonators, and waveguide-ring resonators. These compact comb sources have received considerable attention since 2007 [15]. Tuning a CW laser into a cavity resonance leads to build-up of intracavity power, resulting in parametric gain that enables additional cavity modes to oscillate based on nonlinear optical modulation. Microresonator-based frequency combs have also been demonstrated in a variety of materials, including silica [15–19], calcium fluoride [20–22], magnesium fluoride [23–25], fused quartz [26], and silicon nitride [27–31]. Recent demonstrations [18, 27] of comb generation from planar microresonators fabricated on chips using standard microlithography offer possibilities for on-chip comb applications, such as on-chip pulse generation and optical communications. In addition, the repetition rates of these devices, typically ranging from few GHz to THz [32], complement the unreachable regime for the conventional combs from mode-locked lasers. For practical applications, the most interesting frequency regime would be around several tens of GHz corresponding to the high frequency range used in current optical communication. Last, the microresonator-based combs also provide a possible path to spectrally broaden the comb spectrum to an octave [19, 32].

1.3 Silicon Nitride Waveguide Resonators

Integrated photonics chips, which are typically compact, small, and low-cost, generate and transfer optical signals directly on chips. It offers a convenient way for developing future telecommunications and optical interconnects. Although previously silicon-on-insulator platform, where a silicon layer is on top of an insulator layer

(silicon oxide, SiO_2), works as a leading approach for both linear and nonlinear optical devices [33], its high two-photon absorption in silicon at the telecommunication wavelengths results in high nonlinear absorption and therefore limits its developments in nonlinear optics [34]. For telecommunication band, silicon nitride (Si_3N_4) is a promising candidate as a nonlinear photonics material. First, silicon nitride is a CMOS-compatible material, which could be directly applied in the current semiconductor industry. Second, its large bandgap ($\approx$ 5 eV) results in very low nonlinear absorption. Last, comparing with silica, silicon nitride offers larger Kerr nonlinearity (n_2) which is a factor of ten greater than silica [34]. The refractive index of silicon nitride is close to $n = 2$ at 1550 nm with a nonlinear parameter γ =1.09 to 1.40 $W^{-1}m^{-1}$ [34, 35].

Figure 1.2(a) shows the microscope image of a 40 μm radius silicon nitride microresonator with the bus-waveguide. The schematic cross-section of the waveguide is plotted in Fig. 1.2(b). The silicon nitride waveguide is deposited on top of the insulator layer (SiO_2) residing on a silicon substrate, and the top of the waveguide is covered by a thin SiO_2 layer for protection.

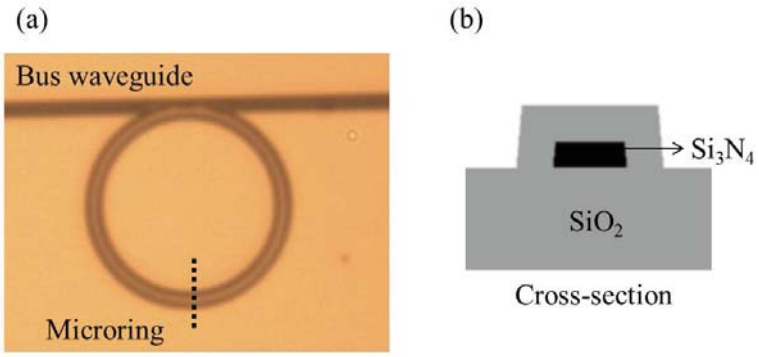

Fig. 1.2. (a) Microscope image of a 40 μm radius silicon nitride microresonator with a bus-waveguide. (b) The schematic diagram of the waveguide cross-section.

1.4 Organization of the Thesis

The thesis is organized as follows: The on-chip comb generation and its properties are first discussed in Chapter 2. The correlation between communication performance, intensity noise, and time-domain characterization will be given under different routes to comb formation [36].

A drop-port study and its applications are presented in Chapter 3. In sharp contrast to most of the previous microresonator studies, where a strong overlapping pump line is typically observed in the through-port spectra [23, 27, 28, 30, 32], the author shows a smooth comb spectrum by utilizing a drop-port waveguide [37]. In addition, field information internal to the ring could be well identified using this drop geometry. Furthermore, a pump saturation behavior for comb generation is identified in microrings while the power transfer between the microring and the bus-waveguide is studied in the presence of comb generation. To further engineer the coupling and improve the comb efficiency, an over-coupled device is also utilized. With the aid of the comb-enhanced coupling, a spectrum where the power of the pump line is weaker than that of the adjacent combs is, for the first time, observed at the through-port spectrum. The comb efficiency at the through-port spectrum is estimated up to $\approx$ 95%. Furthermore, a simple model is used to study the coupling and efficiency in the presence of comb generation.

In Chapter 4, the author compares the comb generation in both normal and anomalous cavity dispersion. Previously, most theories discussing conditions for comb formation are based on a modulational instability analysis assuming a microresonator characterized by anomalous dispersion. In the time-domain measurements, both analytical and simulation studies show the formation of single soliton coupled to a continuous background field inside the resonator [35, 38]. On the other hand, in normal dispersion, a few recent studies discuss comb generation in microresonators through the freedom of pump detuning or interactions with other mode families. Excitation of dark pulse solutions has been demonstrated both experimentally and in simula-

tion [39]. Here, the author demonstrated coherent comb formation in both anomalous and normal dispersion regime. A bright short pulse could be directly formed in the normal dispersion cavity while in anomalous dispersion, a mode-locked transition is identified with complex waveform in the cavity [37].

In Chapter 5, the mode-locking transition and soliton initiation process will be discussed in anomalous dispersion regime. Through the pump detuning or modulation, it is possible to transition a noisy comb into the noise-free regime. Several previous works demonstrated the possibility to kick soliton in microresonator-based frequency comb generation [35, 38, 40]. Here, a correlation between the noise transition and the spectral properties of the transmission will be investigated. In addition, broadband and smooth combs with a short pulse in time could be observed in the anomalous regime with deterministic spectral phase after low-noise transition. With a drop-port geometry, both the efficiency of the intracavity power transfer and the CW background field in the single soliton regime can be identified. In addition, the drop-port spectrum aids in studying the time-domain waveform in the microring and provides information of the spectral phase and CW background for the pump line.

A summary will be given in Chapter 6.

2. CHARACTERIZATION OF ON-CHIP COMB GENERATION

2.1 Introduction

For microresonator-based frequency combs, initial studies focused on characterizing the properties of the generated optical spectra, including the optical bandwidth and the uniformity of the frequency spacing. Recently, more attention has been devoted to other properties of the generated combs. For example, intensity noise has been characterized both in the vicinity of RF tones generated through the beating of comb lines on a photodetector [26, 30, 41] and also at baseband [31]. In addition, pulse shaping experiments provided insight looking into the time-domain behaviors and especially the coherence of the generated comb [26, 28, 42], which is essential for on-chip pulse operation. In this chapter, a correlation between the route to comb formation, coherence, intensity noise, and communication performance of Kerr combs will be discussed [36]. This helps us to establish a model how to select or design microresonators for desirable comb operation.

2.2 Experimental Setup

As in the previous studies [28, 42], a tunable CW laser is amplified and launched into a ring resonator fabricated with silicon nitride waveguides. The parametric gain results in the generation of multiple frequency components (a frequency comb) through cascaded four-wave mixing (FWM). Figure 2.1 shows the schematic diagram of the experimental setup for comb characterization.

The amplified optical pump is coupled into and out of the bus-waveguide through a pair of lensed fibers. By carefully tuning the wavelength of the CW laser, the optical

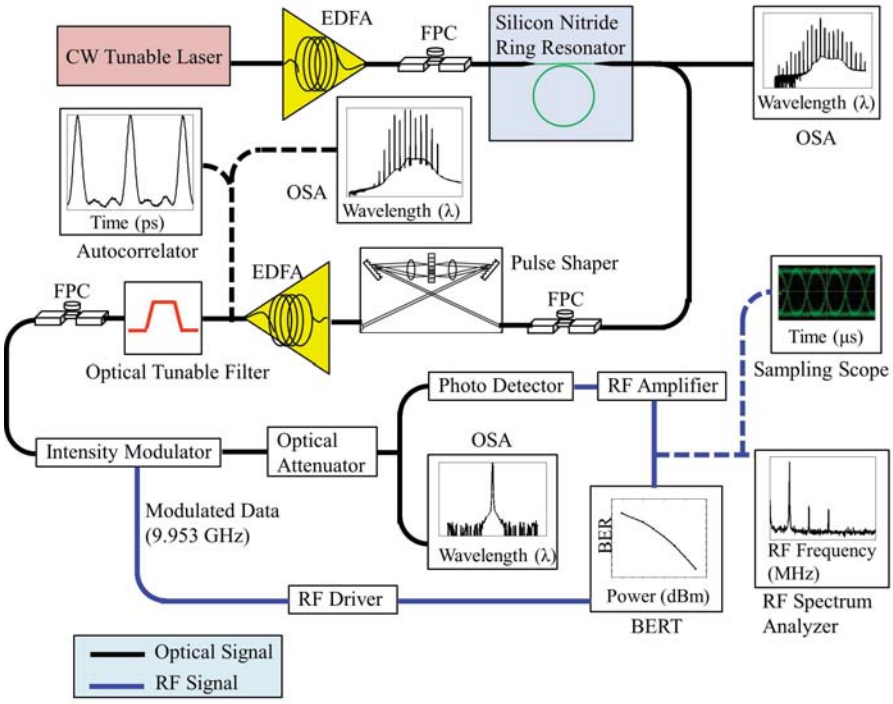

Fig. 2.1. Schematic diagram of the experimental setup. CW: continuous-wave; RF: radio-frequency; EDFA: erbium-doped fiber amplifier; FPC: fiber polarization controller; OSA: optical spectrum analyzer; BERT: bit error rate tester.

power resonated in the ring and initiated frequency combs. A programmable pulse shaper is placed directly after the resonator, playing an important role in each set of experiments discussed later. For characterization of intensity noise and communication performance, the pulse shaper simply works as a filter and selects an individual line out of the generated comb, blocking the others. The power of the selected line is then boosted by an erbium-doped fiber amplifier (EDFA), which then passes through a tunable filter with 0.4 nm bandwidth to suppress amplified spontaneous emission (ASE) noise. The output is detected by a photodiode with 12 GHz bandwidth and amplified by an RF amplifier with 500 MHz bandwidth, after which the low frequency intensity noise is characterized by an RF spectrum analyzer. On-off keying (OOK) communication experiments are performed by modulating each selected comb line at 9.953 Gbit/s using a lithium niobate intensity modulator driven by a length $2^{31} - 1$ non-return-to-zero pseudo-random binary sequence (PRBS). The photodetected output is connected to a bit error rate tester (BERT) for error analysis and a sampling oscilloscope with bandwidth 60 GHz for display of eye diagrams. Eye diagrams and bit error rate data are reported only for filtered comb lines with optical signal to noise ratio (OSNR)$\geq$15 dB (based on 0.1 nm OSA spectral resolution) in the following demonstrations. This ensures that any degradation of the communication results is associated with the inherent properties of selected comb lines themselves as opposed to poor OSNR.

To provide information on the coherence, the pulse shaper manipulates the spectral phase of generated combs on a line-by-line basis in an attempt to achieve pulse compression [28, 42]. In these experiments, the pulse shaper may be also used to attenuate the pump line, which often remains very strong, to a level comparable to the neighboring lines. This strong power detected at the through port of the device may be related to the coupling condition between the bus-waveguide and the ring or the intrinsic spectral properties of the combs internal to the ring. The optical output after the pulse shaper is amplified and connected to an intensity autocorrelator based on second harmonic generation (SHG) in a noncollinear, background-free

geometry. The dispersion of the fibers connecting the microresonator chip and the autocorrelator is left uncompensated in this chapter. The pulse shaper varies the spectral phase one line at a time in order to maximize the second harmonic signal at zero delay [28, 42]. Autocorrelation traces are then recorded as a function of time delay. Experimental autocorrelations are compared with those calculated on the basis of the measured comb spectra with the assumption of flat spectral phase. In these time-domain measurements, high quality pulse compression showing good agreement between experimental and calculated autocorrelation traces provides evidence of stable spectral phase and good coherence.

2.3 Microresontor-based Comb Generation

2.3.1 Routes to Comb Formation

In previous time-domain studies, pulse shaping, compression, and autocorrelation measurements on combs from microresonators were performed to identify the coherence of the generated micro-combs [26,28,42]. Two distinct routes to comb formation are identified [28, 30, 42]. Figures 2.2 show the schematic diagrams for micro-comb formation. In one case, which is termed Type I formation (as shown in Fig. 2.2(a)), the cascaded FWM proceeds from initial sidebands spaced by one free spectral range (FSR) as the intracavity pump reaches the comb generation threshold. In the second case (as shown in Fig. 2.2(b)), the initial pair of sidebands is generated with N-FSR spacing from the pump, where N is an integer greater than one. Cascaded FWM then results in a comb with N-FSR frequency spacing. In both cases the process is expected to produce frequency spacing that is precisely equal across the comb, resulting in high temporal coherence as that from a mode-locked laser.

However, in the latter case, tuning the pump closer into the resonance gives rise to independent FWM processes that originate from the initial, multiple-FSR spacing lines. As a result, additional comb lines are generated, eventually yielding a comb with single-FSR spacing, a route to comb formation which is termed Type II. This

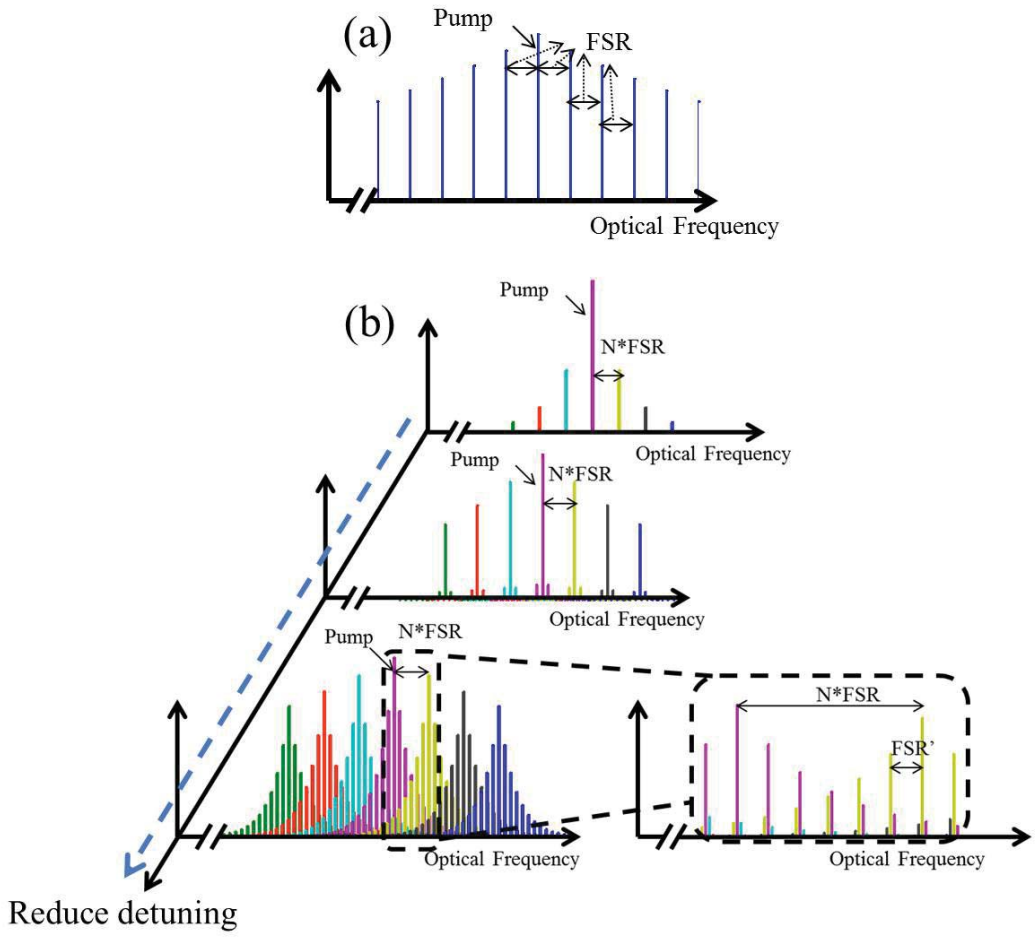

Fig. 2.2. Schematic diagrams for micro-comb formation. (a) A Type I formation. Frequency combs are formed with single-FSR spacing. (b) A Type II formation. Single-FSR combs are expanded from multiple-FSR ,initial sidebands while reducing frequency detuning.

independent FWM is illustrated with different colors in the third phase of Fig. 2.2(b). Due to the cavity dispersion in the microring, the newly generated combs are spaced with a FSR (labeled as FSR' in Fig. 2.2(b)) that is not the same FSR with the initial process. This comb formation yields substructures for each comb line that are too fine to be distinguished in the optical spectra. However, the finite cavity bandwidth will suppress the lines far off the cavity resonance and thus limit the bandwidth of the substructure for each comb [30]. Such Type II combs involve an imperfect frequency division process which leads to degraded compressibility and reduced coherence in pulse shaping experiments [28, 42]. An important point here is that these demonstrations establish a link between the route to comb formation and the coherence of the generated combs.

2.3.2 Properties of Silicon Nitride Microresonator Devices

In this chapter, two resonators are tested, both with rings with 40 μm outer radius. One resonator, which we refer to as Resonator 1, has 2 μm $\times$430 nm waveguide cross-section, loaded quality factor (Q) of 6×10^5, and an average free spectral range (FSR) of 4.78 nm. The transmission spectrum is shown in Fig. 2.3(a) while the zoomed-in spectrum of the tested resonance is shown in Fig. 2.3(b). The linewidth of the resonance is around 2.5 pm.

The measured optical spectrum directly after the Resonator 1 is shown in Fig. 2.4. The optical power is set at 26.5 dBm while the wavelength of CW laser is tuned at 1543.08 nm. For this resonance, the threshold is around 21.3 dBm. This resonator generates a Type I comb, characterized by lines generated at single-FSR spacing and high coherence.

The second resonator, which is referred to as Resonator 2, has 2 μm $\times$550 nm waveguide cross-section, loaded Q of 2×10^6, and an average FSR of 4.71 nm. Figure 2.3(c) shows the transmission spectrum while the zoomed-in spectrum for the tested resonance is shown in Fig. 2.3(d). The normalized transmission dip at resonance

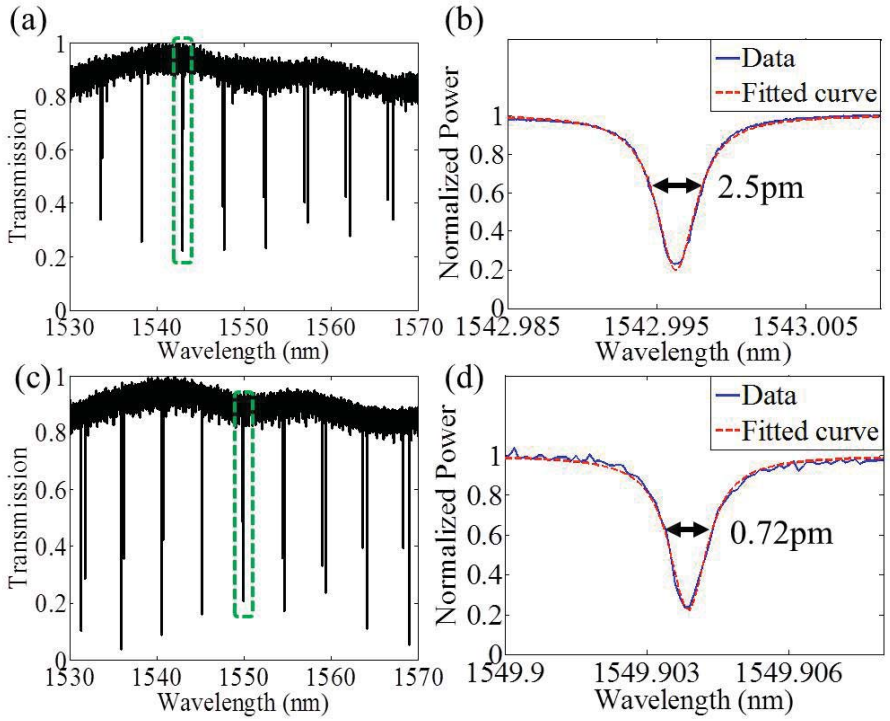

Fig. 2.3. The transmission spectra of (a) Resonator 1 and (c) Resonator 2. (b)(d) The zoomed-in spectra for the tested resonances.

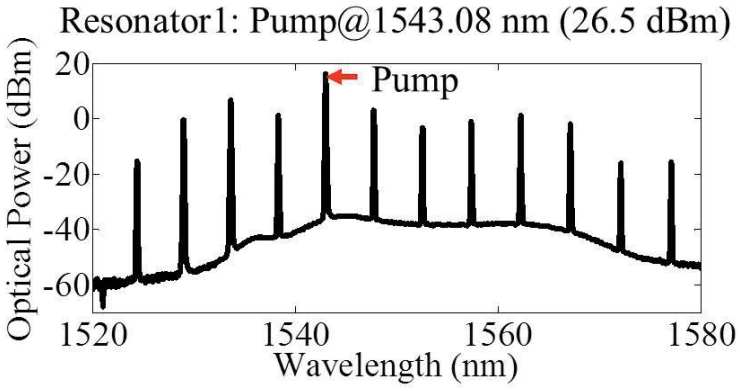

Fig. 2.4. Comb spectrum of Resonator 1. The input power of the tunable CW pump is 26.5 dBm at 1543.08 nm

shows a minimum ≈ 0.2 for both resonators. Figure 2.5 shows the optical spectra of Resonator 2 for pump wavelengths of 1549.93 nm and 1549.94 nm. Initially this resonator is observed to generate lines spaced by two FSRs above comb generation threshold (10.8 dBm), as shown in Fig. 2.5(a). By red-shifting the pump wavelength around 0.01 nm (≈ 1 GHz), new frequencies are observed at the same input power, resulting in a spectrum with lines spaced by single FSR. This forms a Type II comb as shown in Fig. 2.5(b).

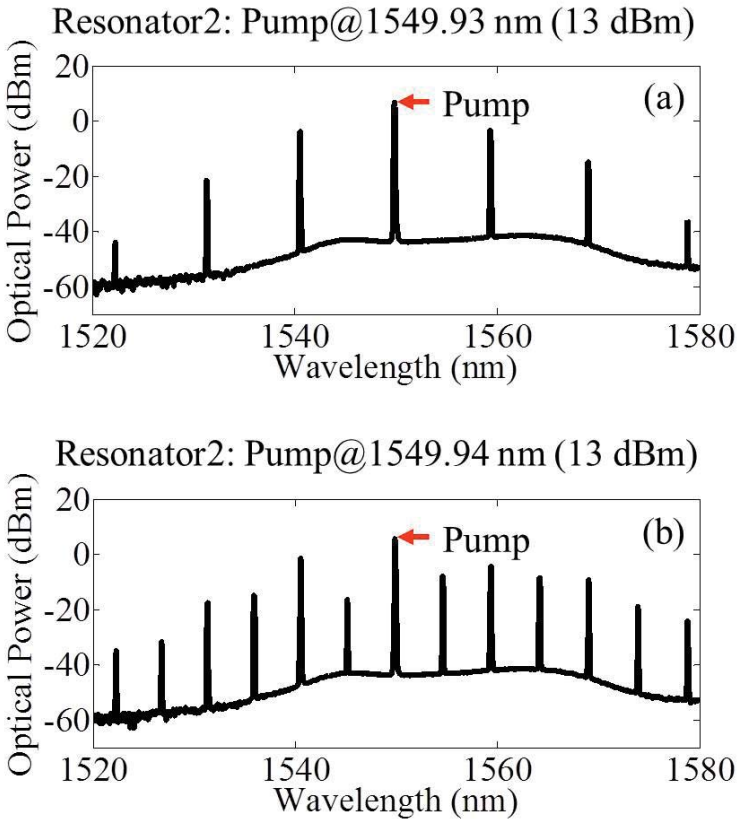

Fig. 2.5. Comb spectra of Resonator 2. The input power and wavelength of the tunable CW pump are (a)13 dBm, 1549.93 nm and (b)13 dBm, 1549.94 nm.

2.3.3 Noise Characterization

As discussed in the previous section, the subsequent FWM process in a Type II formation will result in linewidth broadening for each comb line and thus degrade the temporal coherence. This dynamics could also be identified from the observation of radio frequency (RF) beat notes in an RF spectrum analyzer. This is consistent with the observations of multiple and broad beat notes in previous works [19, 26], where phase noise was measured under different pump detuning.

To shed light on the onset of the comb noise, the RF beat notes were investigated under different comb generation processes presented before. Since the repetition rate of each mode family in silicon nitride microresonators is typically much larger than tens of GHz, the beating between each comb line is hard to observe directly through electronic measurement. Therefore, some reports discussed the linewidth and noise properties of the generated combs through beating with an external CW laser [30], while some studies convert the comb lines to baseband for analysis by mixing with a microwave signal [26].

Figure 2.6 shows intensity noise spectra of three exemplary comb lines selected out of the generated combs from Resonator 1. The measurement is performed over the frequency range 0 MHz to 700 MHz with 1.5 MHz resolution bandwidth. For this Type I comb from Resonator 1, the RF spectra for three different selected lines (1538.3 nm, 1543.0 nm, and 1547.7 nm) are essentially identical and are at the noise floor of the spectrum analyzer.

For Type II formation from Resonator 2, the intensity noise is characterized under different comb generation processes. When pumping at 1549.93 nm with 13 dBm optical power, the initial sidebands of frequency combs from Resonator 2 first start with 2-FSR spacing. As discussed in Sec.2.3.1, this process produces spacings precisely equal across the combs. The RF spectra of the 1559.4 nm comb line generated from Resonator 2 with slightly different pumping wavelengths are shown in Fig.2.7(a). Clearly, before forming a single-FSR comb, the intensity noise, plotted in black line,

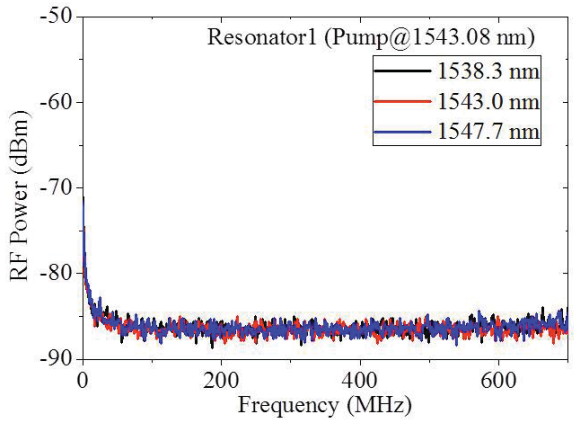

Fig. 2.6. RF noise spectra of three exemplary combs obtained from Resonator 1 (Type I comb).

is low and close to the noise floor of the spectrum analyzer. At this stage, the noise property is similar to that observed from a Type I generation, yielding a low-noise state RF spectrum.

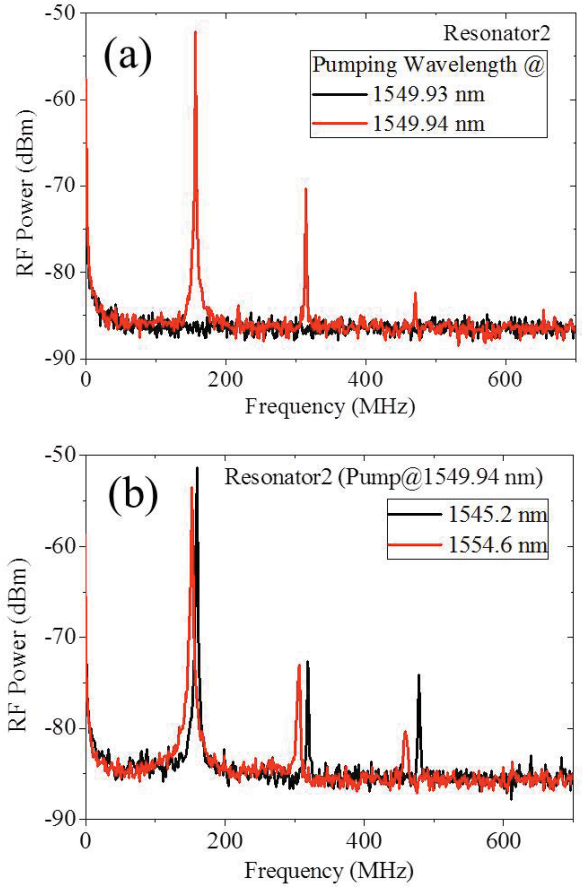

Fig. 2.7. (a)RF noise spectra of the frequency combs at 1559.4 nm before and after tuning the pumping wavelength (Resonator 2). (b) The corresponding RF spectra of the newly generated spectral lines from a Type II frequency comb with pumping wavelength at 1549.94 nm (Resonator 2).

However, when the pump is tuned slightly from 1549.93 nm to 1549.94 nm, 0.01 nm more into resonance, a Type II comb is formed as illustrated in Sec. 2.3.2. Strong intensity noise peaks are now observed in the RF spectrum at around 156 MHz and its harmonics. These data illustrate the very rapid onset of intensity noise with the transition to Type II operation.

For the newly generated combs after tuning the pump, similar noise peaks are observed in the Type II regime (Fig.2.7(b)). The presence of these noise peaks may be explained in terms of beating between combs with different offset frequencies that overlap in the same region of the optical frequency, forming a substructure for each comb line in the spectrum. The frequencies of the main noise peaks, and hence the separations of the subcombs, range from 152-164 MHz in Fig.2.7(b), which is on the order of the linewidth ($\approx$ 112 MHz full width at half maximum) of the pumped mode in Resonator 2. It agrees that the finite bandwidth will suppress the substructure far off the resonance [30].

2.4 Communication Performance of Kerr Frequency Combs

For telecommunication, a multiple-wavelength source is important for wavelength-division-multiplexing (WDM) which lets single waveguide to carry multiple data streams. Since optical communication networks have much larger bandwidth compared with the electronics networks, an on-chip integrated source capable of generating many wavelengths is essential in order to drive the optical networks. Although there are several ways to obtain multiple wavelength sources, such as multiple quantum wells [43] and hybrid lasers [44], these methods require large power consumption and space. Microresonator-based frequency combs offer the possibility to meet these requirements. In addition, the wavelength separation (repetition rate) could be controlled by designing a proper resonator dimension, which is low-cost and simple within photolithography techniques.

In previous studies, a few experiments have looked at optical communication performance using individual lines selected from a microresonator comb as light sources [45, 46]. Although in some cases, error-free communication has been observed, in other cases, communication performance is badly degraded. It is now becoming important to correlate the information provided by these different mea-

surement modalities and to establish a way to select or design microresonator devices for desired operation.

Here, optical communication measurements are investigated using the combs generated in the previous section. To test the communication performance, OOK measurements are demonstrated by modulating the individual comb lines at 9.953 Gbits/s and a length of $(2^{31}-1)$ PRBS is sent into the lithium niobate intensity modulator.

Figure 2.8(a) shows the eye diagrams of the OOK measurements for Type I combs from Resonator 1. Individual comb lines are filtered and selected as the carrier frequency at -11 dBm received optical power to the photodetector. The clean and open eyes indicate the suitability of Type I combs as a multiple-wavelength source for high quality communications. Figure 2.8(b) shows the corresponding bit error rate (BER) data as a function of the received optical power when individual comb lines produced from Resonator 1 are selected. When the received power is above -11 dBm, each of the selected comb lines exhibited error-free operation (no errors are observed over 300 s measurement time, corresponding to BERs below 10^{-12}).

For Type II operation from Resonator 2, the communication measurement is first demonstrated with the initial, 2-FSR-spaced comb before forming a single-FSR comb. High communication performance is again observed for the lines yielding good OSNR ($\geq$15 dB) after amplification. Figure 2.9(a) shows the eye diagrams at 1540.6 nm, 1549.9 nm, and 1559.4 nm, which are all nicely open. The corresponding BER data are shown in Fig. 2.9(b) with solid traces. Similar high performance compared with the Type I comb (Fig. 2.8) was observed.

However, quite different results are obtained when the pump laser is tuned 0.01 nm further into resonance for Type II operation. As more power coupled into the microring and single-FSR combs filled in between the initial sidebands, large intensity noise is then detected as discussed in Sec. 2.3.3. Now all of the generated comb lines show badly degraded eye diagrams. Figures 2.10(a)-(c) present the eye diagrams obtained for 1540.6 nm, 1549.9 nm, and 1559.4 nm comb lines at -11dBm received optical power. Compared to Fig. 2.9(a), which shows these same lines for the previous

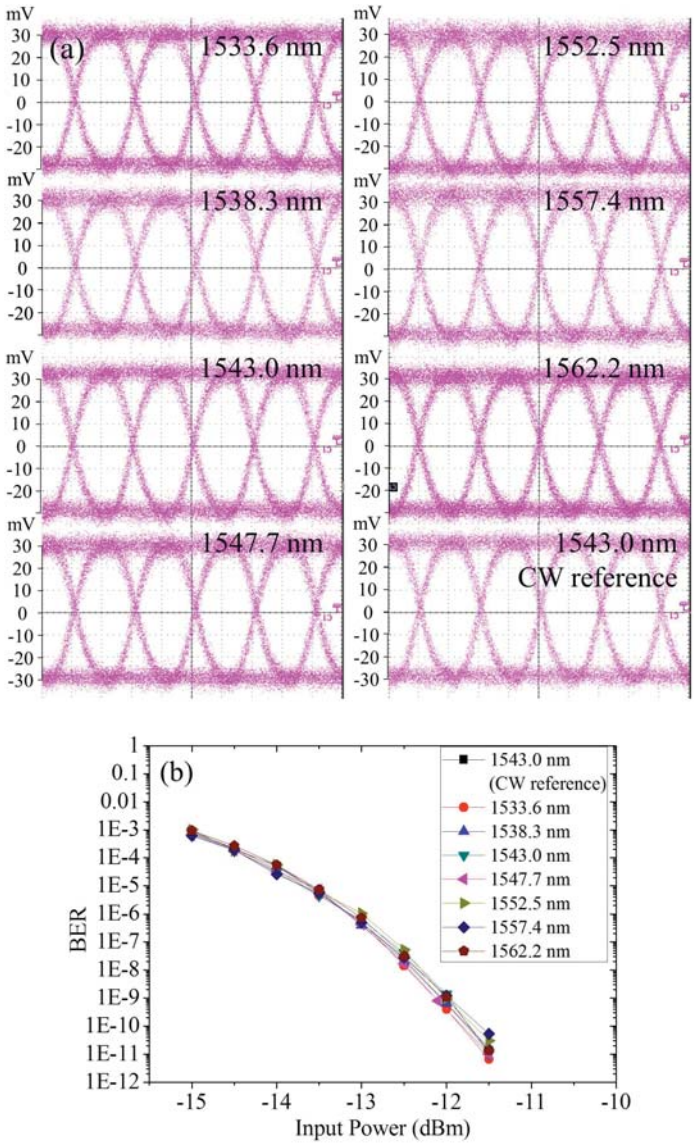

Fig. 2.8. (a) The eye diagrams of seven selected comb lines from Type I combs and the CW reference (taken prior to the microresonator). The open eye diagrams confirm the high quality of the OOK communication performance. (b) The corresponding BER results.

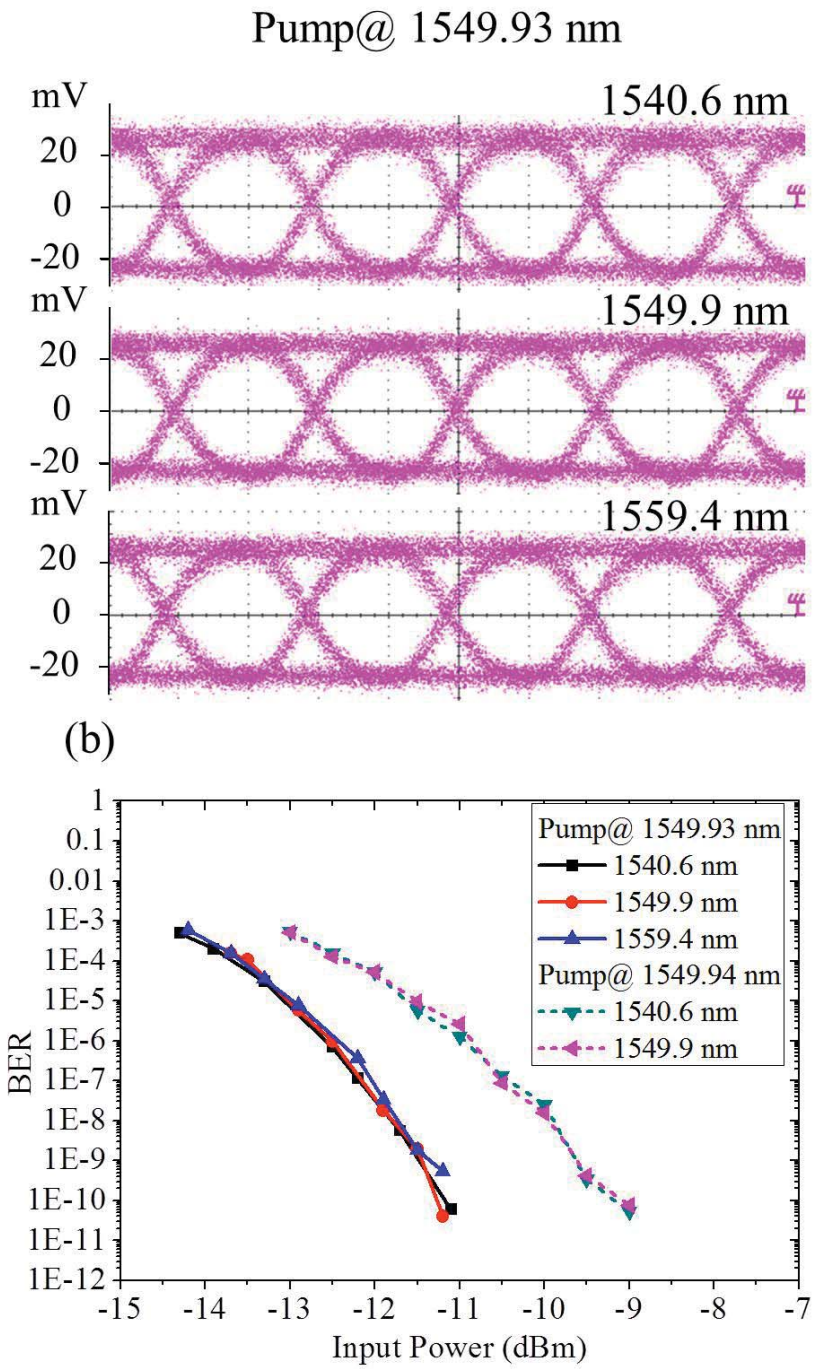

Fig. 2.9. (a)Eye diagrams of each of three filtered comb lines generated from Resonator 2 with pumping at 1549.93 nm. The received power for the plotted eye diagrams is -11 dBm. (b)The BER results of selected combs with pumping at 1549.93 nm (solid traces) and at 1549.94 nm (dashed traces).

two-FSR-spaced comb, now the eyes experience significant closure, with a high level of intensity noise clearly observed on the top rail of the eye, corresponding to the 'on' state. It indicates that the independent FWM for Type II operation results in the degradation of the optical communication performance; the degradation also strongly correlates with the observed intensity noise in radio frequency.

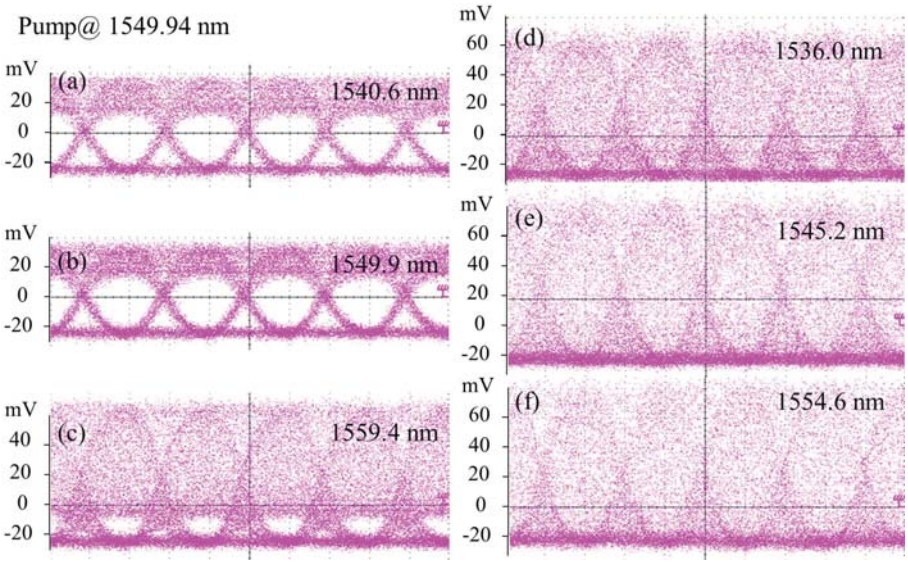

Fig. 2.10. The eye diagrams of a Type II frequency comb with pumping at 1549.94 nm. The received power for the plotted eye diagrams is -11 dBm.

As for the newly generated comb lines after the transition to Type II operation, the eyes are now completely closed as shown in Figs. 2.10(d)-(f). This qualitatively agrees the observed intensity noise in Sec. 2.3.3. Although all the lines in Type II operation are degraded, the degree is different from line to line, which corresponds to the increase in the integrated intensity noise.

The BER curves corresponding to the eye diagrams of Figs. 2.10(a) and (b) are shown in Fig. 2.9(b) with dashed traces. These two curves shown under Type II operation exhibit a power penalty of $\approx$ 2 dB compared with that under a multiple-FSR comb formation. For the eyes are nearly (1559.4 nm) or completely closed, the communication performance was so bad that error rate tester was unable to determine

the error rate. These findings, showing a strong correlation between noise intensity and communication performance, suggest that in the absence of a transition to a low-noise state, such as in [38], Type II combs are unsuitable for optical communications.

2.5 Line-by-line Pulse Shaping and Temporal Coherence

In the last section of this chapter, the temporal coherence of the generated combs will be investigated. The ability to generate short pulses and high coherence combs from microresonators offers attractive opportunities for several applications in ultrafast optics. Since the mode spacing of microresoantor-based frequency combs is typically large enough for pulse shaping at the individual line level, the temporal behaviors are easily controlled by manipulating the spectral phase for a coherent comb generation, which is also termed optical arbitrary waveform generation (OAWG) [47]. By applying line-by-line pulse shaping on microresonator frequency combs, a transform-limited pulse could be generated and realized by the coherent comb generation.

First, a Type I comb from Resonator 1 (Fig. 2.4) is characterized and Fig. 2.11 shows the measured autocorrelation traces. The red lines are the intensity autocorrelation traces calculated based on the measured spectra after the pulse shaper and assuming flat spectral phase, while the green and blue traces show the measured autocorrelation traces before and after the line-by-line phase compensation. The measured autocorrelation trace after pulse compression (blue line) is in close agreement with the calculated one. This demonstrates successful pulse compression and a high level of coherence.

For Type II dynamics from Resonator 2, the comb at multiple-FSR stage again yields high coherence as shown in Fig. 2.12(a). However, after forming a Type II comb by pumping at 1549.94 nm, the on-off contrast of the experimental autocorrelation (shown in Fig. 2.12(b)) is significantly degraded compared to that of the simulated traces. In general, the reduction in autocorrelation contrast ratio indicates reduced coherence as well as degraded compression [48, 49].

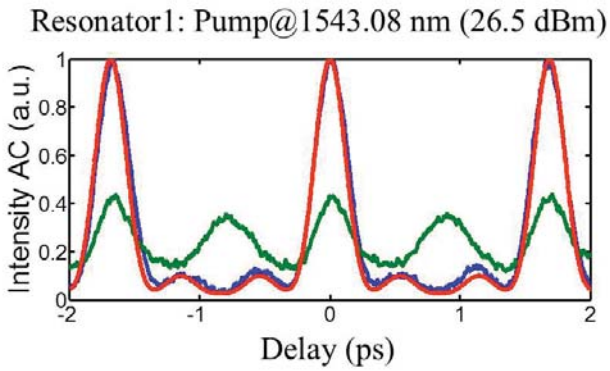

Fig. 2.11. Autocorrelation traces corresponding to the frequency combs in Fig. 2.4. Red lines show intensity autocorrelation traces calculated by taking the optical spectra and assuming flat spectral phase, while the green and blue traces show the measured autocorrelation traces before and after the line-by-line phase compensation.

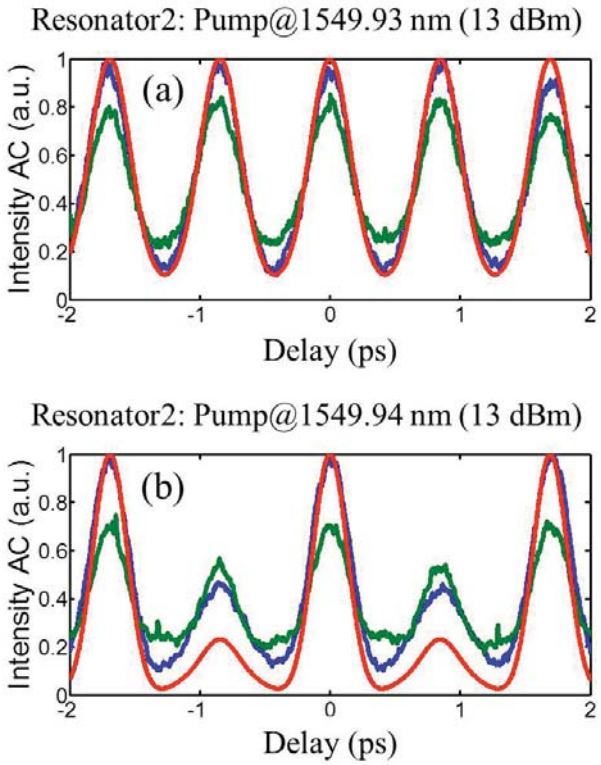

Fig. 2.12. Autocorrelation traces corresponding to the frequency combs in Fig. 2.5. Red lines show intensity autocorrelation traces calculated by taking the optical spectra and assuming flat spectral phase, while the green and blue traces show the measured autocorrelation traces before and after the line-by-line phase compensation.

2.6 Conclusion

In this chapter, the author focuses on characterizing frequency combs generated from two different silicon nitride microresonators with identical 40 μm radius. In each case the author assesses the time-domain coherence of the full comb (through pulse shaping and autocorrelation experiments) and measures intensity noise and communication performance (through 10 Gbit/s on-off keying experiments) of individual lines selected from the combs. The correlation between routes to comb formation, coherence, noise, and communication performance of Kerr combs are identified.

For the first resonator, where a comb forms directly with lines spaced with single FSR (termed as a Type I comb), the comb exhibits high coherence, low intensity noise, and excellent 10 Gbit/s optical communication results. For the second resonator, the comb initially forms with multiple-FSR line spacing. This comb formation shows the same properties compared with a Type I comb. However, after further tuning the laser frequency and forming additional lines between the spacing, a single-FSR comb (termed a Type II comb) is generated with increasing intensity noise in the form of multiple beat notes. It exhibits reduced coherence, increased intensity noise, and severely degraded performance for optical communications.

This study builds a correlation between the routes to comb formation, the coherence, intensity noise, and optical communication performance of a Kerr frequency comb generated from microresonators. This observation should prove useful in selection of microresonator devices, providing combs suitable for applications, especially in high speed optical communications and ultrafast optics. For instance, by feedback-stabilizing the combs and reducing the phase noise, a later demonstration shows the possibility to achieve the transmission of a 1.44 Tbit/s data stream over up to 300 km [46].

3. DROP-PORT STUDY AND OPTIMIZATION IN COUPLING OF MICRORESONATOR FREQUENCY COMBS

3.1 Introduction

In most previous studies a through-port geometry consisting of a single bus-waveguide, fiber, or coupling prism is used to couple light both into and out from the microresonators, while a few experiments utilize a drop port as an output coupler [18, 21, 25, 50, 51]. Typically, the comb spectra observed at the through port contains a strong peak at the pump frequency (Fig. 3.1), which often is 20 dB or even more above the adjacent comb lines [15, 23, 26–28, 30, 32, 35, 38, 39, 42]. Thus, the power transfer into the comb is typically poor. In addition, merely with the through-port measurement, the detected optical spectra at pump frequency consist of both the light transmitted through the bus-waveguide and the light coupled back from the ring resonator. Therefore, the field inside the ring could not be investigated separately.

In this chapter, a drop-port geometry is used to characterize frequency combs generated from silicon nitride on-chip microresonators first in the normal group velocity dispersion regime. This drop port can be used as a monitor for Kerr comb formation internal to the rings. In sharp contrast with the traditional transmission geometry, a smooth output spectra with comparable power in the pump and adjacent comb lines is observed. The power transfer into the comb may be explained to a large extent by the coupling parameters characterizing the linear operation of the resonances studied. It not only helps us to investigate the power coupling in SiN-based microresonator but also offers a way to study the comb dynamics internal to the ring. Furthermore, comparison of through- and drop-port spectra shows that much of the

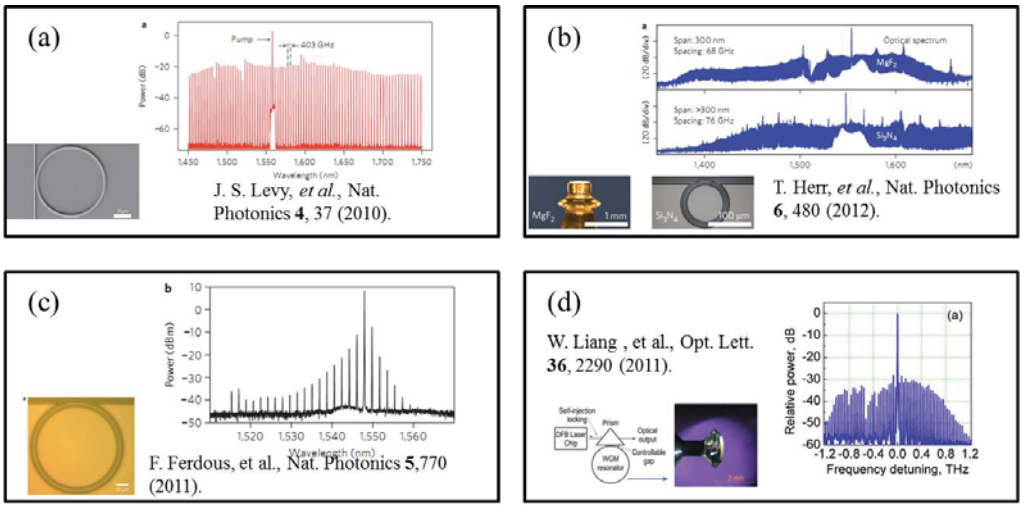

Fig. 3.1. Exemplary optical spectra at the through port from (a) Ref. [27], (b) Ref. [30], (c) Ref. [28], and (d) Ref. [23]. A strong pump line is observed.

amplified spontaneous emission (ASE) noise is filtered out by transmission to the drop port. This drop-port geometry also gives proof of the pump clamping in the cavity, similar to that observed in traditional optical parametric oscillators. In addition, the power transfer in the cavity and comb-induced coupling change will be discussed. In the end, an over-coupled device with a single bus-waveguide is utilized to study the coupling optimization in the presence of comb generation.

3.2 Power Responses for Add-drop Filters

In previous studies [52, 53], a drop-port waveguide has been widely used in microresonators as compact and narrow-linewidth bandpass filters at optical frequencies. These drop filters are important to access one frequency channel without disturbing the others for a wavelength division multiplexed (WDM) signal. A schematic diagram of micoring-based drop filters is shown in Fig. 3.2. Individual frequency is selected by distinct rings with different resonant frequencies. The bandwidth of each channel is determined by the linewidth of the ring resonance.

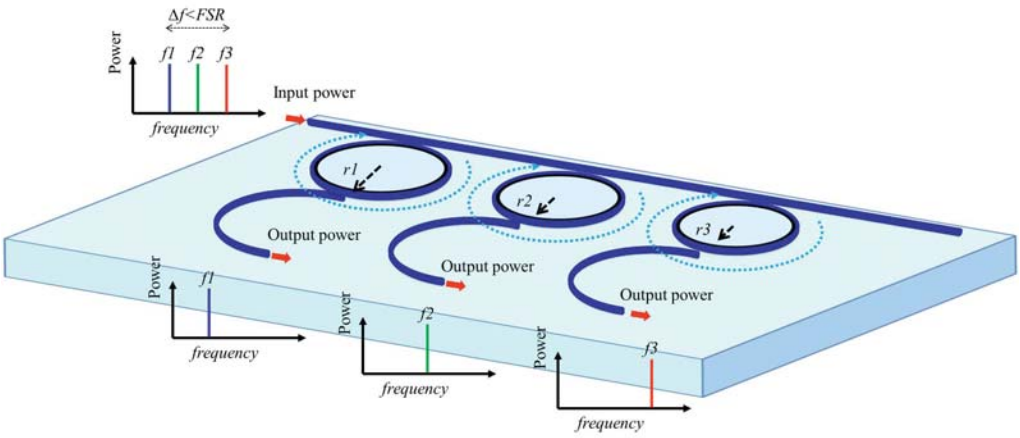

Fig. 3.2. Schematic diagram of microring-based add-drop filters for WDM application.

In the following discussions, the single ring resonator with drop-port geometry is analyzed by the method of coupling of modes. The power response at both the through and drop port will be discussed.

3.2.1 Mode Coupling Theory

Based on the theory proposed in [54], the power responses at the through- and drop-port transmission could be derived as follows. The time-variant equation for the energy internal to the ring is expressed as [54]:

$$\frac{d}{dt}a = (j\omega_0 - \frac{1}{\tau})a - j\mu s_i \tag{3.1}$$

where a is the energy amplitude in the ring ($|a|^2$ represents the total energy in the ring.), ω_0 is the resonant frequency of the ring, $1/\tau$ stands for the decay rate in the ring per round trip, μ is the mutual (field) coupling parameter between a single waveguide and a ring, and s_i is the field amplitude of the incident field. Figure 3.3 illustrates the physical notation of the field transfer in an add-drop filter. The kappa coefficients(κ_p, κ_e, and κ_d), indicating the power dissipating from the cavity, will be discussed later.

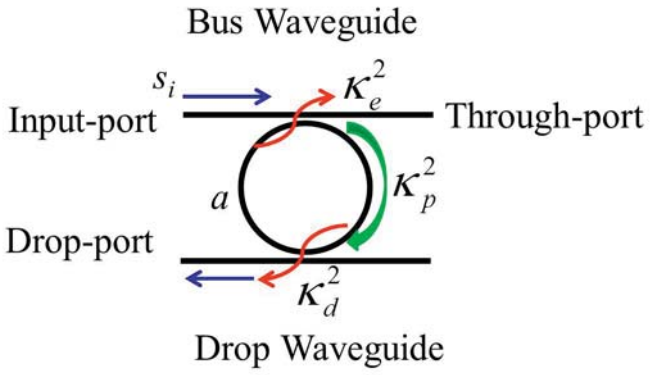

Fig. 3.3. Schematic diagram of a microring-based add-drop filter with coupling parameters.

It should be noted here that the decay rate is related to the power coupling out of the ring and dissipating in the ring (a.k.a. the intrinsic loss of the ring with decay rate $1/\tau_p$). The decay rates of the coupling power are described as $1/\tau_e$ at the bus-waveguide and $1/\tau_d$ at the drop waveguide. Therefore, the total decay rate could be expressed as [54]:

$$\frac{1}{\tau} = \frac{1}{\tau_p} + \frac{1}{\tau_e} + \frac{1}{\tau_d} \tag{3.2}$$

The field of the transmitted wave at the bus-waveguide is then written as $s_t = s_i - j\mu a$.

For a special case, if there is no drop-port ($1/\tau_d = 0$), no intrinsic loss in the ring ($1/\tau_p = 0$), and no input power, the time-variant energy in the ring can be expressed as the following equation:

$$|a(t)|^2 = |a_0|^2 exp(\frac{-2t}{\tau_e}) \tag{3.3}$$

The transmitted wave coupled from the cavity is then described as:

$$|s_t|^2 = \frac{\kappa_e^2 |a(t)|^2}{T_R} = \kappa_e^2 |a(t)|^2 (\frac{v_g}{2\pi R}) \tag{3.4}$$

where T_R is the round-trip time of the ring resonator, κ_e^2 is the fraction of power coupled between the bus-waveguide and the resonator, v_g is the group velocity in microresonators, and R is the radius of the microring. Without the input power, the transmitted power is simplified as $|s_t|^2 = |\mu|^2 |a(t)|^2$. Therefore, based on Eq. 3.4, the mutual coupling parameter can be expressed as: $\mu^2 = \kappa_e^2 (\frac{v_g}{2\pi R})$. The relation could be further related to the decay rate at the bus-waveguide by taking the derivative of Eq. (3.3) when there is no incident field (s_i=0), which gives [54]

$$\mu^2 = \kappa_e^2 (\frac{v_g}{2\pi R}) = \frac{2}{\tau_e} \tag{3.5}$$

Similarly, the power coupled to the drop-port waveguide can be expressed as

$$|s_d|^2 = \kappa_d^2 |a(t)|^2 (\frac{v_g}{2\pi R}) = \frac{2}{\tau_d} |a(t)|^2 \tag{3.6}$$

where κ_d^2 is the dimensionless coefficient characterizing the power coupled out of the microring from the drop waveguide per round trip.

Considering a steady-state incident field with frequency ω, the solution of field in the ring could be expressed as

$$a = \frac{-j\mu s_i}{j(\omega - \omega_0) + \frac{1}{\tau}} \tag{3.7}$$

and therefore by replacing μ in Eq. (3.7) with Eq. (3.5), the transmitted field is now [54]

$$s_t = s_i - j\mu a = \frac{j(\omega - \omega_0) + \frac{1}{\tau} - \frac{2}{\tau_e}}{j(\omega - \omega_0) + \frac{1}{\tau}} s_i \tag{3.8}$$

while the drop-port field is derived as

$$s_d = \frac{-j\sqrt{\frac{2}{\tau_e}}\sqrt{\frac{2}{\tau_d}}}{j(\omega - \omega_0) + \frac{1}{\tau}} s_i \tag{3.9}$$

3.2.2 Power Responses for Though and Drop Port

Based on the previous discussion, the power responses at both through port (T_{thru}) and drop port (T_{drop}) can be derived further from Eq. (3.8) and Eq. (3.9):

$$T_{thru} = \frac{|s_t|^2}{|s_i|^2} = \frac{(\omega - \omega_0)^2 + (\frac{1}{\tau} - \frac{2}{\tau_e})^2}{(\omega - \omega_0)^2 + (\frac{1}{\tau})^2} = \frac{(\omega - \omega_0)^2 + (\frac{1}{\tau_p} + \frac{1}{\tau_d} - \frac{1}{\tau_e})^2}{(\omega - \omega_0)^2 + (\frac{1}{\tau})^2} \tag{3.10}$$

$$T_{drop} = \frac{|s_d|^2}{|s_i|^2} = \frac{\frac{4}{\tau_e \tau_d}}{(\omega - \omega_0)^2 + (\frac{1}{\tau})^2} \tag{3.11}$$

Here, if the driving frequency (ω) is not too far away from the resonant frequency (ω_0), the frequency and wavelength differences could be related to the following equation:

$$|\lambda - \lambda_0| = \delta\lambda = \lambda^2 \frac{|f - f_0|}{c} \tag{3.12}$$

By replacing coefficients τ with κ according to Eq. (3.5) as proposed in [55], the power responses are further expressed as:

$$T_{thru} = \frac{(\lambda - \lambda_0)^2 + (\frac{v_g \lambda^2}{8\pi^2 Rc})^2(\kappa_p^2 + \kappa_d^2 - \kappa_e^2)^2}{(\lambda - \lambda_0)^2 + (\frac{v_g \lambda^2}{8\pi^2 Rc})^2(\kappa_p^2 + \kappa_d^2 + \kappa_e^2)^2} \tag{3.13}$$

$$T_{drop} = \frac{4(\frac{v_g \lambda^2}{8\pi^2 Rc})^2 \kappa_e^2 \kappa_d^2}{(\lambda - \lambda_0)^2 + (\frac{v_g \lambda^2}{8\pi^2 Rc})^2(\kappa_p^2 + \kappa_d^2 + \kappa_e^2)^2} \tag{3.14}$$

κ_e^2 is the dimensionless power loss per round trip due to intrinsic loss in the resonator.

The FSR of the resonator is defined as $v_g/2\pi R$ in frequency, and with a high-quality factor device, where the resonant linewidth is much smaller than the FSR, the FSR in wavelength can be expressed as

$$FSR_\lambda = \frac{v_g \lambda^2}{2\pi R c} \tag{3.15}$$

Finally, the expressions for the transmission response is now [55]

$$T_{thru} = \frac{(\lambda-\lambda_0)^2 + (\frac{FSR_\lambda}{4\pi})^2(\kappa_p^2+\kappa_d^2-\kappa_e^2)^2}{(\lambda-\lambda_0)^2 + (\frac{FSR_\lambda}{4\pi})^2(\kappa_p^2+\kappa_d^2+\kappa_e^2)^2} \tag{3.16}$$

$$T_{drop} = \frac{4(\frac{FSR_\lambda}{4\pi})^2\kappa_e^2\kappa_d^2}{(\lambda-\lambda_0)^2 + (\frac{FSR_\lambda}{4\pi})^2(\kappa_p^2+\kappa_d^2+\kappa_e^2)^2} \tag{3.17}$$

3.3 Experimental Results

3.3.1 Resonator Properties and Experimental Setup

Figure 3.4(a) shows the microscope image of a silicon nitride microring resonator with 2 μm $\times$550 nm waveguide cross-section and 100 μm radius. The gaps between the resonator and the through-port and drop-port waveguides are both 700 nm, suggesting a symmetrical coupling. For stable coupling, a pair of lensed single-mode fibers are placed into U-grooves as shown in Fig. 3.4(b) and aligned with the waveguide. Here, although in the current experiments, the through- and drop-port coupling are symmetric, asymmetric designs with weaker drop-port coupling are also possible. This would lessen the effect on the loaded Q, at the cost of reduced power transfer to the drop-port waveguide. However, it would be appropriate if the primary aim of this drop port is to provide a monitor for the internal comb field inside the ring.

For the experimental setup, measurements of spectra at through and drop ports are performed sequentially using an optical spectrum analyzer (OSA); the output lensed fiber is positioned first at one output and then moved to the other with the input lensed fiber fixed.

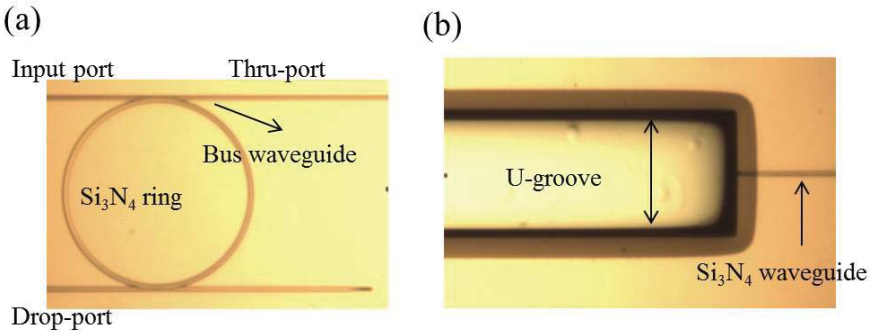

Fig. 3.4. (a) Microscope image of a 100 μm radius silicon nitride microring with coupling region. (b) Image of a U-groove.

For the following studies of comb spectra and power transfer, two TE resonances are investigated, for which the electric field is predominantly polarized parallel to the plane of the wafer. The polarization of the modes is identified by the procedure proposed in [56]. Using a polarizer at the output guide, the polarization of coupled modes is determined in the free space by the transmitted power after the polarizer at different angles.

Figures 3.5 show the transmission spectra of the two TE resonances. The first resonance (TE1) is a doublet centered at around 1558.4 nm (Fig. 3.5(a)), which has intrinsic quality factor (Q) approximately 3.1×10^6 for each of the individual lines and belongs to a mode family with 1.84 nm average FSR. This splitting of the resonant peak may result from a backward propagating wave induced by scattering from the coupling regions [57] or surface roughness [58]. The second resonance (Fig. 3.5(b)) occurs near 1558.7 nm, has intrinsic Q around 1.0×10^6, and belongs to mode TE2 with 1.76 nm average FSR. The modes here are identified by simulating the group index for different modes [59] and comparing the estimated FSR with the experimental one. From the transmission spectra, the power differences between the through and drop port are 14.0 dB for TE1 resonance and 4.7 dB for TE2 resonance; it implies that for TE2 mode, at least the resonance studied, the coupling condition is closer to critical coupling and therefore the coupled drop-port power should be much higher.

3.3.2 Comb Spectra from Through and Drop Ports

In the following demonstrations, the comb spectra from these two resonances are first investigated both at the though and drop ports. To generate a frequency comb, the laser is tuned into the resonance from the short wavelength side to achieve a soft thermal lock [18,27,60]. The linewidth of the pump line is estimated narrower than 20 MHz by beating with a fiber comb source (Menlo Systems). It is at least three times narrower than the $\approx$ 64 MHz linewidth of the higher-Q (3.1×10^6) TE1 resonance.

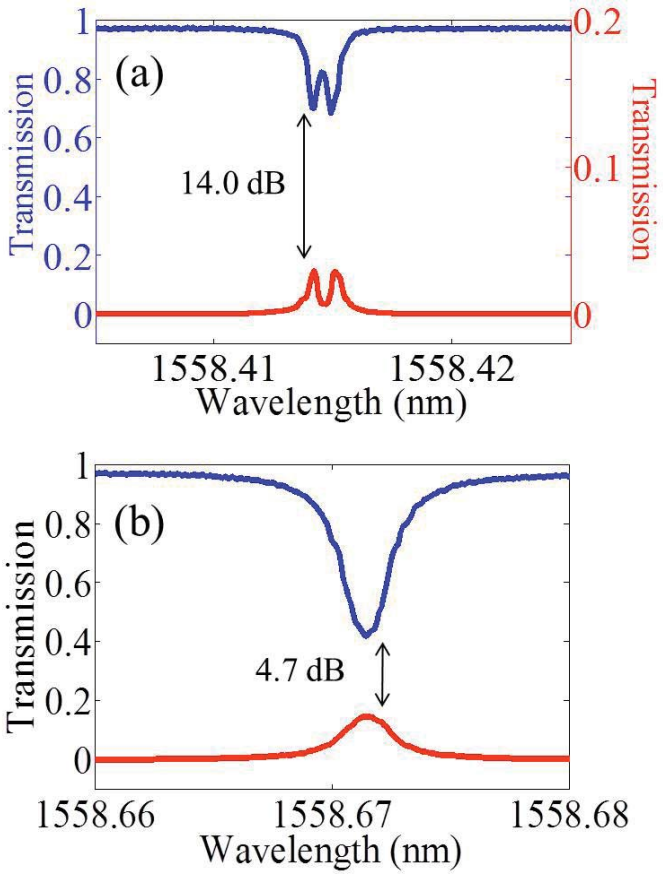

Fig. 3.5. The transmission spectra with low input power at (a)1558.41 nm and (b)1558.67 nm resonances; the vertical scale on the left axis of (a) shows the intensity of drop-port transmission.

At the highest input power studied, Figures 3.6 show the exemplary optical spectra observed both from the through (blue trace) and drop port (red trace) with (a) 430 mW at around 1558.5 nm (TE1 mode) and (b) 680 mW at around 1558.8 nm (TE2 mode). The input power here is defined as the power estimated in the input bus-waveguide by measuring the fiber to fiber loss between input and through port, typically 3 to 5 dB, and assigning half of this loss to the input side. For the TE1 mode, frequency combs are observed to generate lines spaced by 3-FSR spacing; and, for the TE2 mode, a 5-FSR comb is excited. Both resonances are red-shifted around 0.1 nm due to the thermal nonlinearity under the pumping conditions described above.

First, for the spectra measured from the through port, ASE noise from the high power amplifier is clearly observed. For the spectra measured from the drop port, the ASE noise between the comb lines is filtered out for both cases, which increases the optical signal to noise ratio (SNR) of microresonator-based frequency combs. Another important point is that the drop-port data reveal the power spectrum and field information internal to the microring. Although the power at the pump frequency is much stronger than that of the adjacent comb lines in the through-port data; in the drop-port data, the power at the pump frequency is much closer to that of the adjacent lines. Evidently, for these two resonances demonstrated here, the combs internal to the microring have approximately smooth spectra. For the through port, the pump is 19.1 dB stronger than the stronger of the adjacent lines, while at the drop-port spectrum, the pump is actually slightly (1.7 dB) weaker than the stronger of adjacent lines. In addition, the pump at the drop-port data is around 22.6 dB weaker compared with that at the through port. For the data in Fig. 3.6(b), the pump at the drop port is around 12.5 dB weaker than that at the through port. Similarly, a large degree of smoothness at the drop-port spectrum could be observed in this case. Compared to the stronger of the adjacent lines, the pump is 16.3 dB stronger at the through port but only 5.5 dB stronger at the drop port. To a large extent, the much stronger pump line observed at the through port is related to coupling conditions, not to the actual comb in the ring.

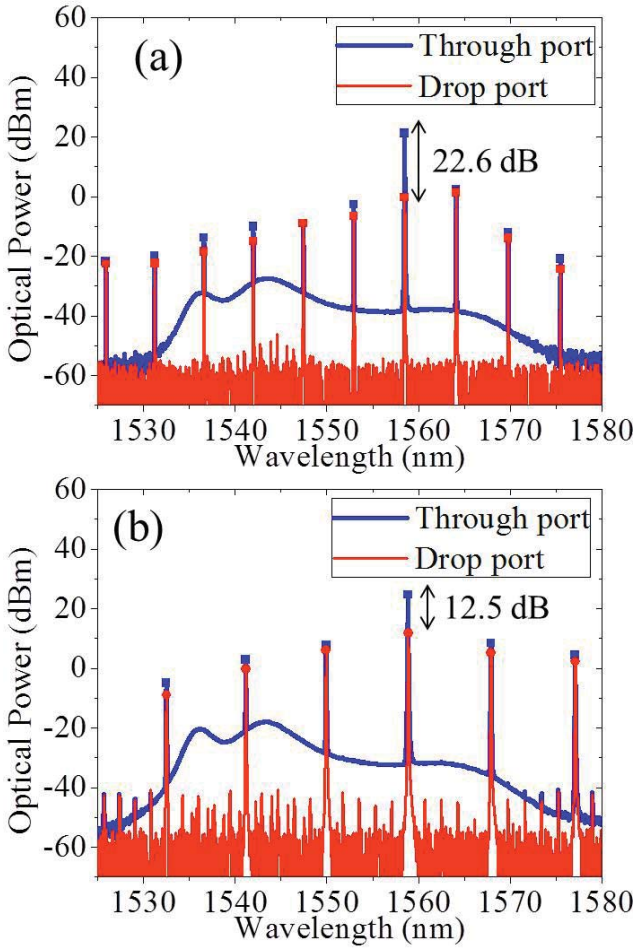

Fig. 3.6. Measured optical spectra of generated combs from both the through (blue trace) and drop port (red trace) with input power (a) 430 mW at around 1558.5 nm (TE1 mode) and (b) 680 mW at around 1558.8 nm (TE2 mode).

The demonstrations of the drop waveguide give the possibility to generate a smooth comb spectrum. Even compared to the previous studies employing a drop-port geometry [18, 21, 25], the spectra demonstrated here, particularly Fig. 3.6(a) exhibit a degree of smoothness in the region around the pump rarely observed. The absence of a strong pump line in the drop-port spectra suggests that at least under some conditions (e.g. normal dispersion cavity), the continuous-wave component of the internal field can be small.

Note here that, aside from the pump line, the output comb lines from the through and drop ports show close to the same power level, except the drop-port lines are reduced by an average of 2.5 dB relative to that from the through port for both cases. Since with symmetrical coupling, the comb lines from through and drop ports should have the same power ideally, this implies either the coupling is unintentionally slightly different or the output drop guide has larger loss. In order to account for this difference, the estimated drop-port power is adjusted upwards by 2.5 dB in the following discussions for power transfer.

3.3.3 Coupling Parameters and Conditions

In previous discussions, the comb spectra and transmission spectra have been characterized for both resonances; a large fraction of pump power emerges from the through-port data. It is now interesting to consider the coupling conditions quantitatively. Table 3.1 shows the measured transmission responses for the through and drop ports. Following the theory proposed in [55] (also described in the previous section) the coupling parameters (κ) could be extracted by fitting the through-port transmission spectra using Eq. (3.16). The fitting results for the two resonances studied are shown in Table 3.2. The κ coefficients are defined as in the previous section. The T_{thru}/T_{drop} values in Table 3.2 are calculated by fitting transmission spectra and extracting κ factors.

Table 3.1
Transmission responses for two studied resonances

Resonance	T_{thru}	T_{drop}	T_{thru}/T_{drop} (dB)	Linewidth (pm)
1558.4 nm (TE1)	0.70	0.028	14.0	0.7
1558.7 nm (TE2)	0.42	0.142	4.7	2.3

Table 3.2
Extracted coupling parameters

Resonance	κ_e^2	κ_d^2	κ_p^2	T_{thru}/T_{drop}(dB) (Calculated)
1558.4 nm (TE1)	1.49×10^{-4}	1.49×10^{-4}	1.57×10^{-3}	14.5
1558.7 nm (TE2)	1.41×10^{-3}	1.41×10^{-3}	5.04×10^{-3}	5

Although here the parameters are fitted only with the through-port transmission, the T_{thru}/T_{drop} values in Table 3.2 are in close agreement with those observed experimentally (Table 3.1), giving confidence in the parameters extracted. From the extracted parameters, for both resonances, the loss in the microring is significantly larger than the waveguide coupling. It indicates that the resonances are featured as under-coupled. Furthermore, the intrinsic loss for the 1558.7 nm (TE2) resonance is approximately three times higher than that for the 1558.4 nm (TE1) resonance, consistent with the fact that the fundamental mode usually has lowest intrinsic loss. By comparing these two resonances, TE1 mode is much more severely under-coupled.

3.4 Pump Clamping and Comb-induced Coupling Effects

3.4.1 Power Transfer at the Through and Drop Ports

In this section, the power transfer in the combs between the through- and drop-port waveguides will be discussed. A power-dependent experiment is performed to investigate dynamics of Kerr comb formations and the effects on the intracavity power. To account for thermo-optically induced resonance shifts, at each input power the pump wavelength is tuned carefully into the resonance, which is defined as the wavelength yielding minimum power transmission from the through port (maximum transmission for drop-port measurements). The results are shown in Figs. 3.7.

The output pump power (black trace) and comb power (blue trace) at the through port versus input power for the TE1 resonance are plotted in Fig. 3.7(a). The input and output power shown here refer to power in the bus-waveguide estimated before and after the microring, respectively. The comb power is obtained by integrating the measured optical spectra excluding the pump line, while the pump power is determined by integrating over a 1 nm range centered on the pump. Clearly, both pump and comb power increase with the input power, with the comb showing a threshold effect. The threshold is around 22.4 mW determined by extrapolating the measured data. The corresponding drop-port results for TE1 mode are shown in Fig. 3.7(b).

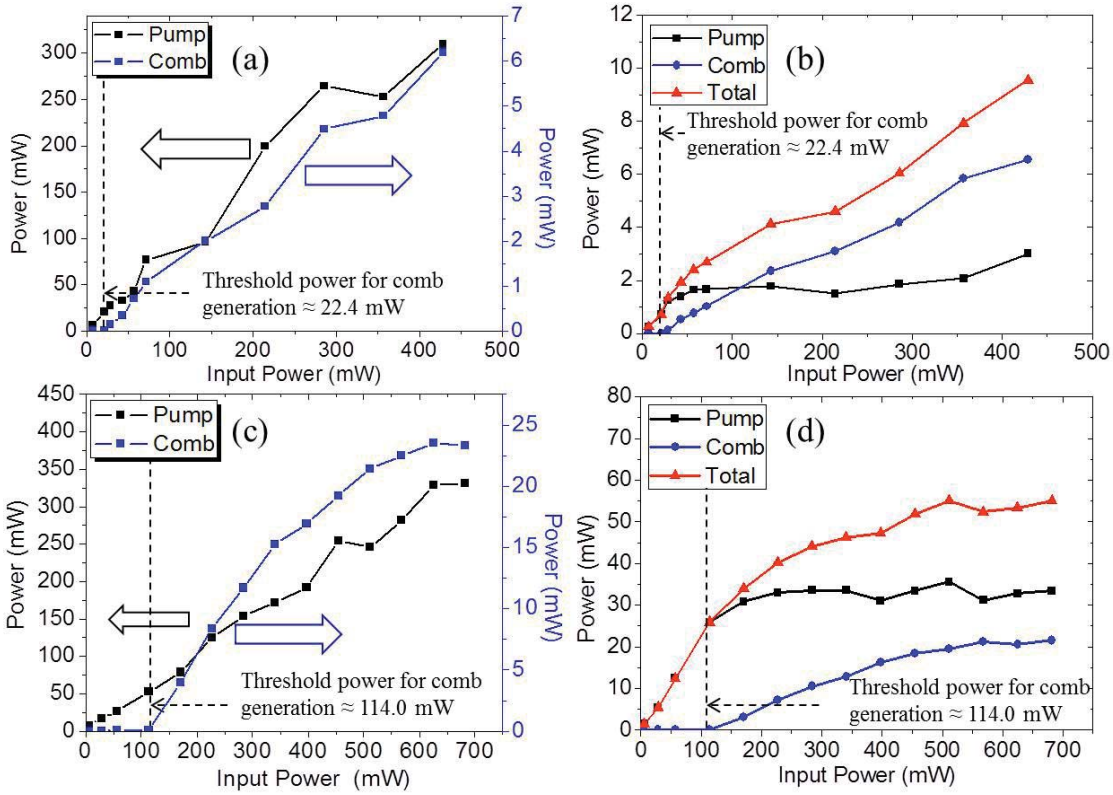

Fig. 3.7. The detected output power of the pump (black trace) and the comb lines excluding the pump (blue trace) versus input power, corresponding to the (a) through and (b) drop port at 1558.4 nm (TE1) resonance while (c) and (d) represent the analogous results from the through and drop port pumping at 1558.7 nm (TE2) resonance. The red traces in (b) and (d) stand for the total power including both pump and comb lines.

Initially, both the comb and pump power increase with input power similar to the through-port data. However, unlike the nearly linear curve of pump power measured at the through port, at the drop port, the pump power starts to saturate (although not abruptly) above the threshold for comb generation. Figures 3.7(c) and (d) show the data from the through and drop port, respectively, for TE2 mode pumping at around 1558.7 nm. It furnishes another example of pump clamping above comb generation threshold in the drop-port data. Any further increase in the input power beyond comb threshold leads to an approximately linear rise at least initially in the parametric signals (i.e., the frequency combs). Note here the drop-port data reflect the internal field inside the ring. This observation implies saturation of the parametric gain analogous to gain saturation observed in conventional parametric oscillators above threshold [61,62]. Similar saturation behavior has also been identified for microresonator frequency combs both in the drop-port experiments [18] and in simulation studies [63].

To further verify this observation of gain clamping, a resonance belonging to the TE2 mode family is also tested at around 1551.5 nm with a relatively low Q ($\approx 6.5 \times 10^5$). The transmission spectrum is shown in Fig. 3.8(a). For this resonance, no comb was generated at up to 430 mW input power, the highest power tested. The observed pump power from the drop-port data was approximately linear with input power, with no sign of saturation (shown in Fig. 3.8(b)). This supports the interpretation that pump clamping in the drop-port data provides evidence of parametric gain saturation directly linked to the Kerr comb formation.

Furthermore, the output power of the comb obtained by pumping at TE2 is substantially higher than that obtained by pumping at TE1, which agrees that TE2 resonance is much closer to critical coupling. It is also interesting to see that in both cases the output power in the comb is relatively small compared to the input power. This could be understood, at least in part, from the linear transmission spectra and the extracted coupling parameters. For the TE1 resonance, the total drop-port output power at the highest pump level is 9.6 mW, quite close to the 12 mW value

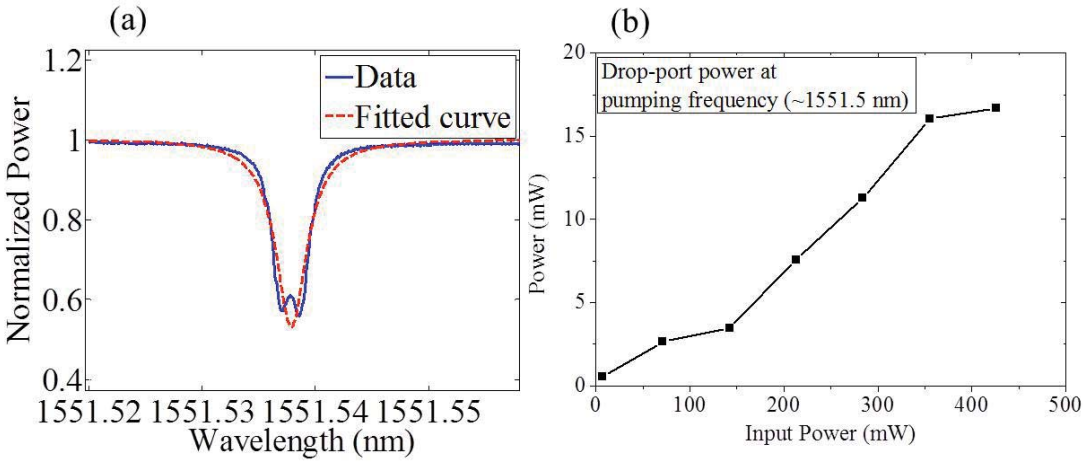

Fig. 3.8. (a) Transmission spectrum at round 1551.54 nm. (b)Drop-port power at the pump frequency.

obtained from the product of the pump power (430 mW) and the linear drop-port transmission ($T_{drop} = 0.028$). It implies that, since under severe under-coupling, the power transfers to the ring is relatively smaller than that at critical coupling. Most of the input power is transmitted through the bus-waveguide. A similar estimate for the total drop-port power for the TE2 resonance yields 97 mW, higher than but within a factor of two of the observed value (55 mW). This behavior is discussed in the following section.

3.4.2 Power Saturation and Nonlinear Effect

In addition to the linear behavior discussed in the previous section, a saturation phenomenon is evident for the comb and total (comb plus pump) drop-port power data for both resonances, but most notably in Fig. 3.7(d). This saturation can be explained through a simple, empirical model. On resonance and assuming coupling parameters $\ll 1$, the power at the through (P_{thru}) and drop ports (P_{drop}) can be written as:

$$P_{thru} = [\sqrt{P_{bus}} - \kappa_e \sqrt{P_{uring}}]^2 \tag{3.18}$$

$$P_{drop} \approx \beta (P_{bus} - P_{thru}) \tag{3.19}$$

where P_{uring} is the resonantly enhanced power in the microring at the pump frequency. Eq. 3.19 says that the drop-port power is equal to some coefficient β multiplied by the power $P_{bus} - P_{thru}$ that does not go to the through port. The coefficients β are determined by two different power contributions in the resonator, the pump power and comb power. For light that remains at the pump frequency, β could be expressed as $\beta_{pump} = \kappa_d^2/(\kappa_d^2+\kappa_p^2)$, whereas for light generated in the comb β would have $\beta_{comb} = \kappa_d^2/(\kappa_d^2 + \kappa_p^2 + \kappa_e^2)$. The difference happens here because the pump light delivered to the through port is already accounted for in Eq. 3.18, while the comb light is not. Thus, as a larger fraction of the pump light in the microring starts to transfer into the comb, the effective β factor decreases. For the TE2 resonance, this mechanism could

eventually result in a $\approx 20\%$ decrease in the drop-port power. A second mechanism is related to the observed clamping of the pump light in the resonator. This alters the interference condition governing the transmitted pump at the through port; in Eq. 3.18 one needs to use the saturated value of the intracavity pump power rather than the linear value. Thus, increasing power transfer into the comb decreases the total power coupled into the resonator, presenting a second mechanism for saturation of the drop-port output power. These effects are significantly stronger for the TE2 resonance, which is considerably closer to the critical coupling condition. Figure 3.9 shows the total drop-port power simulated for the TE2 resonance according to Eq. 3.19. Here the coupling parameters are used from Table 3.2 and β is taken as the average of β_{pump} and β_{comb}. The simulated curve is in close agreement with the observed total drop-port power (red trace) in Fig. 3.7(d).

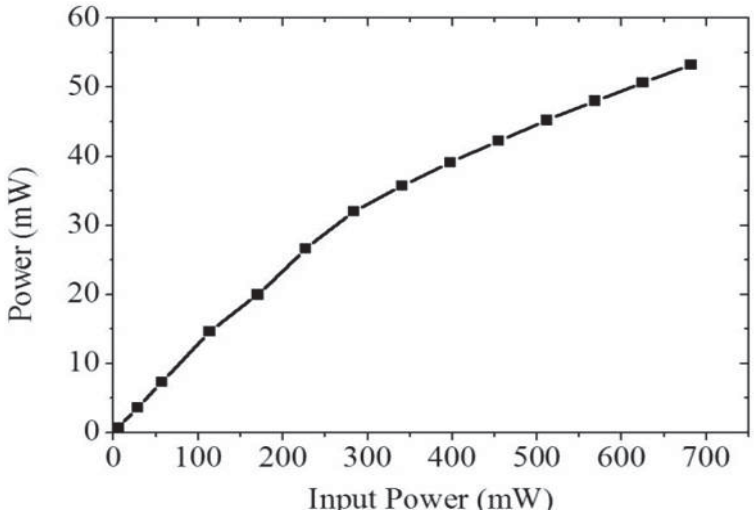

Fig. 3.9. The total drop-port power simulated for the TE2 resonance according to Eq. 3.19.

To conclude, this section investigates the coupling, power response, and information of internal comb field for microresonator-based comb generation. By utilizing a drop-port geometry, it unveils the comb spectra in the ring cavity and the nonlinear

coupling effect in the presence of comb generation. This work here helps shape the design of on-chip microresonators with desirable coupling for comb operation.

3.5 Enhanced-power Coupling for Silicon Nitride Microresonators in the Presence of Comb Generation

Typically, as stated before, the comb spectra observed at the bus-waveguide contains a strong peak at the pump wavelength, which is often 20 dB or more above the adjacent comb lines [18, 23, 27, 28, 30]. Smooth comb spectra have been demonstrated by utilizing a drop-port geometry [37]. However, a drop-port waveguide degrades the loaded Q and therefore increases the threshold power for comb generation. With the discussion of drop-port geometry in the previous section, the power transfer to the comb may be considered as an additional loss from the perspective of the pump frequency and as such affects the coupling of the pump into the resonator [37]. For typical cases of under- or critical coupling, this effect reduces the pump power build-up in the cavity. Another previous study shows the possibility to control the coupling response either by introducing gain medium in the cavity [64] or by introducing dual-coupled ring [65] with the cost of complicated fabrication and power loss.

In this section, frequency comb-enhanced coupling in silicon nitride microresonators will be discussed first. With an initially over-coupled device, a spectrum of comb lines stronger than the pump could be first time observed at the through port. A modeling approach for coupling and comb generation threshold will be later discussed to optimize the efficiency for micro-comb generation.

As the pump power in the cavity transforms into frequency combs, the intracavity power at the pump frequency decreases and therefore it alters the coupling condition at the bus-waveguide. This nonlinear mechanism results in the coupling change and could be also a crucial effect for coupling optimization. For instance, if under-coupling (or critical coupling) is first designed in a cold cavity, the coupling will be pushed into severely under-coupled as additional pump power is taken by frequency combs

or other nonlinear signals, as shown in the upper part of Fig. 3.10. Therefore, the ratio of power coupled in the ring to the power transmitted at the through port may decrease. It limits the efficiency of comb generation. In contrast, if the waveguide coupling is first designed to be over-coupled in a cold cavity (lower part of Fig. 3.10), the coupling efficiency may increase with nonlinear interaction (e.g. comb generation). By optimizing the gap between the waveguide and the ring, it is able to design critical coupling in the presence of comb formation.

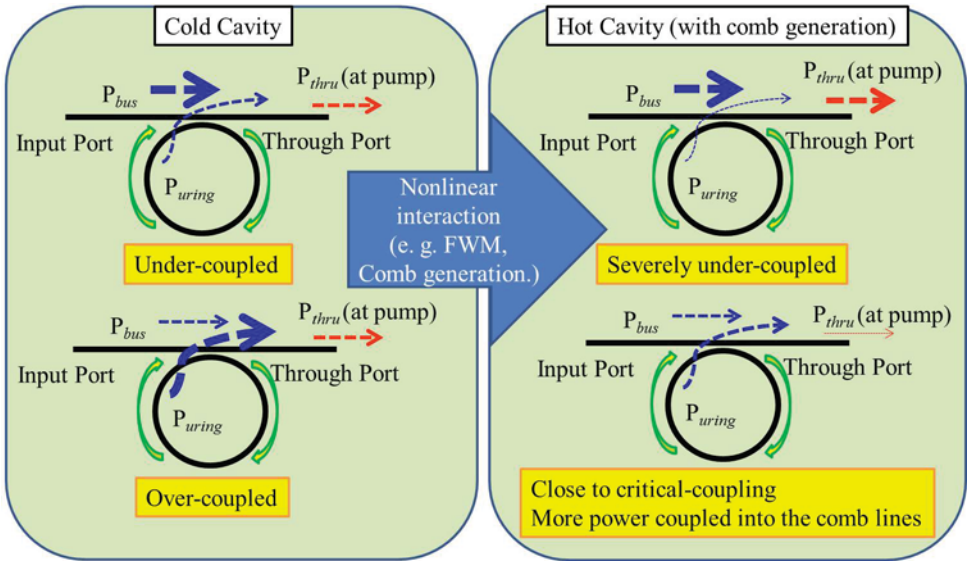

Fig. 3.10. Schematic diagram of resonator coupling: Linear and Nonlinear.

In this section, a Si_3N_4 microresonator is designed with a bus-waveguide over-coupled to the cold cavity. As the pump power increases and locks into the cavity resonance, an enhancement of the coupled pump power is observed after frequency comb generation. In addition, due to this enhanced coupling of the pump power, a spectrum with a pump line weaker than the adjacent comb lines is observed, for the first time at the through port of a microring.

3.5.1 Characterization of Coupling Condition

A Si_3N_4 ring resonator with 2 μm$\times$595 nm waveguide cross-section and 200 μm ring radius is used for comb generation, which places the cavity in the normal cavity dispersion regime. The gap between the resonator and the bus-waveguide is 300 nm, which results in over-coupling. The low power transmission spectrum at the $\approx$ 1547.83 nm resonance used for comb generation is shown in Fig. 3.11(a). To identify the coupling condition (over-coupled or under-coupled), the phase response of the resonance is obtained by sweeping a modulation sideband of the CW laser through the resonance at low power under control of a vector network analyzer [66]. Figures 3.12(a) show the schematic phase response of both over- and under-coupled resonances with the measurement setup showing in Fig. 3.12(b). The modulated frequency of the sidebands sweeps from 10 GHz to 20 GHz across the cavity resonance. An antiresonance shape could be observed in the phase response of under-coupled devices; while a 2π shift is identified in over-coupled devices. The measured phase response of the demonstrated resonance is shown in Fig. 3.11(b) with a 2π shift across the resonance, indicating the over-coupled condition. Table 3.3 shows the parameters of the resonance by fitting the transmission spectrum. Here T_{thru} is the power response at the through port, κ_e^2 and κ_p^2 are dimensionless coefficients characterizing the power lost per round trip, respectively, due to coupling to the bus-waveguide and due to intrinsic loss in the resonator. Since the cold cavity is over-coupled, κ_e^2 is larger than κ_p^2.

3.5.2 Through-port Spectra and Comb Efficiency

For an over-coupled device, the effective κ_p^2 moves closer to κ_e^2 in the presence of comb generation which takes power out of the pump line in the intracavity. Thus the coupling is pushed from the over-coupled to the critically coupled regime, and the pump power transferred into the microcavity is expected to be enhanced. To investigate this effect, the optical power spectra are recorded with different input

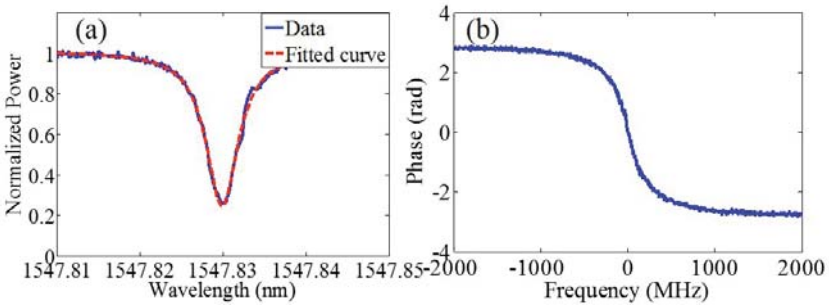

Fig. 3.11. (a) Measured transmission spectrum at around 1547.83 nm. (b) The corresponding measured phase response.

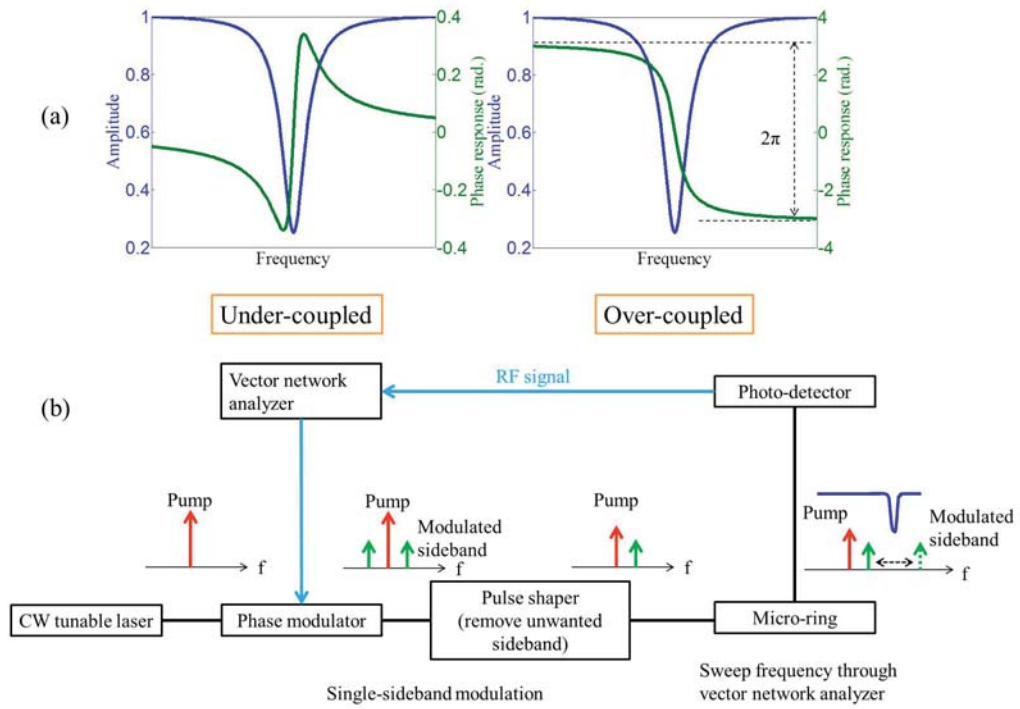

Fig. 3.12. (a) Amplitude and phase response of over- and under-coupled resonances. (b) The schematic diagram of a coupling characterization system.

Table 3.3
Parameters for Resonance at 1547.83 nm

Parameters	value
Resonance (nm)	1547.83
Intrinsic loss (κ_p^2)	7.7×10^{-3}
Coupling (κ_e^2)	2.3×10^{-2}
Transmission (T_{thru})	0.24 ($\approx$ -6.2 dB)

powers. To account for thermo-optically induced resonance shifts, at each input power the pump wavelength is tuned carefully into the resonance which is defined as the wavelength yielding minimum pump transmission at the through port. Figures 3.13 show examples of optical spectra measured at the bus-waveguide with input power varying from 550 mW to 1100 mW around 1547.83 nm. The input power used here is defined as the power at the bus-waveguide before the microring, which is estimated by measuring the input- to through-port fiber to fiber loss ($\approx$ 5.1 dB) and assigning half of this loss to the input side.

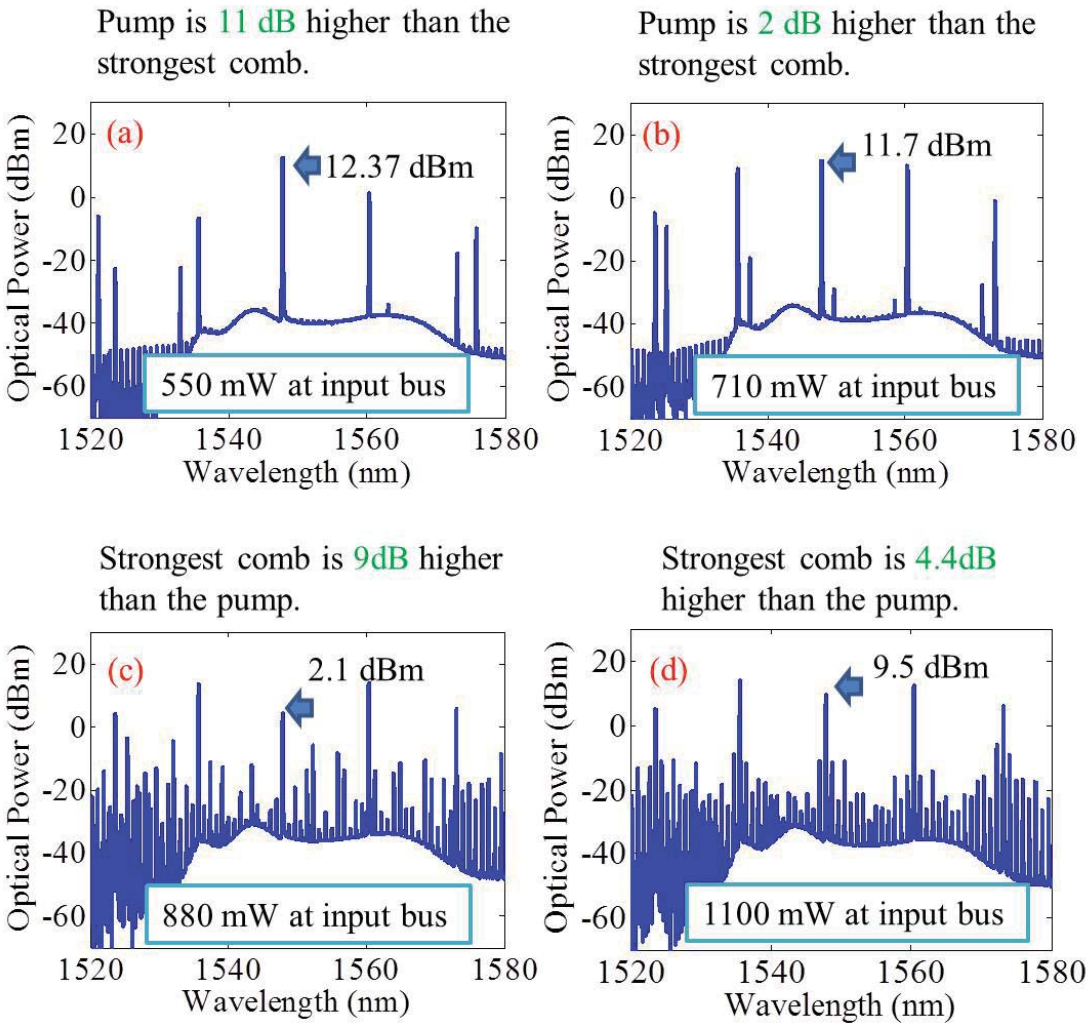

Fig. 3.13. Through-port spectra with pump powers (a)550 mW, (b)710 mW, (c)880 mW, and (d)1100 mW at the bus-waveguide.

At the beginning (Fig. 3.13(a)), the spectrum contains a strong power difference (12.4 dB) between the pump and the generated comb lines, similar to that previously observed in through-port spectra. When the input power increases and brings up the comb lines, the pump power at the output guide is slightly decreased by 1 dB and a smooth envelope of primary comb lines is observed at the output (Fig. 3.13(b)). With further input power, in Fig. 3.13(c) a strong decrease of the detected pump ($\approx$ 10 dB relative to the pump line in Fig. 3.13(a)) is seen; here the power of the strongest comb line is now 9 dB higher than the pump line. This is the first time that comb lines substantially stronger than the pump have been observed at a through port and marks the attainment of a dynamic critical coupling condition. At still higher power (Fig. 3.13(d)), the pump power begins to increase again; it suggests that further power transfer into the combs puts the pump effectively into the under-coupled regime, similar to that demonstrated in the previous section. Figure 3.14 shows the pump extinction (black trace), determined by tuning the pump wavelength in and out of the resonance, and the corresponding total output power in the comb (excluding the pump, blue trace). With varying the input power, the pump extinction remains the same before comb generation which is close to the measured value from the low-power transmission spectrum; in the presence of comb generation, the extinction strongly changes and could be as high as 19 dB. This indicates that effectively the resonance approaches critical coupling under comb generation.

Although the comb power in C-band has been discussed, it should be noted here that other effects, such as nonlinear loss mechanisms (suggested by the visible light evident in the image of the pumped resonator, Fig. 3.15), may also be in play here and may contribute to some of the features in the data, such as the variation in extinction observed around 600 mW pump power.

To further investigate this comb-enhanced coupling effect, the comb efficiency and the ratio of the comb power at the through port are shown in Figs. 3.16. The comb efficiency is defined by dividing the total comb power (excluding the pump line) by the input power at the bus-waveguide. High efficiency of comb generation ($\approx$ 18%)

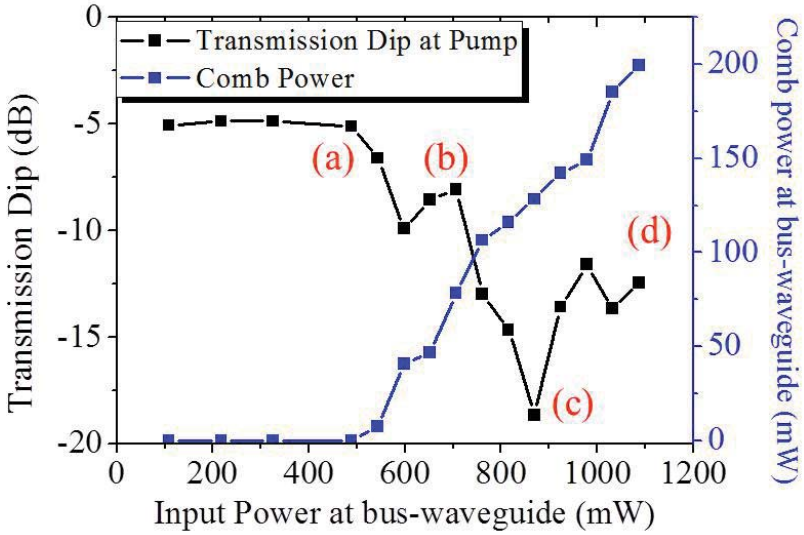

Fig. 3.14. The corresponding pump extinction measured at resonance and (black trace) the output comb power at different input powers (blue trace).

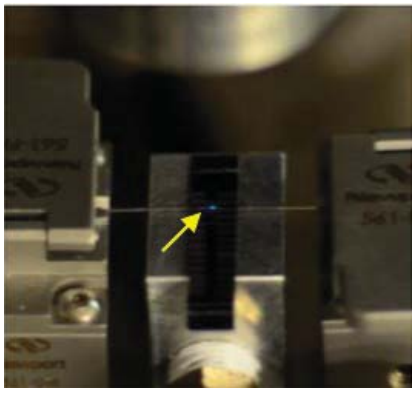

Fig. 3.15. The device image under measurement: visible light emits from the device under test.

at the through port could be observed, which is much higher than that previously demonstrated combs in this thesis (less than 10%). In addition, the ratio of the comb power measured at the through port reflects the relative ratio between the pump power and comb power. At critical coupling condition (≈ 880 mW input power), 95% of the through port power is contributed by the generated comb lines in C-band, suggesting a high conversion efficiency of comb generation.

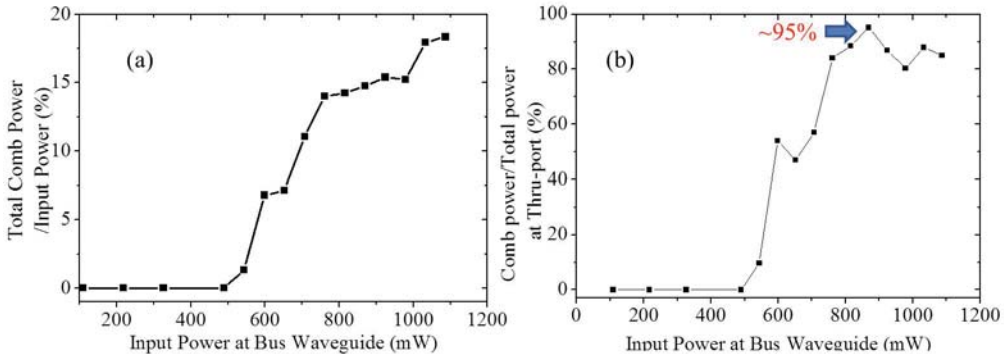

Fig. 3.16. (a)Comb efficiency and (b)ratio of the comb power to the total power at the through port.

3.5.3 Comb Generation Threshold and Coupling Optimization

Except for the coupled pump power, the coupling strength between the bus-waveguide and ring waveguide is also crucial to the threshold power for comb generation. In this section, the threshold power will be discussed with different ring geometries. The gain per round trip in the cavity could be expressed as the following equation [67]

$$2\gamma P_0(2\pi R) = \frac{2\omega n_2}{cA_{eff}} P_0(2\pi R) \tag{3.20}$$

where P_0 is the power in the microring, γ is the nonlinear parameter, n_2 is the nonlinear coefficient (m^2/W), and A_{eff} is the effective area (m^2). Note that since γ

is used to describe the field, there is a factor of 2 in front of Eq. 3.20. Assuming there is no drop-port waveguide, the loss per round trip in the ring is

$$\frac{2\pi R}{v_g}(\frac{1}{\tau_{in}}+\frac{1}{\tau_{ext}})=\frac{(2\pi R)n_g}{c}(\frac{1}{\tau_{in}}+\frac{1}{\tau_{ext}}) \tag{3.21}$$

n_g is the effective group index, τ_{in} is the intrinsic decay time (s) in rings, and τ_{ext} is the external decay time for external coupling (refer ring to the through- and drop-port coupling combined) for the mode studied. Therefore, as achieving the comb generation threshold, the cavity gain is equivalent to the loss per round trip:

$$\frac{2\omega n_2}{cA_{eff}}P_{0th}=\frac{n_g}{c}(\frac{1}{\tau_{in}}+\frac{1}{\tau_{ext}}) \tag{3.22}$$

P_{0th} is the threshold power in the microring and can be written as

$$P_{0th}=\frac{1}{2}\frac{n_gA_{eff}}{\omega n_2}(\frac{1}{\tau_{in}}+\frac{1}{\tau_{ext}}) \tag{3.23}$$

Next, the decay rate is replaced by the quality factors for intrinsic loss ($Q_i=\omega\tau_{in}$) and external coupling ($Q_{ext}=\omega\tau_{ext}$), and based on the coupling equations without drop-port geometry, the build-up intracavity power is $P_0=\frac{4\kappa_e^2}{(\kappa_e^2+\kappa_p^2)^2}P_{bus}$, where P_{bus} is the corresponding power in the input bus-waveguide. $\frac{4\kappa_e^2}{(\kappa_e^2+\kappa_p^2)^2}$ is the pump power enhancement factor of the microring at resonance. The threshold power at the input port (P_{bus-th}) is:

$$P_{bus-th}=\frac{1}{2}\frac{(\kappa_e^2+\kappa_p^2)^2}{4\kappa_e^2}\frac{n_gA_{eff}}{n_2}(\frac{1}{Q_{in}}+\frac{1}{Q_{ext}}) \tag{3.24}$$

The κ parameters here are now replaced by Eq. 3.16, and the quality factors are written as $Q_{ext}=\frac{\lambda_0}{\delta\lambda}=\frac{\lambda_0}{2(FSR/4\pi)\kappa_e^2}$ and $Q_{in}=\frac{\lambda_0}{\delta\lambda}=\frac{\lambda_0}{2(FSR/4\pi)\kappa_p^2}$. Finally, the threshold power at the bus-waveguide can be derived as [67, 68]:

$$P_{bus-th}=\frac{\pi^2Rn_g^2A_{eff}}{2\lambda_0n_2}Q_{ext}(\frac{1}{Q_{in}}+\frac{1}{Q_{ext}})^3=\frac{\pi^2Rn_g^2A_{eff}}{2\lambda_0n_2Q_{in}^2}\frac{(1+K)^3}{K} \tag{3.25}$$

where $K=Q_{in}/Q_{ext}$.

The relation between K and P_{bus-th} is shown in Fig. 3.17. For critical coupling, where $Q_{ext} = Q_{in}$, the resonant power in a ring reaches its maximum. However, if considering the threshold power for comb generation, the threshold power is minimized with under-coupling (K=0.5). Therefore, it's important to design devices with optimized coupling, where both high efficient power transfer and low threshold power are achievable.

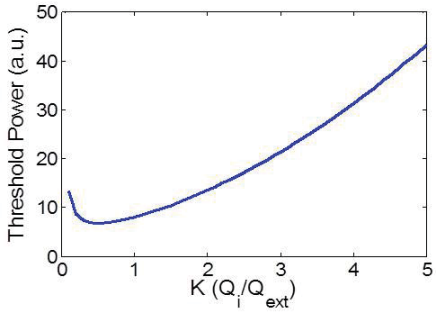

Fig. 3.17. The relation between K and threshold power at input bus-waveguide.

For devices with a drop-port waveguide, Equation 3.21 and its corresponding threshold equation could be modified as:

$$Loss/Roundtrip = \frac{(2\pi R)n_g}{c}(\frac{1}{\tau_{in}} + \frac{1}{\tau_{ext}} + \frac{1}{\tau_{drop}}) \tag{3.26}$$

$$P_{bus-th} = \frac{\pi^2 R n_g^2 A_{eff}}{2\lambda_0 n_2} Q_{ext}(\frac{1}{Q_{in}} + \frac{1}{Q_{ext}} + \frac{1}{Q_{drop}})^3 = \frac{\pi^2 R n_g^2 A_{eff}}{2\lambda_0 n_2 Q_{in}^2} \frac{(1+K+K_2)^3}{K} \tag{3.27}$$

where $K = Q_{in}/Q_{ext}$ and $K_2 = Q_{in}/Q_{drop}$.

Figure 3.18 shows the relation between measured and calculated threshold power for devices with anomalous dispersion. The thickness of the silicon nitride film is around 800 nm, suggesting the cavity dispersion is in anomalous dispersion (with waveguide width <3 μm). The calculated threshold power is estimated by the effective area of specific waveguide dimensions and the coupling parameters extracted from the low-power transmission spectra. Note here that the coupling parameters of

the resonance for the initial comb lines are assumed to be the same with the pump resonance. The capital letter 'S' in Fig. 3.18 indicates the slope between the measured and calculated threshold power. The lower limit side of the measured threshold power exhibits a close agreement with the theoretical curve (S=1). It suggests that the threshold power could be scaled and estimated based on the low-power transmission spectra. On the other hand, large variation could be observed especially for the waveguide with wide widths. One possible hypothesis is that, with more supporting modes in the wide waveguide, the coupling parameters could be altered by the unwanted mode interaction.

To conclude, the enhanced-coupling of the pump power in an initially over-coupled Si_3N_4 microresonator is identified due to the additional nonlinear mechanism for power transfer out of the pump presented by comb generation. The enhanced-coupling results in observation of comb lines stronger than the pump, for the first time at the through-port output in a chip-based microresonator. In addition, the comb threshold power and efficiency are simulated based on a simple modeling approach. This work not only helps us to design coupling optimizing power transfer to the combs but also provides a way to generate an engineering comb spectrum with a through-port geometry.

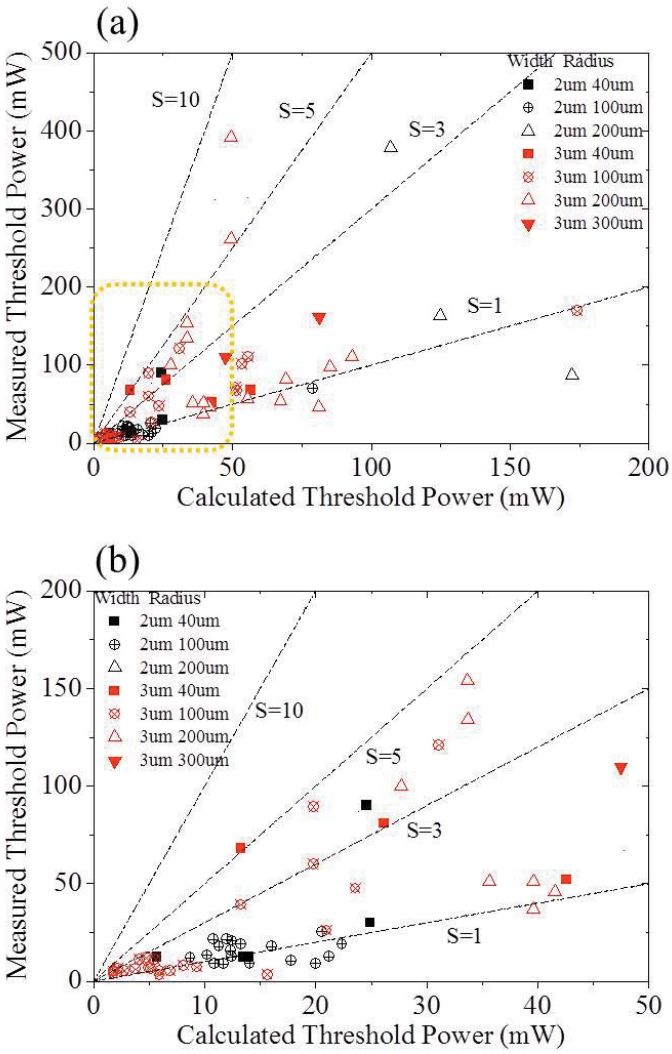

Fig. 3.18. (a)The relation between the measured and the corresponding calculated threshold power. (b)Zoomed-in area in (a).

4. TIME-DOMAIN STUDIES FOR COMB GENERATION: CHARACTERIZATION IN NORMAL AND ANOMALOUS DISPERSION REGIMES

4.1 Introduction

Optical frequency comb generation based on high-quality factor (Q) microresonators has been widely investigated for its potential in optical communication, optical clocks, and pulse generation. Most theories discussing conditions for comb formation are based on a modulational instability analysis assuming a microresonator characterized by anomalous dispersion. For instance, Ref. [30] reports a theory valid under anomalous dispersion, which predicts that initial single-FSR operation is preferred when the ratio of resonator linewidth to normalized dispersion is unity or below, while initial multiple-FSR operation is favored when this ratio is large. Another study shows the possibility to engineer comb spectra by tailoring the dispersion [25].

A few recent studies provide possible explanations of comb generation in the normal dispersion regime, either due to a modification of the modulational instability process in the presence of a cavity through pump frequency detuning, or the interactions with other mode families [69, 70]. Experimental demonstrations [28, 36] characterize the properties, such as temporal coherence and generation dynamics of the frequency combs, from normal dispersion. More recently, due to the fully understanding of the comb generation aided by mode-coupling, controllable combs have been demonstrated by selecting the pump position [71] or by tuning thermal heaters [72].

Here, a discussion of the frequency combs generated in different dispersion regimes will be given. At first, the simulated dispersion of the silicon nitride waveguide is studied. By designing different dimensions of silicon nitride waveguides, the dispersion could be tailored from normal to anomalous regime. To study the coherence of

the generated combs in different dispersion regimes, time-domain studies are later demonstrated both at the through port of an anomalous dispersion device and at the drop port of a normal dispersion device. This drop-port geometry, at least in the demonstrated cases, gets rid of the much strong pump line which is necessary to be filtered out or suppressed in through-port measurements. In addition, through mode interaction in normal dispersion, the generated comb could form a train of short, bright pulses inside the cavity with low CW background.

4.2 Simulated Dispersion in Silicon Nitride Microresonators

For frequency comb generation in microresonators, the cavity dispersion is critical for comb dynamics. It does not only affect the generation process but also the properties of the generated combs. To shed light on these issues, waveguide dispersion are simulated with a freely available software (MPB), based on fully-vectorial eigenmodes of Maxwell's equations with periodic boundary conditions [59]. The schematic diagram of the waveguide cross-section is shown in Fig. 4.1. Black area indicates the silicon nitride (Si_3N_4) waveguide while the gray area stands for the silicon oxide (SiO_2) cladding layer and substrate. The insets show the mode profiles of both fundamental and second-order transverse electric (TE) modes, where the electric field is predominantly polarized parallel to the plane of the wafer. By changing the dimension of waveguides, the dispersion could be tailored to a proper region for comb generation.

For the (total) cavity dispersion, it includes both the material (Si_3N_4) dispersion (depending on the wavelength-dependent group index) and geometrical dispersion (depending on the waveguide geometry) [31]. Figure 4.2(a) shows the refractive index of a silicon nitride thin film [73] in the C-band region while Fig. 4.2(b) shows the corresponding material dispersion.

In order to obtain the cavity dispersion, the group velocities are calculated at different wavelengths individually in MPB using the corresponding material index in

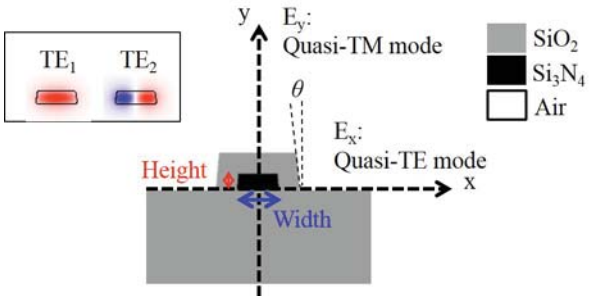

Fig. 4.1. Schematic diagram of a waveguide cross-section.

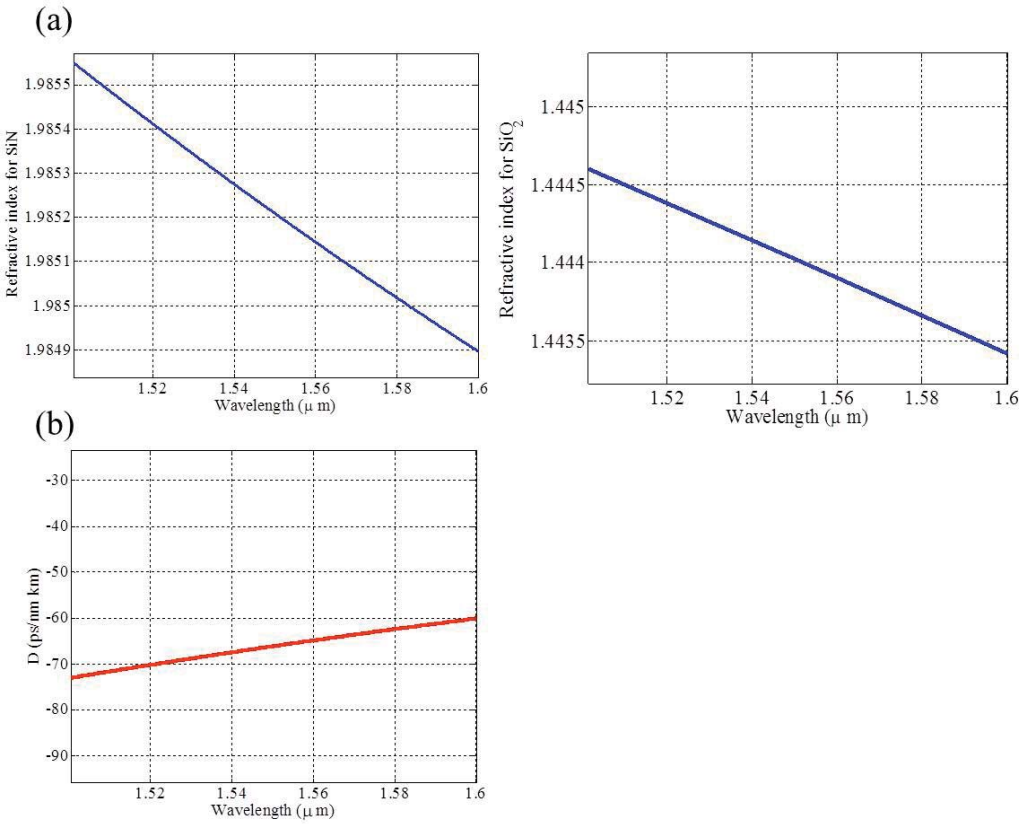

Fig. 4.2. (a) Refractive index of a silicon nitride thin film. (b) The corresponding material dispersion.

Fig. 4.2(a). The total dispersion is then determined by the fitting function of the wavelength-dependent group velocity. Figure 4.2(b) shows the material dispersion for silicon nitride. Based on the schematic geometry, several dimensions are selected with a fixed etching angle θ= 5 degree. First, the dispersion is discussed within different waveguide heights, ranging from 500 nm to 800 nm, with the same waveguide bottom width 2 μm. Figures 4.3(a) and (b) show the simulated results for both TE and TM modes.

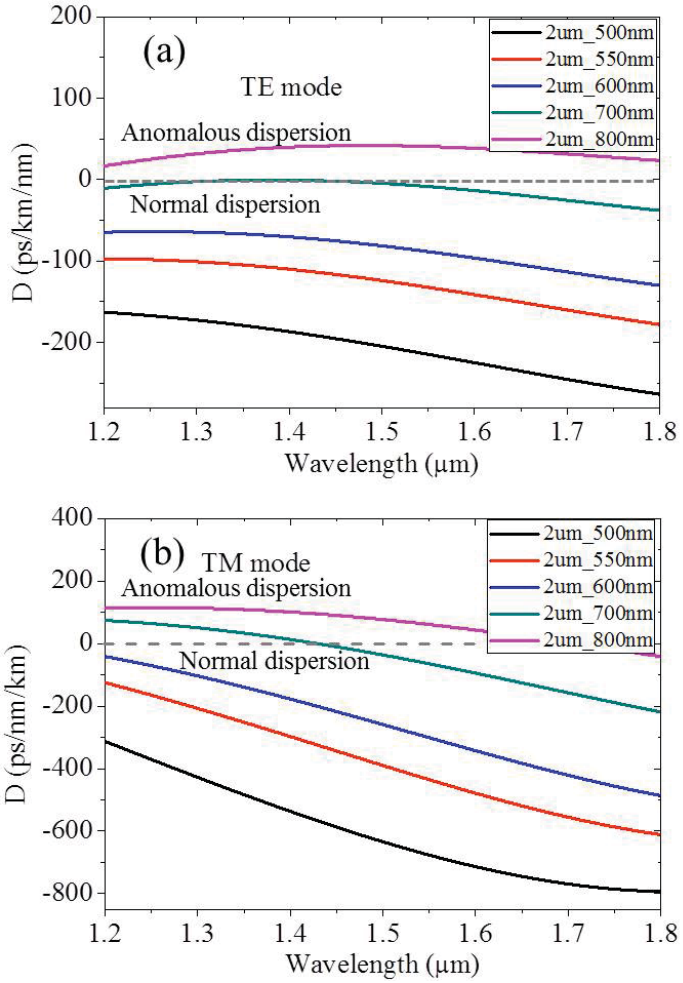

Fig. 4.3. Simulated dispersion with different heights for (a)TE and (b)TM modes. The waveguide width is 2 μm

From the simulated data, for TE mode, zero dispersion at 1.55 μm occurs with a waveguide height around 700 nm, consistent with a previous work on dispersion-engineered, anomalous dispersion silicon nitride waveguides for comb generation [27]. Thinner films are expected to exhibit normal dispersion, with anomalous dispersion possible for films thicker than about 700 nm. To further investigate the impact on dispersion, the waveguides with different widths are selected to be studied. By fixing the waveguide height at 740 nm, Figure 4.4 shows the total dispersion of waveguides with different widths. The results suggest that the total dispersion of a waveguide in C-band region is less sensitive to the width than to the height. Therefore, it is preferable to control the dispersion from normal to anomalous regimes by fabricating different film thicknesses.

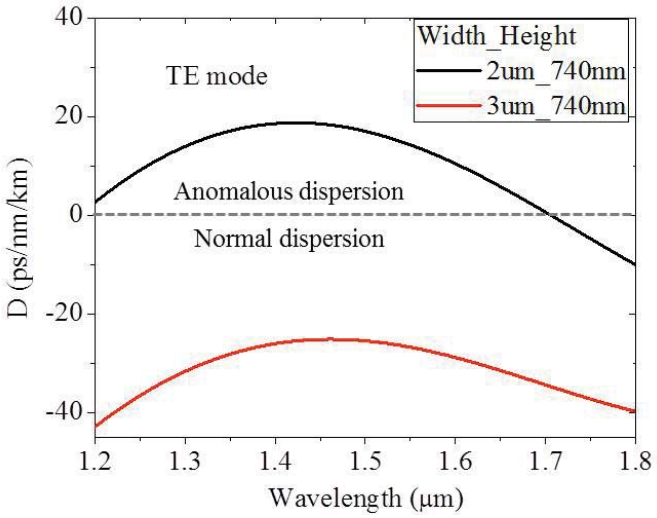

Fig. 4.4. Simulated dispersion with different widths. The waveguide height is fixed at 740 nm

These results provide clues for designing microresonator with desirable dispersion, in which both broadband and low-repetition-rate combs could be achieved. The devices with different dimensions and thus different dispersion will be characterized in the following sections. The generated combs exhibit dramatically different features in both optical spectra and time-domain characterization.

4.3 Dispersion Measurement for Silicon Nitride Microresonators

As mentioned in the previous section, the dispersion is an important factor for comb generation. Although the simulated dispersion has been discussed, it may vary based on the fabrication process and the material index. A practical way to determine the actual dispersion for individual waveguide and microresonator is essential. Several methods have been employed by previous studies. One general way is Fourier-transform spectral interferometry [74]. A wavelength-dependent modulation could be observed in the optical spectrum. The modulation frequency of the spectral interferogram is proportional to the time delay between a pulse passing through the system and a reference pulse with a delay stage; and the group index of the entire system is obtained. However, this characterization requires complicated operation. Furthermore, instead of directly measuring the dispersion from the actual ring waveguide, a long waveguide fabricated with the same dimension as the microring waveguide is needed. It limits the flexibility for characterization and also results in uncertainty.

For microresonators, the repetition rate (or FSR) directly provides clues to the group velocity and the refractive index of the ring waveguide. By extracting the group index, one can easily get the cavity dispersion. Equation (4.1) shows the relation between the FSR of microresonators and the group index.

$$FSR = \frac{c}{2\pi R n_g} \tag{4.1}$$

where c is the speed of light, R is the radius of microcavities, and n_g is the group index of the waveguide.

In [75], a novel way is proposed to accurately measure total dispersion in a microcavity. However, this method is only applicable for microresonators with FSR in microwave frequency range. Here, frequency comb-assisted diode laser spectroscopy is used for measurement of microcavity dispersion [76]. By introducing comb-based beating markers, a broadband and fast spectroscopy provides precise information of the cavity dispersion.

Figure 4.5 shows the schematic diagram for the frequency comb-assisted dispersion measurement. A tunable CW laser is sent into the microresonator and then the output from the through port is detected by a photo-detector while part of the power is used to beat with a fiber comb source (Menlo Systems). The frequency comb has a repetition rate around 250 MHz. The beating signal is divided into two paths, passing through different band-pass filters with a bandwidth 1 MHz, centering at 30 MHz and 75 MHz, respectively. By scanning the CW laser, transmission spectra of a microresonator will be recorded by the oscilloscope with 10 million sample points. Four calibration markers, located at ±30 MHz and ±75 MHz with respect to each frequency comb line, will be generated and recorded in the oscilloscope. These calibrated markers will later be used to reconstruct the absolute frequency for individual resonance peaks of the transmission spectrum. The calibrated frequency provides precise resonance positions which are typically hard to obtain with a conventional laser scanning, due to the mode hopping and uncertainty of the recorded wavelength. It then gives the precise frequency-dependent FSR and therefore the group index.

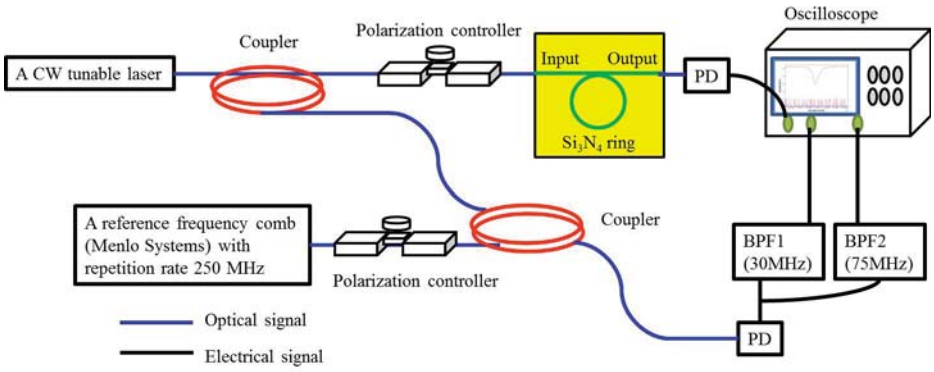

Fig. 4.5. Schematic diagram for dispersion measurement. PD: photo-detector; BPF: band-pass filter.

As discussed in the previous section, the dispersion of silicon nitride waveguide resonator is strongly dependent on the thickness of the waveguide width. Figure 4.2 shows the measured dispersion (dots) and simulated dispersion (solid lines) including both waveguide and material dispersion within the bandwidth region of interest.

Thinner films are expected to exhibit normal dispersion, with anomalous dispersion possible for films thicker than about 700 nm. This prediction is consistent with the previous works on dispersion-engineered microresonators [27, 37].

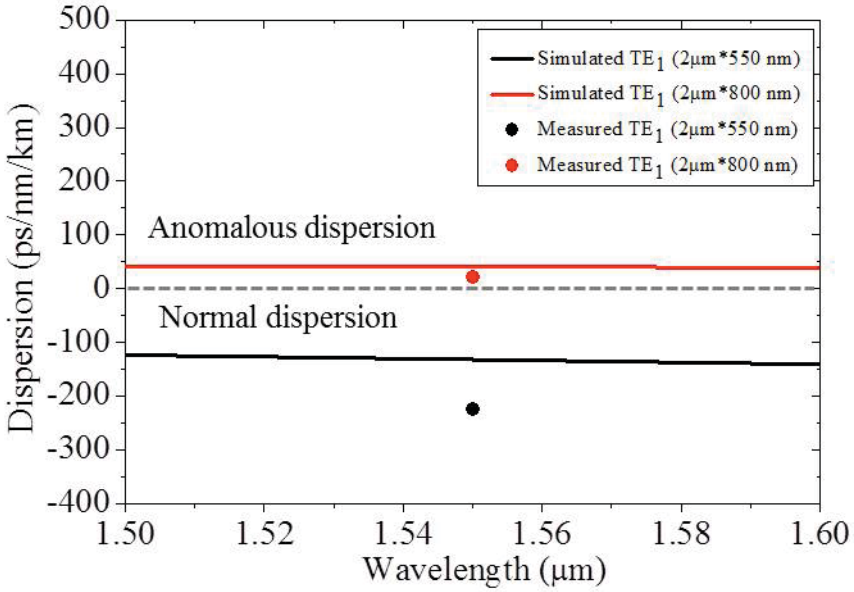

Fig. 4.6. Measured (dots) and simulated (solid lines) waveguide dispersion for two different waveguide dimensions.

4.4 Time-domain Characterization of Comb Generation

Pulse shaping experiments shed light on the time-domain behavior and especially the coherence of generated combs [26, 28], which is a crucial requirement for on-chip arbitrary waveform or short pulse generation. A recent paper [39] discussed the temporal behaviors of the comb fields directly inside microresonators; through simulations, they showed that either bright or dark cavity solitons can be initiated from microresonators, in which the behavior is depending on the dispersion regimes and pumping conditions. In this section, time-domain characterization is performed using microresonators with different cavity dispersion. Utilizing a compensated-fiber link, the intracavity field of microresonators will be investigated. A transition to a

low-noise comb through pump detuning was observed in anomalous dispersion while a train of passively mode-locked pulses with low background is observed in a normal dispersion microcavity.

4.4.1 Autocorrelation Measurements with a Compensated-fiber Link

Following the experimental procedure introduced in Chapter 2, the author studied the correlation between the spectral properties, intensity noise, and temporal coherence. By applying the pulse shaping technique in the previous studies [28, 36], a bandwidth-limited pulse could be obtained from combs that show high coherence and low intensity noise. However, the field information inside the microresonators is left unknown because the dispersion of the actual fiber leads was not compensated nor characterized. Here, to characterize the internal fields, the system is upgraded with a compensated-fiber link as shown in Fig. 4.7. The output from the chip is first sent into an erbium doped fiber amplifier (EDFA) and the amplified output is then sent through a combination of single mode fiber and dispersion compensating fiber (DCF). The length of the DCF fiber is checked by injecting a short pulse from a mode-locked laser through the system after the chip (starting at the output fiber link) [77]. The full-width at half-maximum (FWHM) of the reference mode-locked laser before the system is measured to be around 112 fs as shown in Fig. 4.8(a). The DCF length is aimed to minimize the system dispersion and therefore the measured duration of the autocorrelation trace. Fig. 4.8(b) shows the measured autocorrelation traces after the system. The intensity autocorrelation of the test pulse after the fiber link was around 368 fs FWHM (green line in Fig. 4.8(b)) without programming the pulse shaper. This is close to bandwidth-limited (302 fs), calculated by the optical spectrum after the EDFA and assuming flat spectral phase (as shown in Fig. 4.8(c)). The slight difference between the calculated and measured pulse likely results from residual higher-order dispersion. This compensated-fiber link is further checked by the line-by-line pulse shaper. By programming the individual pixels on

the shaper, the measured FWHM is ≈ 312fs after further compensation, shown in the blue line in Fig. 4.8(b). Fig. 4.8(d) shows the retrieved phase from the pulse shaper. Clearly, the phases within the bandwidth of the EDFA are almost flat and close to zero. It indicates, even without line-by-line pulse shaping, the link is approximately dispersion-compensated down to several hundred femtoseconds.

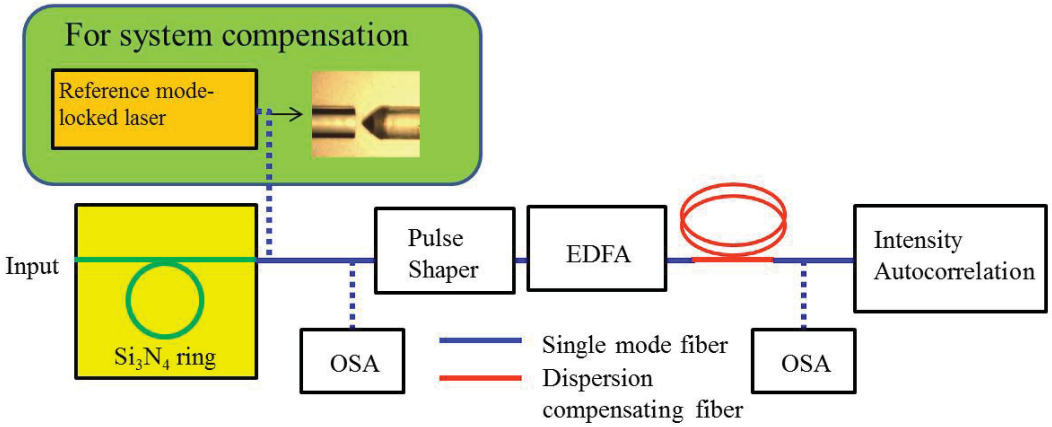

Fig. 4.7. Experimental setup with a compensated-fiber link for time-domain characterization.

4.4.2 Time-domain Measurements in Anomalous Dispersion

For comb generation in anomalous dispersion, previous time-domain experiments demonstrate generation of soliton-like ultrashort pulses from anomalous dispersion microresonators [35, 38, 40, 78]. Both analytical and simulation studies in anomalous dispersion regime also show the possibility with formation of a single soliton. [38,39,79]. In [35,38,40,78], mode-locked comb formation and dynamics are strongly dependent on the frequency detuning and pumping conditions. A noise-drop transition was observed, indicating the onset of soliton formation and mode-locked pulses [35].

To investigate the temporal coherence and intensity noise for comb generation in anomalous dispersion, a silicon nitride ring resonator with 3 μm $\times$800 nm waveguide

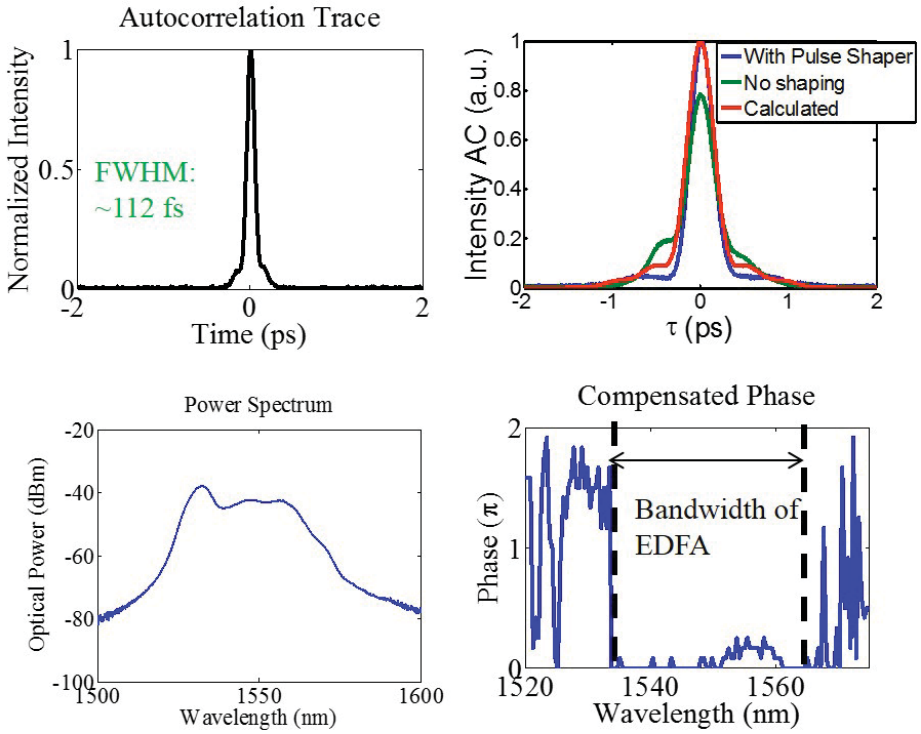

Fig. 4.8. (a)The measured autocorrelation trace of a reference mode-locked laser. (b)Measured and calculated autocorrelation traces after the subsequent system. (c)Optical spectrum after the system. (d) Compensated phase of the line-by-line pulse shaper.

cross-section and 100 μm ring radius was fabricated. The gap between the resonator and the bus-waveguide is 500 nm. Figure 4.9 shows the transmission spectrum of the quasi-TE modes, in which the electric field is predominantly polarized parallel to the plane of the resonator. The loaded quality factor (Q) for the fundamental mode, yielding high transmission contrast and high Qs, is around 1.1 million at $\approx$ 1558.17 nm (as shown in Fig. 4.9(b)). The simulated dispersion parameter is 3.3 ps/nm/km, which is close to zero but in anomalous dispersion regime.

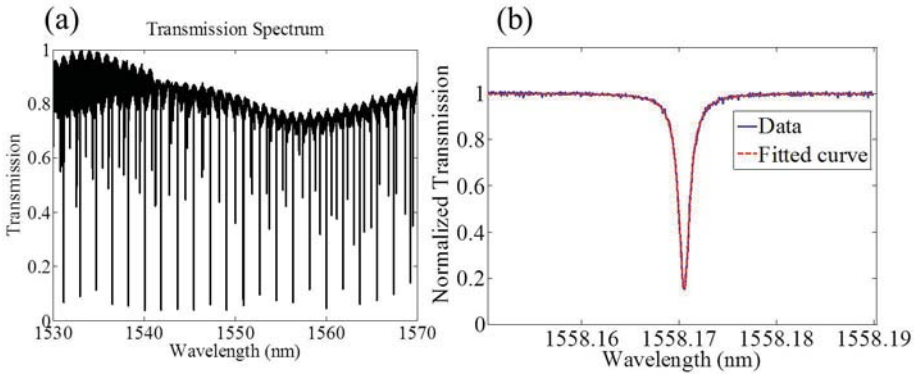

Fig. 4.9. (a) Transmission Spectrum of the microring resonator with anomalous dispersion. (b) Zoomed-in spectrum of a fundamental quasi-TE mode with loaded Q $\approx$ 1.1 million.

By increasing the input power and slowly tuning the wavelength into the resonance from the short wavelength side, frequency combs are generated once the threshold power is reached. Figure 4.10(a) first shows the comb spectrum with input power of 200 mW at around 1558.336 nm. High intensity noise is observed in the RF spectrum shown in Fig. 4.10(b). The normalized autocorrelation traces of the generated pulses are plotted in Fig. 4.10(c). Green and blue lines stand for the measured autocorrelation traces before and after line-by-line pulse compression. The calculated autocorrelation trace is shown as the red curve in Fig. 4.10(c), by taking the optical spectrum after the EDFA and assuming flat spectral phase. Clearly, this comb yields partial compressibility and poor coherence. At a later stage, as the pump is further tuned into the resonance by 2 pm (Fig. 4.10(e)), the intensity noise of the generated

comb suddenly drops, as shown in Fig. 4.10(f), without dramatically changing its comb spectrum. At this point, in the time-domain measurements shown in 4.10(g), the pulse is well compressed by the line-by-line phase correction. The measured pulses have a period of 4.44 ps, corresponding to a 225 GHz repetition rate. The comb at this stage exhibits high coherence and full pulse compressibility. It should be noted here that since the power of the pump line at the through-port spectra is much stronger than that of the adjacent comb lines, the pulse shaper is also used to attenuate the pump line by 10 dB. Figures 4.10(d) and (h) show the shaped spectra of Figs. 4.10(a) and (e), respectively, after the system.

Although showing high coherence and low intensity noise, the field of this frequency comb inside the resonator (without subsequent line-by-line pulse shaping) exhibits a noise-like variation which is different with the previous publications forming a short pulse in anomalous dispersion cavities [35, 38–40, 78].

To further examine the phase-locked transition, the repeatability of the generated intracavity field is studied after achieving low-noise transition. Figure 4.11(a) shows the measured autocorrelation traces before (red trace) and after (black trace) line-by-line phase correction. Black trace is the bandwidth-limited pulse calculated on basis of the measured optical spectrum. By repeatedly tuning the pump wavelength with fixed input power, the pump is re-locked to the resonance and the combs are initiated with low intensity noise several times. Multiple intensity autocorrelation traces are measured with the same phase applied for the compensated pulses in Fig. 4.11(a). The measured autocorrelation traces, shown in Fig. 4.11(b), exhibit a strong agreement with each other, indicating bandwidth-limited pulses. It suggests that the phase is not only stable in time but also the same while returning to the mode-locked state.

The phases applied in the pulse shaper for bandwidth-limited pulse generation allow us to determine the spectral phase for individual comb lines inside the resonator. By using the complement of the phase applied in the shaper to achieve pulse compression, the retrieved phases of individual comb lines from the resonator are shown

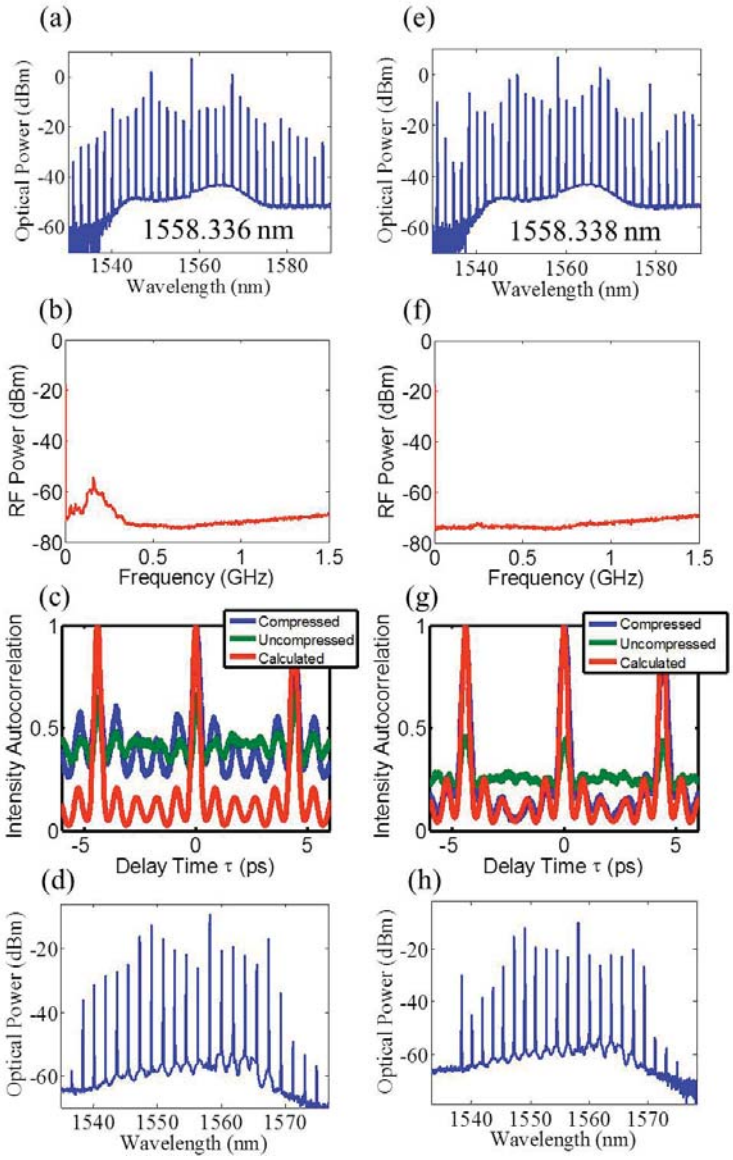

Fig. 4.10. (a)(e) Optical spectra of the generated comb at 1558.336 nm and 1558.338 nm under 200 mW input power. (b) (f) RF spectra of the generated frequency combs in (a) and (e), respectively. (c) (g) Autocorrelation traces corresponding to the frequency combs generated in (a) and (e). Green and blue lines show the measured autocorrelation traces before and after line-by-line pulse compression while red lines show the intensity autocorrelation traces calculated by taking the optical spectra after the erbium doped fiber amplifier (EDFA) and assuming flat spectral phase. (d) (h) Optical spectra corresponding to (a) and (e), respectively, after the system.

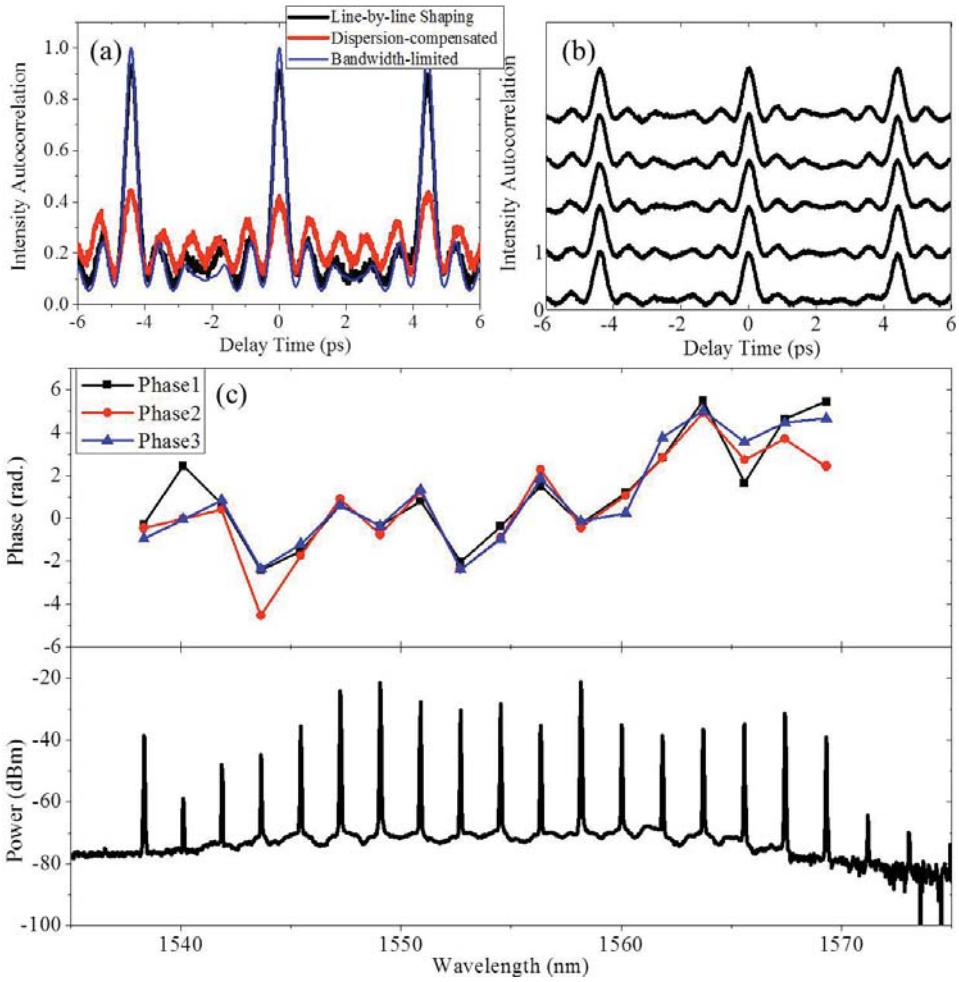

Fig. 4.11. (a) Intensity autocorrelation traces with pumping around 1558.22 nm. (b) Measured autocorrelation traces after repeatedly relocking the resonance with the same applied phase. (c) Retrieved phases of the individual comb lines from the resonator and the corresponding optical spectrum.

in Fig. 4.11(c). The phases from running the retrieving process three times after relocking are in close agreement with a deviation $0.06\times2\pi$. This confirms the accuracy of the phase-retrieved process and the correctness of the obtained comb spectral phase. This also implies, as mentioned before, the spectral phase is identical after relocking the resonance. The deviation may be correlated to the relative output power per comb line. The phase retrieved here is independent of a constant offset, and a linear spectral phase term is subtracted off (which just results in the time delay for the time-domain waveform [49]).

In this coherent comb state, the optical spectrum and the the retrieved spectral phase (Fig. 4.11(c)) help reconstruct the field information inside the ring through Fourier transform. The calculated intensity internal to the ring is shown in Fig. 4.12(a), while the corresponding phase of the field is shown in Fig. 4.12(b). Five oscillating peaks are found per round trip time, indicating a complexly structured waveform. It is worth to note here that the background level of the intensity in the microring is still uncertain, since it is difficult to know in a through-port device how much of the strong pump line observed at the output port is present inside the resonator. However, the results show a complexly structured internal comb field in strong contrast to the previous observations reported in [35, 38, 40, 78], where measurements suggested the presence of well-formed pulses directly in the microresonator. In addition, instead of utilizing the whispering gallery modes in a microrod resonator [80], the stable phase-locked microcomb state is now operated in a silicon nitride ring resonator on chip-level scale. Unlike the existence of distinct phase distributions for different phase-locked states in [80], the phase here is stable and identical even after re-locking the resonance and forming the coherent combs.

To further study this mode-locked transition, another resonance was investigated by pumping at around 1562.08 nm, belonging to the same mode family previously discussed. Figure 4.13(a) shows the optical spectra while the corresponding RF spectra are shown in Fig. 4.13(b). The initial sidebands first start with 6-FSR spacing, showing the same behavior with that observed in the previous resonance. It indicates

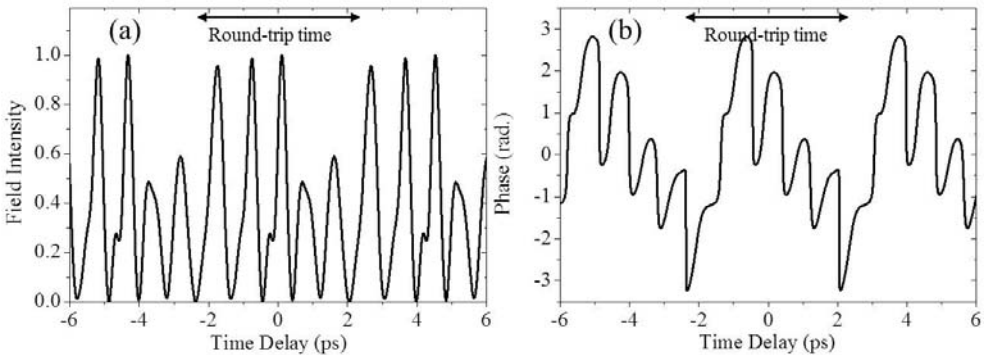

Fig. 4.12. (a) The calculated intensity internal to the ring. (b) The corresponding phase of the field.

that, unlike the comb in normal dispersion typically exhibiting a dramatic change by pumping at different resonances [28, 37, 70], the combs demonstrated in anomalous dispersion are more likely to generate the first pairs of combs with the same initial spacing. This supports that, in anomalous dispersion, the modulational gain dominates the comb generation at threshold; while in normal dispersion, the position of initial sidebands is mainly determined by the mode interaction [70]. Similar low-noise transition is observed with detuning the pump a few picometers from blue to red. For time-domain characterizations, Figures 4.13(c) and 4.13(d) show the corresponding autocorrelation traces with respect to the comb generation pumping at 1562.080 nm and 1562.084 nm. The insets are the corresponding filtered spectra after the pulse shaper. In this case, a portion of the optical spectrum centered around 1552 nm is selected for characterizing the time-domain waveform. Again, the comb with high intensity noise exhibits poor temporal coherence while the comb after low-noise transition shows full compressibility and high coherence. Similar to that pumping at 1558.34 nm, a coherent but complexly structured internal comb field is observed.

4.4.3 Mode-coupling in Normal Dispersion for Comb Generation

Recently, several new findings of frequency comb generation have been reported in normal dispersion. Through the freedom of pump detuning [69] or the mode interaction [66, 70, 71], Kerr combs are allowed to generate in normal dispersion cavity. However, the spectral properties of the generated combs could be significantly different from that initiated in anomalous dispersion through the modulational instability. Dramatic difference of the comb spectra is experimentally observed by simply shifting the pump by one single resonance (or one FSR) in normal dispersion cavity [28, 37]. Such behavior has also been observed in [70] and explained on the basis of interaction with different mode families, which can produce strong local disturbances in dispersion. Figure 4.14(a) shows the comb generation at the threshold under different

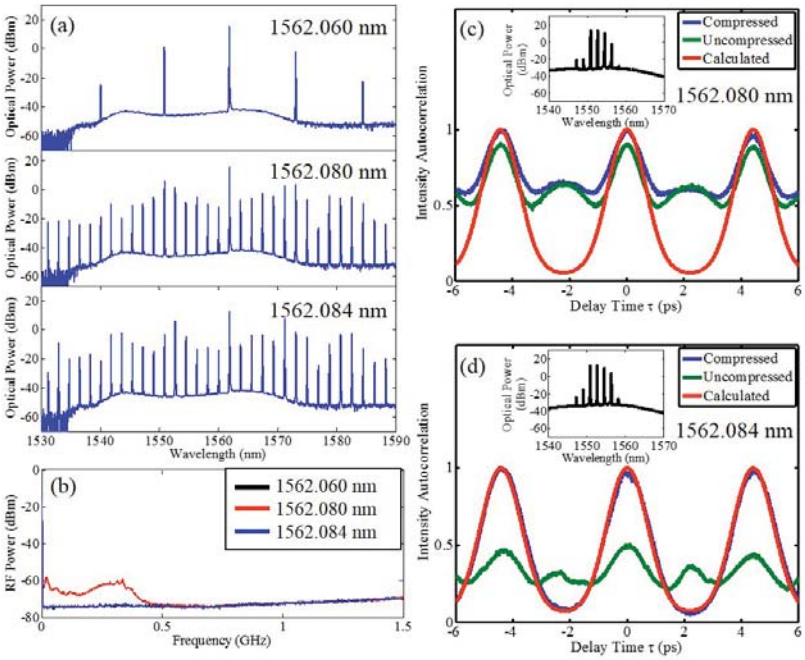

Fig. 4.13. (a) Optical spectra at different pump wavelengths. (b) The corresponding RF spectra of the generated combs. Intensity autocorrelation traces are shown (c) before and (d) after low-noise transition. (c) and (d) insets are the corresponding filtered spectra after the pulse shaper.

pumping wavelengths in a normal dispersion cavity. This device used here is the same one previously discussed in Chapter 3.

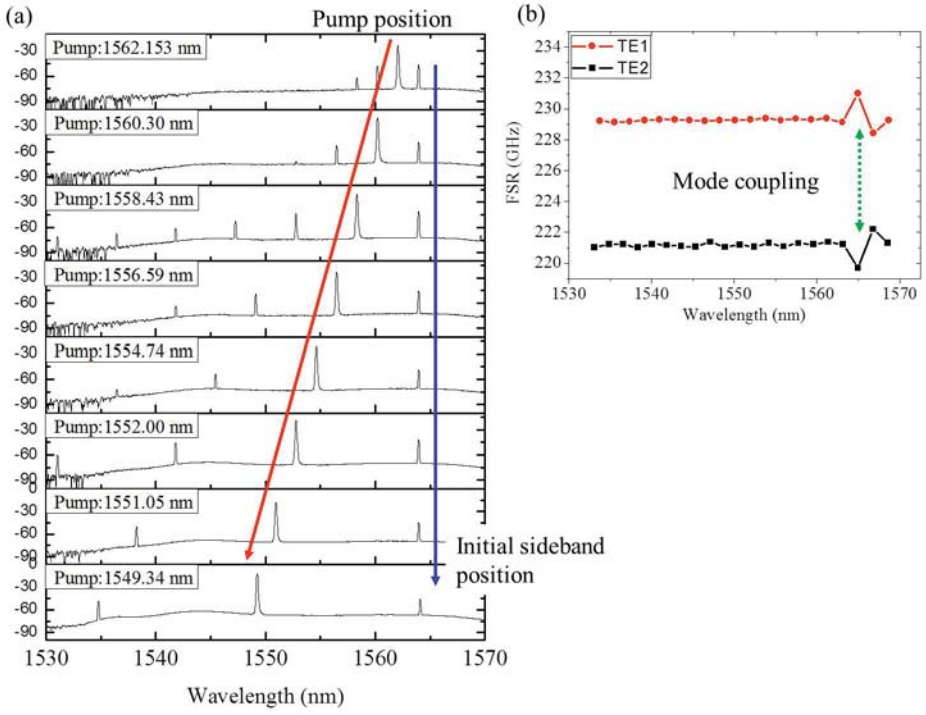

Fig. 4.14. (a) Comb generation at threshold under different pumping wavelengths in a normal dispersion cavity. (b) The measured FSRs for both TE1 and TE2 modes.

Clearly, the initial sidebands of combs at threshold tend to generate around 1564 nm, where a large variation could be identified in the measured FSR (Fig. 4.14(b)) from the cold-cavity transmission spectrum. The FSRs for both TE1 and TE2 modes are shown in Fig. 4.14(b). This pinning effect in comb spectra and the variation of FSR show strong evidences that for this normal dispersion cavity, comb could be initiated through mode-coupling and local dispersion change.

4.4.4 Time-domain Measurements in Normal Dispersion with a Drop-port Geometry

As demonstrated before, comb generation in anomalous dispersion typically contains a strong pump line, 20 dB or more above the adjacent comb lines. An analytical investigation of mode-locked combs also predicts a large CW background at the through port associated with a strong residual pump [81]; the solutions presented explicitly include a CW component internal to the microresonator. As for normal dispersion, a complex waveform with significant background and a smooth intracavity spectrum was predicted [69]; meanwhile in Ref. [70], a smooth spectrum is identified. However, the existence of a continuous background field inside the cavity has not been verified yet. Although some experimental spectra do exhibit a strong pump line, this may be associated with the strong pump field transmitted directly from the input waveguide in the through-port configuration. This issue may be important for future on-chip comb applications.

Although the spectral properties for normal dispersion have been well studied in Chapter 3 with the aid of a drop-port geometry, in time-domain studies, it still lacks adequate information for intracavity fields. Ref. [39] shows that the comb in normal dispersion may form a dark soliton with a strong background field. Some studies [28, 42] show that low background level ultrashort pulses are possible at the through-port measurements through external line-by-line pulse shaping, while Refs. [35,38] reported generation of ultrashort pulses directly in the microresonator, considering devices with anomalous group velocity dispersion. However, in all of these time-domain experiments, suppression of the very strong pump line present at the through port was necessary for pulses with a low background field. Reference [35] used a spectral filter to select a region of the comb away from the pump region for characterization, while in [26, 28, 38, 42], similar to the time-domain measurements in the previous section, a pulse shaper or fiber-Bragg grating was used to attenuate the pump line. This strong pump line observed in the through-port data may be linked to non-optimized coupling

or the dynamics of comb generation. It does not only limit the comb characterization for the intracavity field, but also gives rise to a strong background field in time-domain measurements.

To address these issues, a drop-port geometry is again used here to identify the spectra inside the microresonators. As illustrated in the previous chapter, by observing the output from the drop port, the comb fields internal to the microring can be directly probed. This avoids a complication inherent in the through-port data, for which the output pump light depends on the interference between the field coupled out of the microresonator and the field directly transmitted from the input bus-waveguide. Without the need to filter out or suppress the strong pump as was necessary in previous through-port experiments [26, 28, 35, 38, 42], it is possible to directly probe the internal field inside the microresoantor and also generate low background level ultrashort pulses through external line-by-line pulse shaping. Furthermore, the system is utilized with a compensated-fiber link as introduced in the previous section. Therefore, this enables us to characterize not only the spectrum properties but also the temporal behaviors internal to the microrings.

The drop-port device used here is the same one previously discussed in Chapter 3. The resonator is fabricated with 2 μm $\times$550 nm waveguide cross-section and 100 μm radius, designed in normal dispersion regime. The drop-port spectra generated from this device are again plotted in Figs. 4.15 (the same data with the red lines shown in Figs. 3.6) with pumping power 430 mW at around 1558.5 nm and 680 mW at around 1558.8 nm. From these drop-port data, the comb lines exhibit a degree of smoothness rarely observed in previous through-port data. It indicates that, at least in a normal dispersion cavity, a smooth spectrum may be obtained directly from the microrings.

Figures 4.15(c) and (d) show the autocorrelation traces corresponding to the comb generation in Figs. 4.15(a) and (b) respectively. The red traces show the intensity autocorrelation traces calculated by taking the optical spectrum and assuming flat spectral phase, while the green and blue lines show the measured autocorrelation

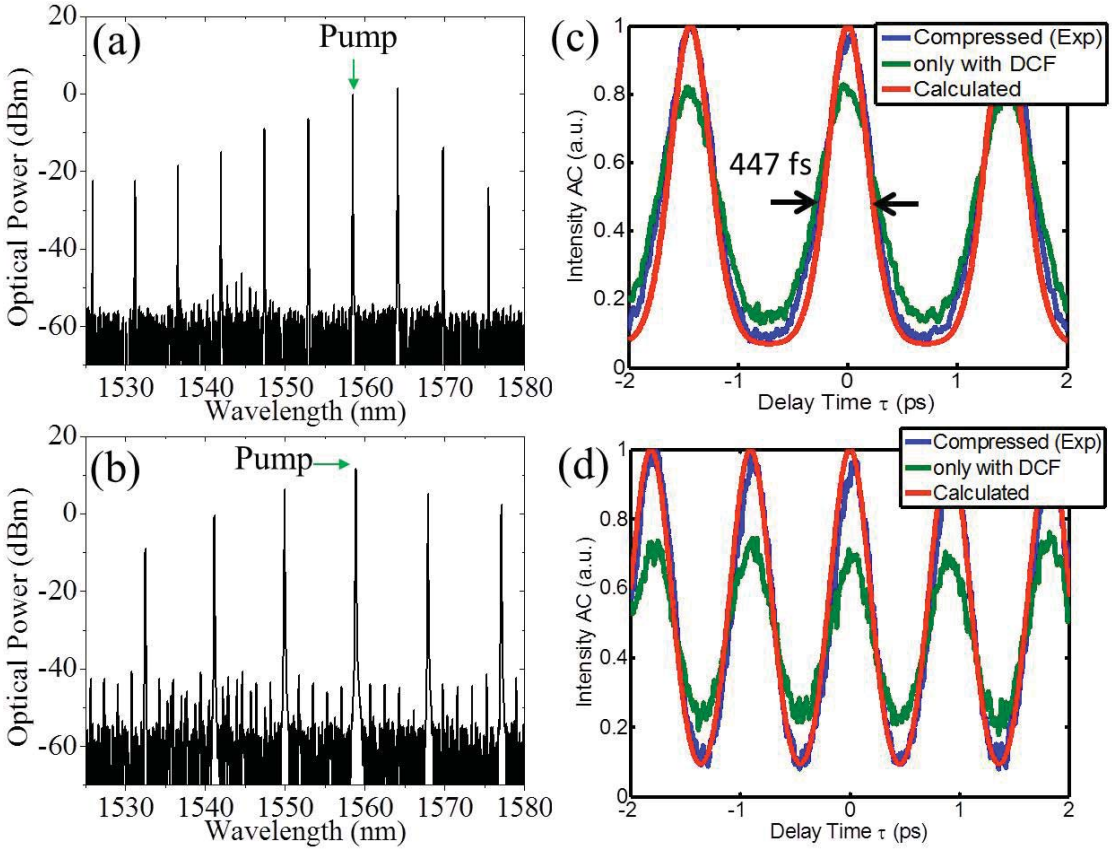

Fig. 4.15. Measured optical spectra at the drop port with input power (a) 430 mW at around 1558.5 nm and (b) 680 mW at around 1558.8 nm. The corresponding autocorrelation data are shown in (c) and (d), respectively.

traces before and after the line-by-line phase correction. A pulse shaper is placed before the EDFA to fine-tune the spectral phase but without modifying the shape (intensity) of the optical spectra. For both cases, the measured autocorrelation traces after fine-tuning the phase (blue traces) are in close agreement with the calculated one. It indicates that the demonstrated combs have high level of temporal coherence, in accord with the previous studies of combs generated directly at multiple-FSR spacing (Chapter 2). The second finding is that for the first case in Fig. 4.15(c), a pulse-like intensity autocorrelation is directly obtained without line-by-line pulse shaping. The measured pulse train has a period of 1.45 ps, corresponding to a 689 GHz repetition rate, consistent with the comb spacing of 5.52 nm (3 FSRs). Comparing with the simulated curve from the optical spectrum after EDFA, the experimental and calculated traces are close but not perfectly matched; the FWHMs of the experimental and calculated traces are 526 fs and 423 fs, respectively. One possible reason is that the measured pulses here are short enough that residual higher-order dispersion in the compensated-fiber link causes the broadening. Another possibility is that for this case the field internal to the microring is itself slightly broadened compared to a bandwidth-limited pulse.

For other resonances, dramatic examples of pulse-like intensity autocorrelation are obtained in the same device. By pumping at 1 W pump power around 1560.4 nm, a comb with single FSR could be directly generated, which is termed as a Type I comb in Chapter 2. The optical spectrum is shown in Fig. 4.16(a) while Fig. 4.16(b) shows the corresponding RF spectra. Clearly, the generated comb exhibits low intensity noise by comparing the background noise of the RF spectrum analyzer. The optical spectrum after the EDFA, without programming the amplitude of the pulse shaper, is shown in Fig. 4.17(a). Note that since a drop-port geometry is applied, the optical spectrum, at least the one discussed here, could be smooth, in which the pump power is comparable to that of the comb lines.

The measured autocorrelation trace, plotted as the blue line in Fig. 4.17(b), matches well with the trace simulated assuming flat spectral phase (green trace). It

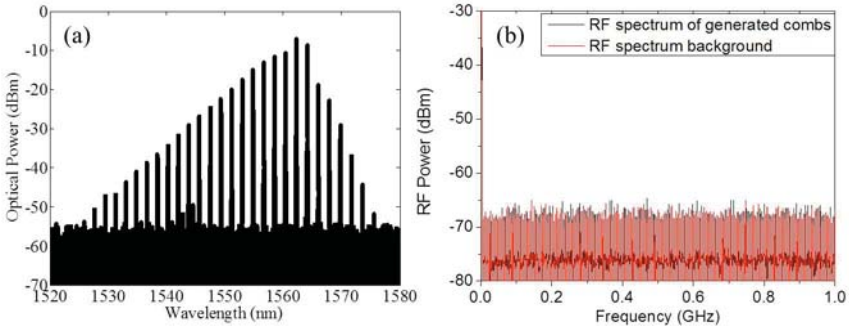

Fig. 4.16. (a) A Type I comb at 1 W pump power around 1560.4 nm. (b) The corresponding RF spectra.

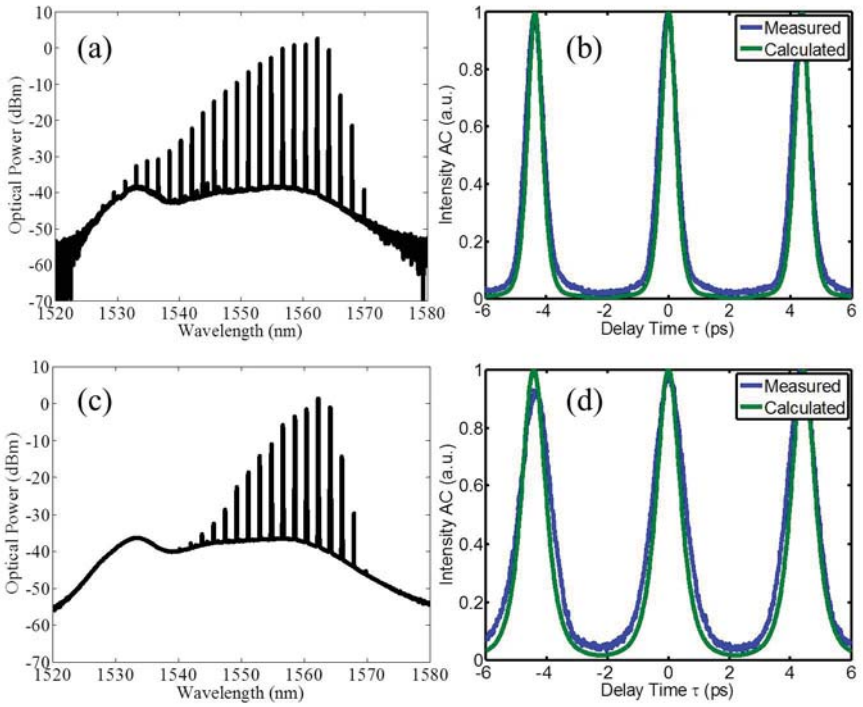

Fig. 4.17. (a)(c) Optical spectra after the system (including the EDFA) by pumping 1 W at 1560.4 nm and 700 mW at 1562.2 nm. Smooth spectra are observed. (b)(d) The corresponding autocorrelation traces.

indicates that the field inside the microring contributed a short pulse with a low CW background component. The minimal value between two peaks of the autocorrelation trace is only around 2% of the peak value. The pulses have a period of 4.35 ps, corresponding to a repetition rate 230 GHz of the microring, consistent with the 1.84 nm comb spacing, with a measured autocorrelation width $\approx$ 698 fs FWHM. Another similar pulse-like intensity could be also observed at 700 mW pump power at around 1562.2 nm (belonging to the same mode family with the previous one). The optical spectrum and autocorrelation traces are shown in Fig.4.17(c) and (d), respectively. Again, smooth spectrum is obtained without programming amplitude in the pulse shaper. The minimal value of the measured trace is 4% of the peak value. For both cases, the measured autocorrelation traces show close agreement with the simulated curves assuming bandwidth-limited pulses inside the microresonator. Also, it should be noted here, the pumping region at 1562 nm is close to the regime where mode-coupling and large variation of FSR could be identified (as discussed in the previous section). Therefore, the initial comb lines tend to occur with single FSR spacing from the pump and form a type I comb. Here with the aid of the mode-coupling, a comb in normal dispersion cavity provides the ability to generate a short pulse train directly from the microring without further shaping the spectra. It also suggests the possibility to implement on-chip pulse generators for integrated photonics.

5. LOW-NOISE TRANSITION AND SOLITON FORMATION IN ANOMALOUS DISPERSION

For time-domain studies, a critical issue is to form a comb with high temporal coherence. With studies on different microresonators, the routes to comb generation, Type I and II combs [36,42] or MMS and NMS combs [30], have been well discussed. Recently, the short pulse generation has been demonstrated both in normal [37] and anomalous dispersion cavities [35, 38]. In normal dispersion, coherent combs may be generated through local dispersion modification between different mode families [66, 71]. However, the spectral bandwidth in normal dispersion is typically limited compared with that measured in anomalous dispersion. In addition, due to the mode-pinning effect, the pump position for a single-FSR comb is critical and can not be easily adjusted without an external thermal heater [72]. In contrast, based on modulational instability theory, several works have focused issues on comb spectral properties in anomalous cavity dispersion [25, 30]. Similar to the observation in fiber-based cavities, studies have showed the possibility to obtain passive mode-locking of the comb consistent with soliton-pulse formation under anomalous dispersion [35, 38, 78, 82–84] on a balance of cavity dispersion and nonlinearity, providing coherent, broad bandwidth, and low-noise comb operation. In this chapter, a mode-locking behavior will be demonstrated in anomalous dispersion cavity. Unlike a noise-free comb at the beginning of comb formation in normal dispersion, frequency combs in anomalous dispersion transition from chaotic Type II comb formation to a mode-locked state. The mode-locked transition for comb generation will be correlated with the transmission spectra and the response of the comb power. Meanwhile, a smooth, broadband spectrum shows the evidence of a single soliton formation, which has only been demonstrated on chip by a few groups using a through-port geometry [78, 82]. With the aid of a drop-port geometry, the pump detuning, spectral phase, intracavity power and the power trans-

fer between the through and drop port could be well identified for the demonstrated soliton formation. A short bright pulse close to a transform-limited pulse could be clearly observed in the cavity with that the spectral phase of the pump is close to that of the adjacent combs.

5.1 Simulated Soliton in Anomalous Dispersion

Figures 5.1 shows a simulated example of soliton formation in an anomalous dispersion cavity. The simulation is performed by utilizing the standard Lugiato-Lefever model [85], written as:

$$t_R \frac{dE}{dt} = [-\alpha - i\delta_0 - iL\frac{\beta_2}{2}\frac{d^2}{d\tau^2} + i\gamma L|E|^2]E + \kappa_e E_{in} \tag{5.1}$$

where κ_e is the bus-waveguide coupling coefficient, t_R is the cavity roundtrip time, α is the roundtrip cavity loss (including both intrinsic loss and coupling loss), δ_0 is the pump detuning, L is the roundtrip length, and β_2 is the cavity dispersion. Intense studies have investigated the Kerr comb formation based on this spatiotemporal formalism [39, 79, 81, 86], which provides an efficient way to study both time and frequency dynamics for Kerr frequency combs with a large mode number. By fine-tuning the laser wavelength, a single soliton per round trip could be generated in a 100 μm silicon nitride resonator. The intensity and the corresponding optical spectrum are shown in Fig. 5.1. The parameters for the Lugiato-Lefever model are listed in Table 5.1, which are moderate values for a silicon nitride waveguide resonator. Similar to those observed in the previous findings, a smooth spectrum is found accompanying with a strong pump line. Figure 5.1(b) inset shows the central part of the zoomed-in spectrum.

This example shows the opportunity to form a single cavity soliton on a balance of cavity dispersion and nonlinearity of the silicon nitride waveguide. Furthermore, it provides a way to design a proper device for single soliton operation.

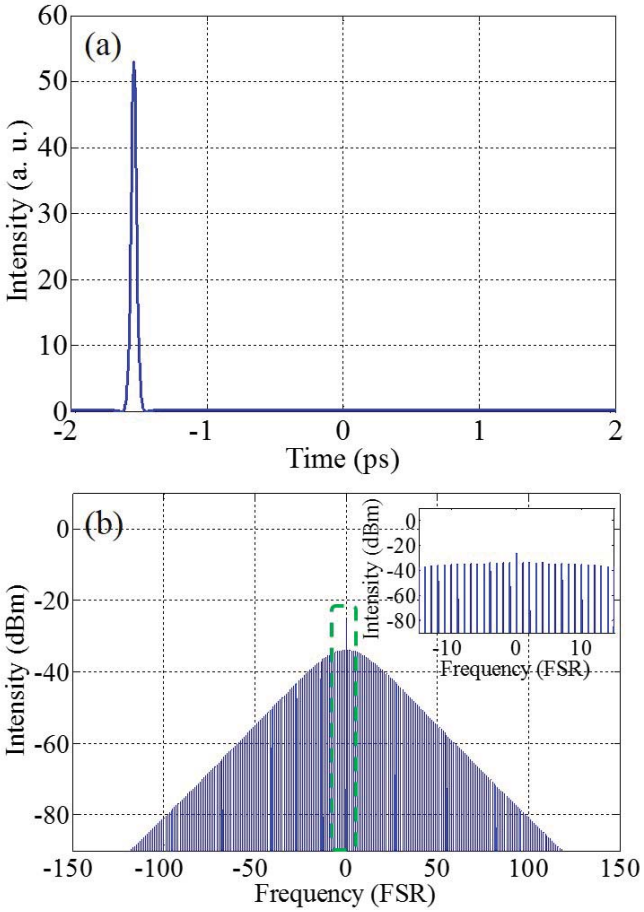

Fig. 5.1. Simulated soliton based on the Lugiato-Lefever model. (a) The intensity profile of a single soliton and (b) the corresponding comb spectrum inside the microresonator.

Table 5.1
Parameters for the Lugiato-Lefever model

Parameters	value
Nonlinear parameter $\gamma(W^{-1}m^{-1})$ [34]	1.4
Intrinsic loss (κ_p^2)	1.7×10^{-3}
Coupling (κ_e^2)	4.8×10^{-4}
Dispersion (ps^2/km)	-51
Cavity roundtrip time (ps)	4.2
Roundtrip length (μm)	$2\pi \times 100$

5.2 Low-noise Transition with Pump Detuning

5.2.1 Correlation between Transmission Response and Noise Transition

A phase-locked Kerr comb generation has been widely observed in anomalous dispersion cavity with fine-tuning the pump wavelength. This phase-locked behavior could be either mode-locked [35, 38, 40] or without mode-locking [80, 87]. A recent study [88] shows the possible pathway to avoid the chaotic regime for mode-locked frequency combs in anomalous dispersion, which provides the possibility to generate combs with low intensity noise and high coherence. In the early part of this thesis, experimentally a phase-locked comb in anomalous dispersion is observed without forming a short pulse by red-shifting the pump line. However, there is no clear evidence and clues to address this operating regime. Here, to study the noise-free transition for micro-comb generation, high power transmission spectra are studied. As demonstrated by Ref. [38,82,90], multiple steps could be observed in transmission spectra in the form of soliton formation. Figure 5.2 from Ref. [38] shows the exemplary transmission spectra and the corresponding comb generation. The evolution in high power transmission spectra provides a possible pathway for coherent comb generation.

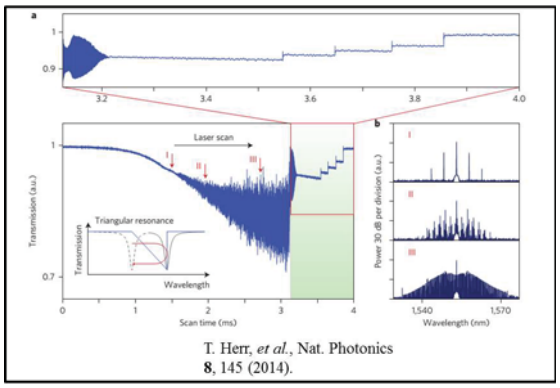

Fig. 5.2. Transmission spectra and the corresponding comb generation from Ref. [38].

To address these issues, a silicon nitride microring with 100 μm radius is used to study the comb evolution under different pump detuning. A correlation between

the transmission and low-noise transition is investigated in this anomalous dispersion cavity. The cross-section of the silicon nitride waveguide is fabricated with 800 nm (height)×2 μm (width). The average intrinsic quality factor for the fundamental TE mode (TE1) is around 1.5 million. Figure 5.3 shows the measured FSRs for the corresponding mode across C-band region. The FSR is measured by utilizing the frequency comb-assisted measurement as discussed in the previous section, while the scanning speed of the tunable CW laser is set at 10 nm/s. The fitting curve shows the dispersion D≈ 20 ps/nm/km, suggesting this cavity is in anomalous dispersion regime. This measurement is also in close agreement with that simulated data by MPB (D≈ 40 ps/nm/km).

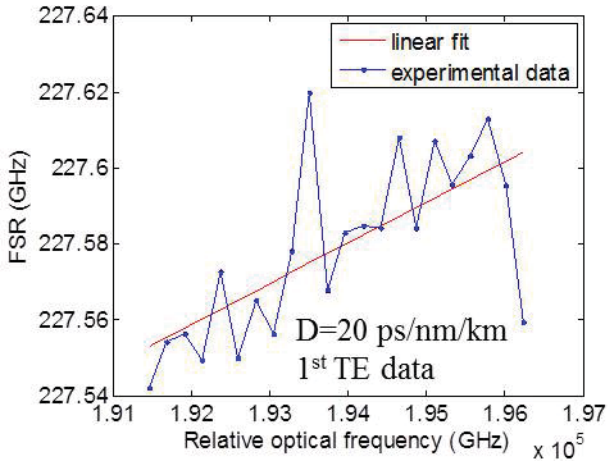

Fig. 5.3. Measured FSR variation for a 800 nm (height)×2 μm (width) silicon nitride waveguide.

The comb generation at different resonances of TE1 mode is shown in Figs. 5.4 (without low-noise transition) and Figs. 5.5 (with low-noise transition) by pumping at 200 mW input power. The spectral resolution is set at 0.1 nm while a commercial wavemeter (Menlo Systems) is utilized to determine the pump wavelength down to sub-picometer scale. The first columns in both Figs. 5.4 and Figs. 5.5 show the comb generation with large intensity noise while in Figs. 5.5, the low-noise combs (as shown in the second column) are possibly found by red-detuning the pump wavelength. The

measured intensity noise and high-power transmission response are shown next to each optical spectrum. To measure the intensity noise from the micro-combs, the comb is first sent into a photo-diode with 12 GHz bandwidth and the electrical signal is then amplified by an electronic amplifier with 500 MHz bandwidth. The resolution bandwidth of the ESA is set at 100 kHz. The transmission response is measured by sweeping the pump line 40 nm/s (200 mW, which is used for comb generation) and recorded at the through-port data by an oscilloscope. Meanwhile, the response of the generated combs is also measured by filtering out of the pump line. It should be noted that the manually detuning speed for comb generation in the previous Chapters is typically less than 1 pm/s, which is much slower than that used in the transmission spectra. First, as typical Type II comb formation, Figures 5.4 show the spectra where no low-noise comb could be observed even by manually fine-tuning the laser with a sub-picometer step. The corresponding transmission responses exhibit a regular triangular shape induced by the thermal bistability. Similar to that observed in Ref. [38], significant noise could be identified in the final stage of the chaotic comb generation (as shown in the lightgreen region in Fig. 5.4). The response of generated combs (the fourth column of Figs. 5.4) exhibits similar dynamics. As the laser is further red-detuned with 40 nm/s sweeping speed, a transition could be observed in the transmission spectrum, suggesting stable comb operation (as shown in lightyellow region). However, the comb could not be stably stayed in this regime by fine-tuning the laser wavelength manually. This could be explained by the relatively narrow (less than 1 picometer) region for low-noise transition.

In other cases, a transition to low-noise spectra is observed after fine-tuning the laser wavelength within a few picometers. As shown in Figs. 5.5, for each pump resonance, the transmission response now produces obvious steps followed by the resonance dip. Compared with the previous cases (Figs. 5.4), the stable comb regimes, marked with lightyellow, exhibit a broader range, up to several picometers. It shows a strong correlation between the range of stable-power response in transmission and the feasibility of low-noise comb generation. Moreover, Figs. 5.6 show the exemplary

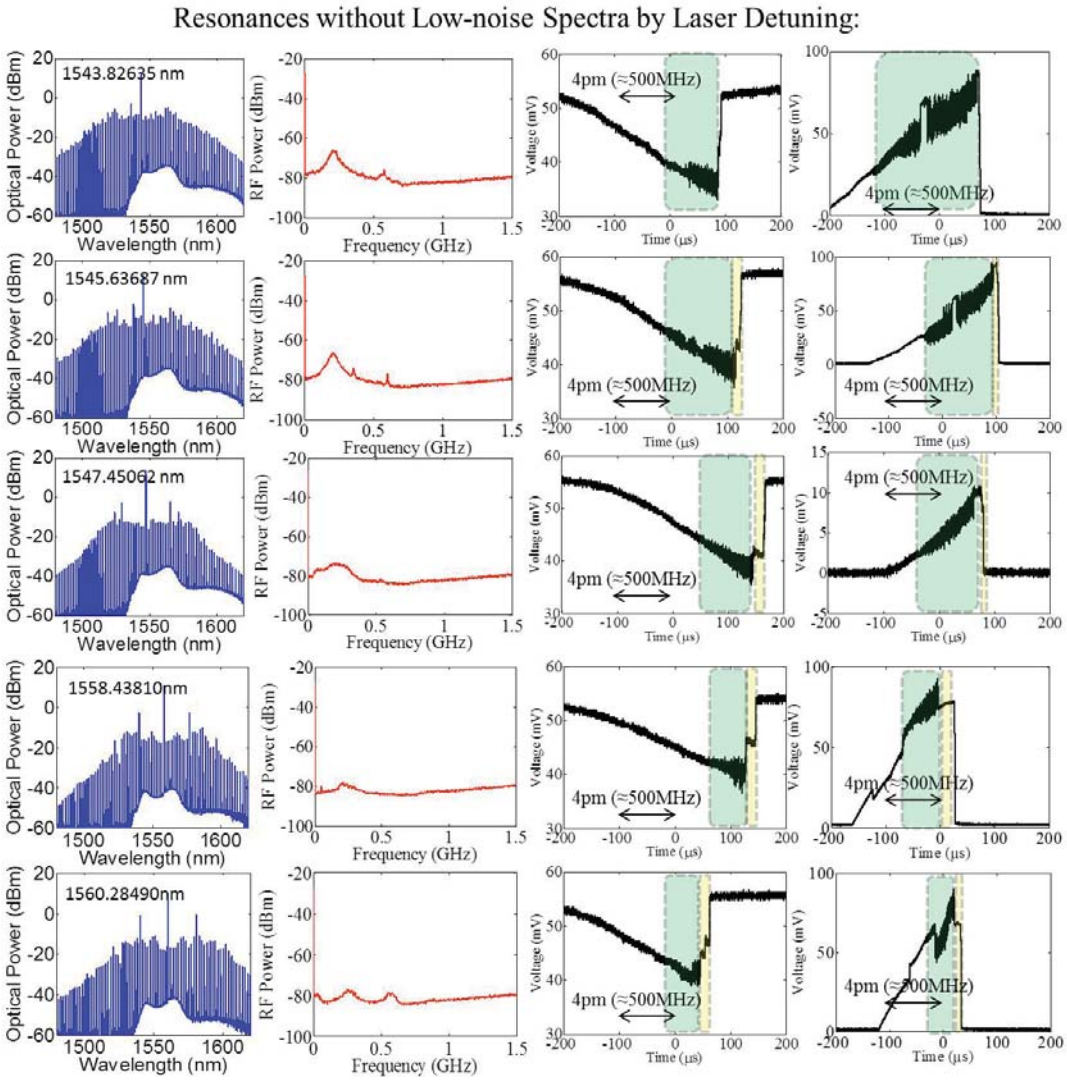

Fig. 5.4. Optical spectra, intensity noise, and transmission responses for the individual pumping resonance. The rightmost parts show the transmission response by filtering out of the pump line at the output.

transmission by sweeping the pump laser around 1551.1 nm. In detail, the zoom-in spectra (Figs. 5.6(b) and (d)) show clear multiple steps implying the soliton evolution in anomalous dispersion regime, where each step corresponds to the successive reduction of soliton number each round trip in the microresonators [38, 78, 89]. This identification of a series of discrete steps in the transmission could only be observed in anomalous cavities. However, the range for each step demonstrated here is less than 0.2 picometer in this resonator and it is hard to reach stably for the comb generation. To further address this difficulty, a pump-modulation process will be discussed later in this chapter.

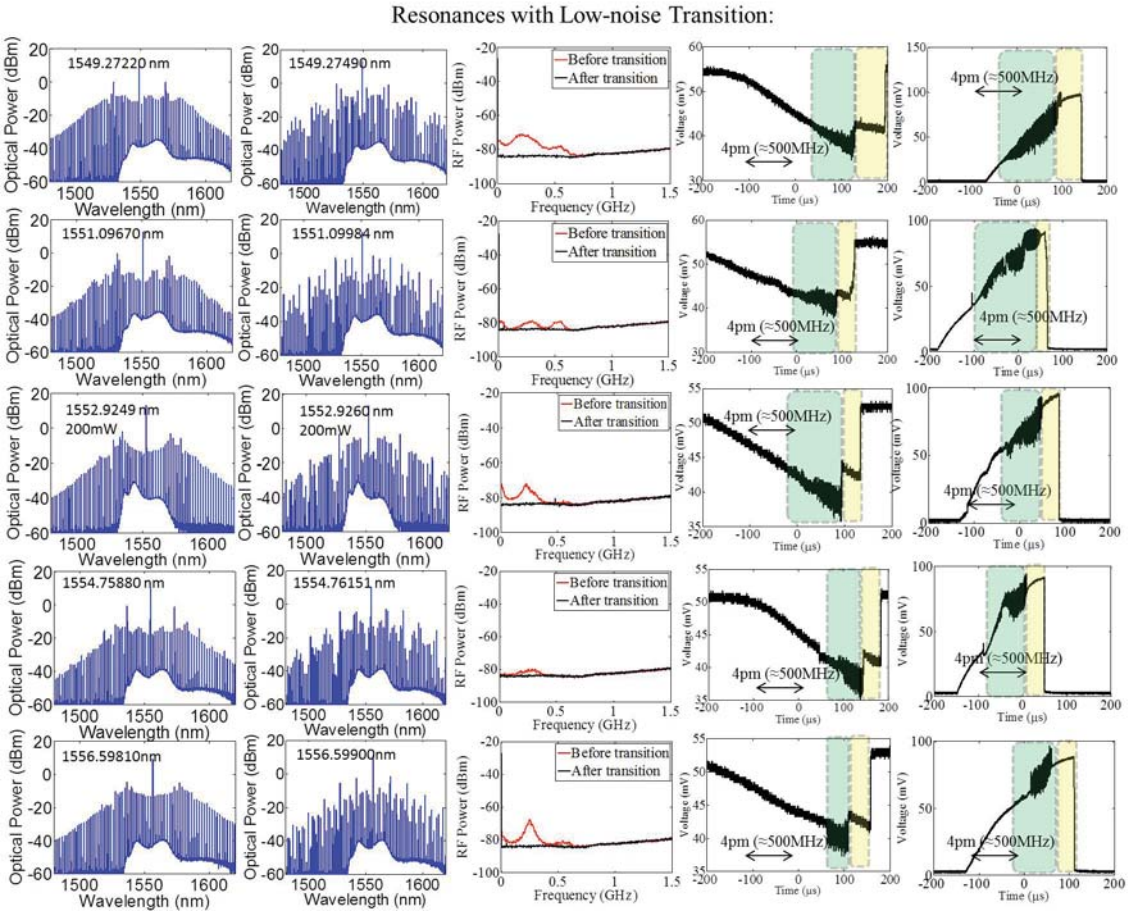

Fig. 5.5. Optical spectra before and after low-noise transition, intensity noise, and transmission responses (with pump 200 mW) for the individual pump resonance.

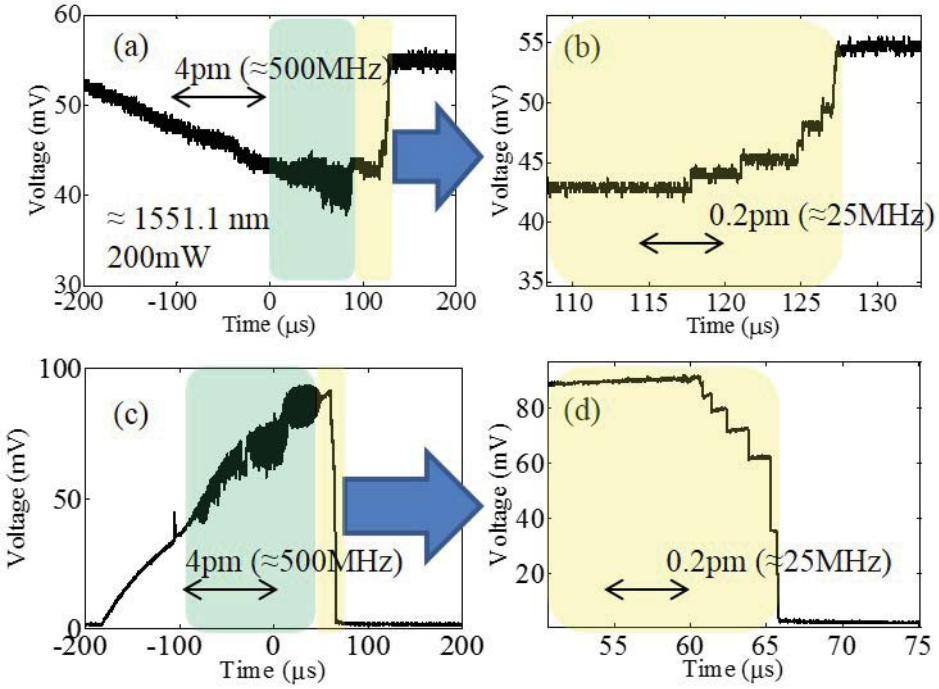

Fig. 5.6. (a) The transmission responses and (b) the corresponding responses by filtering out of the pump line with sweeping the laser around 1551.1 nm. (c)(d) The zoom-in area of the responses, showing multiple soliton steps.

To further identify the properties of the generated combs, time-domain studies are performed to address the temporal coherence and the cavity waveform. Unlike a short pulse generated in anomalous cavities, the measured cavity field has an complexly structured waveform. Figures 5.7 show the time-domain measurements at around 1549.3 nm with input power 200 mW. Again, a dispersion-compensated link is used to study the intracavity field and its corresponding spectral phase. The simulated and measured autocorrelation traces are shown before (5.7(b)) and after (5.7(d)) the low-noise transition. Before the phase-locking transition, the autocorrelation trace (Fig. 5.7(b)) has a contrast ratio ≈ 2, even after line-by-line compensation, showing a noise-like signal with poor coherence. After low-noise transition(Fig. 5.7(d)), the high compressibility implies the comb with good coherence. However, instead of observing a short pulse (or single soliton) for this high coherent comb, the measured intensity, calculated by the retrieved phase from the pulse shaper, forms an complexly structured waveform (green traces in Fig. 5.7(e)) similar to that observed in the previous chapter.

One question left is the reason for the phase-locking mechanism. Figure 5.8(a) shows the comb spectra after noise-free transition at different pump wavelengths. One significant feature is that the locally strong comb line keeps at approximately the same location ($\approx$ 1528 nm) with different pump wavelengths. This identification is similar to that observed in comb generation in normal dispersion cavity [71], which related to the mode-coupling between different mode families. In Fig. 5.8(b), different sections of the measured transmission spectrum are aligned by pinning one of the mode family close to zero offset in frequency. An avoided crossing between two different modes is obviously observed in the zoom-in spectrum (close to 1528 nm), evidencing the mode-coupling. This work suggests that the mode-coupling may be another strong effect on the phase-locking process in an anomalous dispersion cavity.

The observation of this step-like resonance and the noise transition in the transmission spectra helps us to identify the feasibility of coherent comb generation in anomalous dispersion, regardless of the shape of the intracavity field. Although the

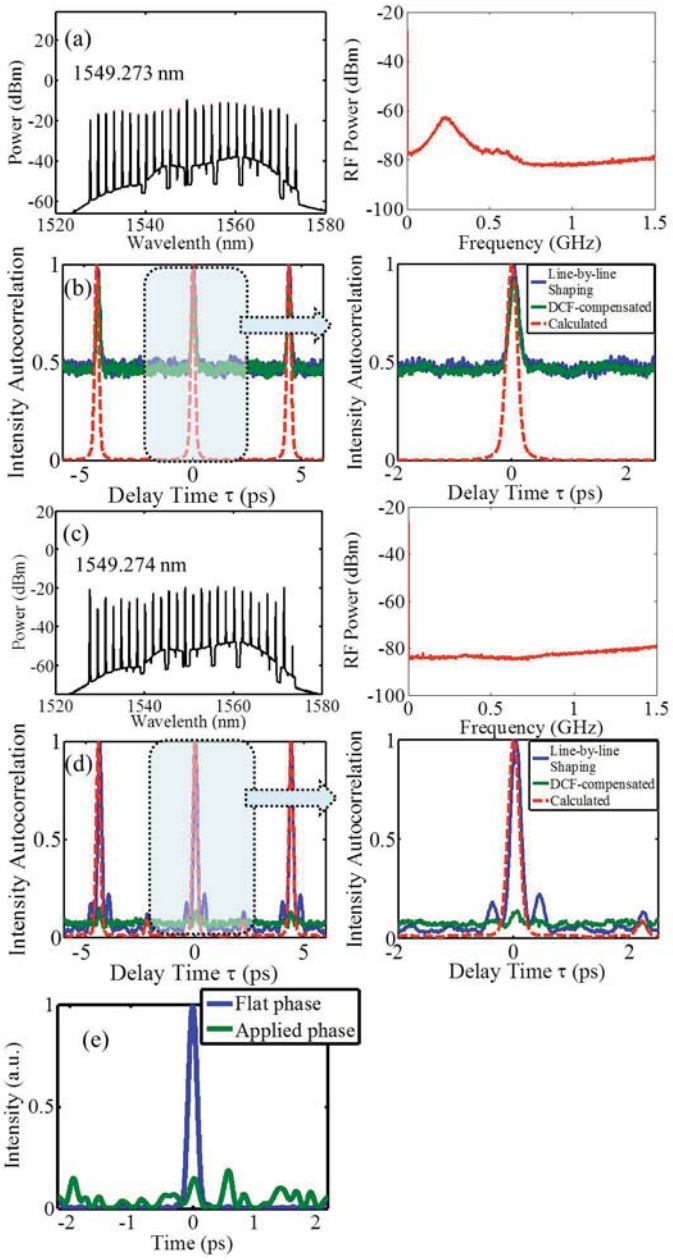

Fig. 5.7. Measured optical spectra (a) before and (c) after low-noise transition; the right figures of each optical spectrum show the corresponding intensity noise. The autocorrelation traces are shown in (b) and (d), respectively. (e) The simulated intensity with constant (blue curve) and retrieved phase (green curve).

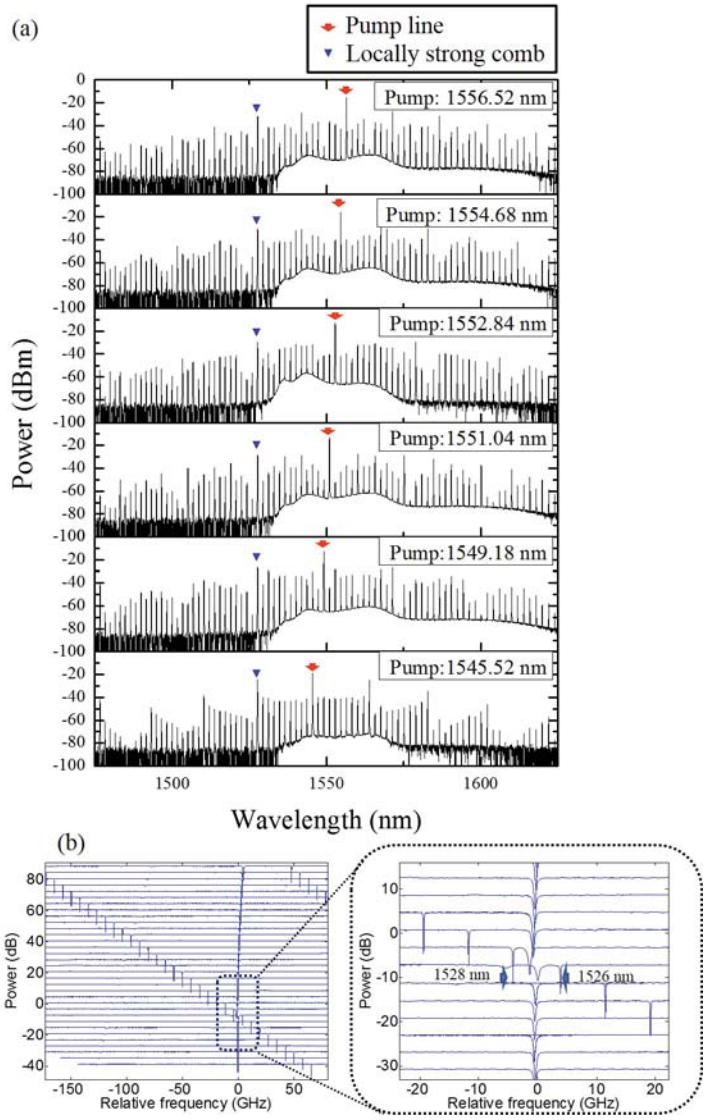

Fig. 5.8. (a) The comb spectra after noise-free transition at different pump wavelengths. (b) Aligned resonances centered at 1527 nm with fixed increment in frequency showing the mode-coupling.

locking mechanism in anomalous dispersion has not been well understood, these works suggest the existence of multiple nonlinear operating modes resulting in coherent comb generation.

5.2.2 Laser-Assisted Tuning of Micro-comb Generation

As discussed before, the noise feature is an important characteristic for Kerr comb formation; either noisy or coherent operating regimes are widely studied in different geometries of microresonators in anomalous dispersion regime [26,35,38,40,41,80,82]. Several techniques, like self-locking [41,80] and cavity soliton formation [35,38,40,82], are used to achieve low-noise transition by fine-tuning the pump laser. However, most experiments required careful laser detuning. The deterministic tuning process has not been well established. In this section, a tunable laser-assisted tuning process will be introduced to achieve low-noise comb spectra.

Figure 5.9(a) shows the experimental setup for laser-assisted tuning. The first tunable laser is amplified and sent into the microring for comb generation. The second laser is used to be a reference marker and define the terminating position for the sweeping of the first laser. As illustrated in the previous section, the transmission spectra are measured by filtering out of the pump line after the microring. A beating signal will be generated once the laser tuning is approximately around 10 MHz (in higher frequency) away from the reference laser, determined by the central wavelength of the band-pass filter (1 MHz bandwidth). A 30 MHz low-pass filter is then used to filter out unwanted frequency response above 150 MHz from the 10 MHz band-pass filter. This beating signal and the transmission spectra are then recorded by the oscilloscope simultaneously to locate the position of the reference laser. After selecting the proper position for the reference laser relative to the transmission spectrum, the comb is initiated by red-shifting the pump laser slowly into the cavity resonance, with a fixed pump power at the bus-waveguide. This comb generation process is the same with that used before for thermal locking. Figure 5.9(b) is the schematic diagram for

the laser-assisted tuning. Once the sweeping laser is close to the reference laser by 10 MHz, the control loop detects the beating signals with an electrical spectral analyzer; it stops the sweeping process, and then the comb spectrum is recorded.

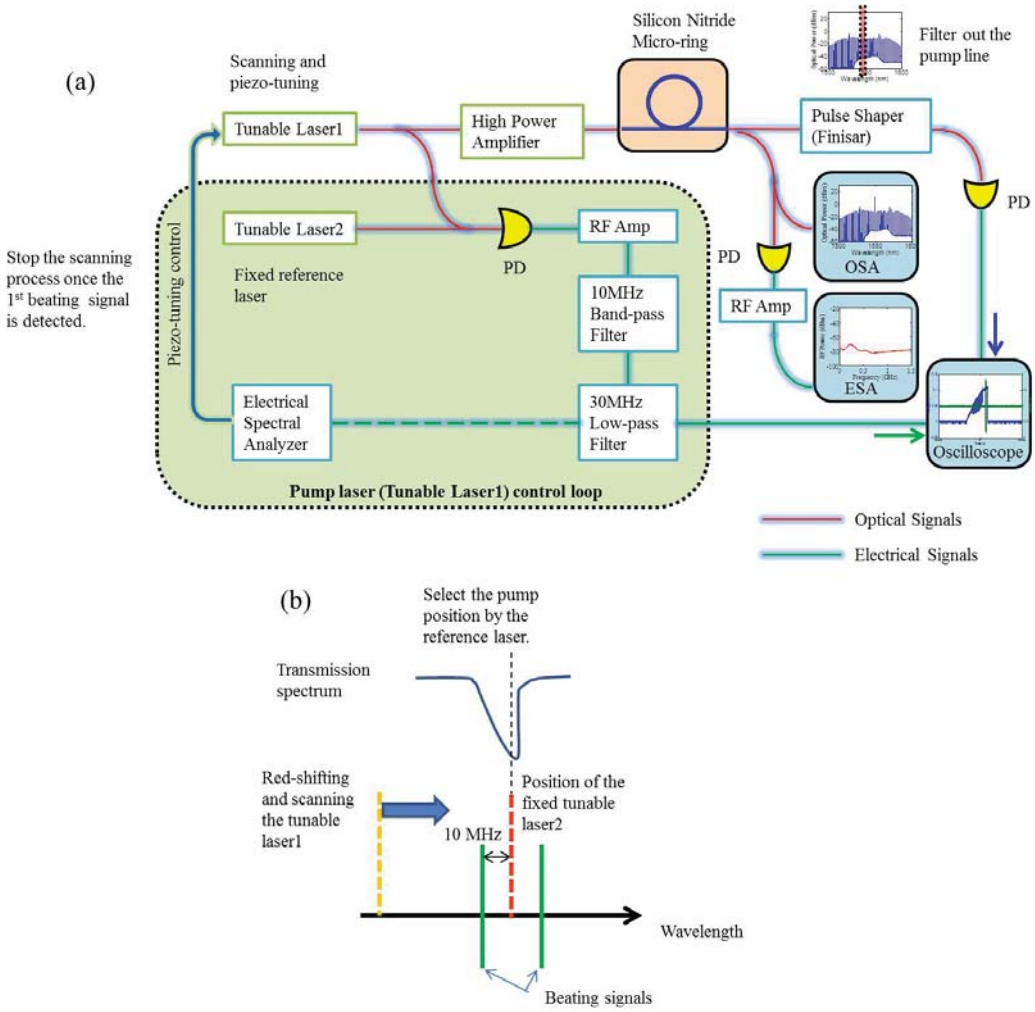

Fig. 5.9. (a) Experimental setup for laser-assisted tuning. The first tunable laser is amplified and sent into the microring for comb generation. The second laser is used to be a reference marker and define the terminating position for the sweeping process. (b) The schematic diagram for laser-assisted tuning. A beating signal will be generated once the laser tuning is approximately around 10 MHz away from the reference laser. The control loop stops the tuning process once the beating signal is detected by the electrical spectral analyzer.

Two examples of the transmission spectra and the reference beating markers are shown in Figs. 5.10(a)(b) with the reference laser centered around 1549.145 nm and 1549.144 nm, respectively, which correspond to the noise-free and chaotic regime of the converted signal (frequency combs). The wavelength of the reference laser is determined by a commercial wavemeter. The zoom-in spectra show a pair of beat notes spacing by 20 MHz. The first case shows that the terminating position for the sweeping laser is in the noise-free transition regime (as discussed in the previous section). The generated comb shows a noise-free spectrum similar to that observed in Fig. 5.5. For the second case, the marker is placed in the chaotic regime. Therefore, the generated comb shows large intensity noise while the sweeping is done. This demonstration provides a way to select the operating regime from the transmission spectra for comb generation. In addition, unlike the manually slow detuning for comb generation discussed in the previous section, the detuning speed here could be fast (10 to 40 nm/s) and the same with that used in sweeping the transmission spectra. This not only helps to link the comb generation to different regimes of high-power transmission spectra but also provides a more flexible path for low-noise comb formation.

5.3 On-chip Soliton Formation in Anomalous Dispersion Cavity

5.3.1 Modulation and Soliton Initiation Process

Previously, the pump laser is fine-tuned to the cavity resonance and, in order to achieve thermal locking, the laser is shifted from blue to red [18, 27, 60]. However, by manually fine-tuning the wavelength, the coupling condition, intracavity power, and temperature change simultaneously. The transient instability inhibits the stable soliton operation. To overcome this issue, an intensity modulator has been employed to modulate the pump power [78, 82]. This technique offers the possibility to operate generated comb in the soliton regime. Here, to characterize the soliton properties in silicon nitride microrings, the pump modulation is introduced to generate a single

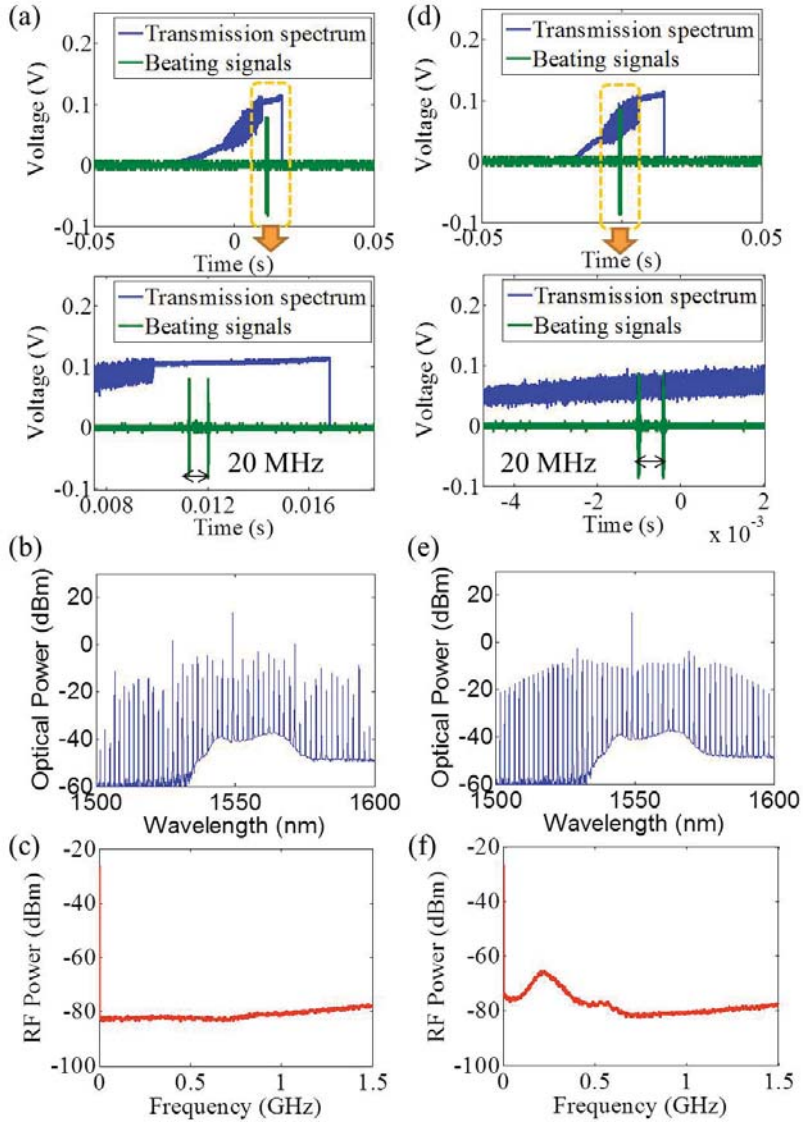

Fig. 5.10. The transmission spectra (blue traces) and its corresponding beating signals (green traces) with the reference laser centered around (a)1549.145 nm and (d) 1549.144 nm. (b)(e) The corresponding spectra of comb generation after terminating the laser tuning process. (c)(f) RF noise spectra of (b) and (e).

soliton. The schematic diagram is shown in Fig. 5.11. To achieve stable soliton operation, the pump power is patterned with a short dip around 200 ns time scale (as shown in Fig. 5.12). This power drop introduces perturbation in the cavity and induces the soliton formation. The pump power remains high and stable after the quick drop process; this power drop is patterned by a commercial arbitrary waveform generator (AWG) and keeps running with a repetition rate 1 Hz until the soliton is formed with low-noise transition. Afterward, the pump power remains the same throughout the measurements.

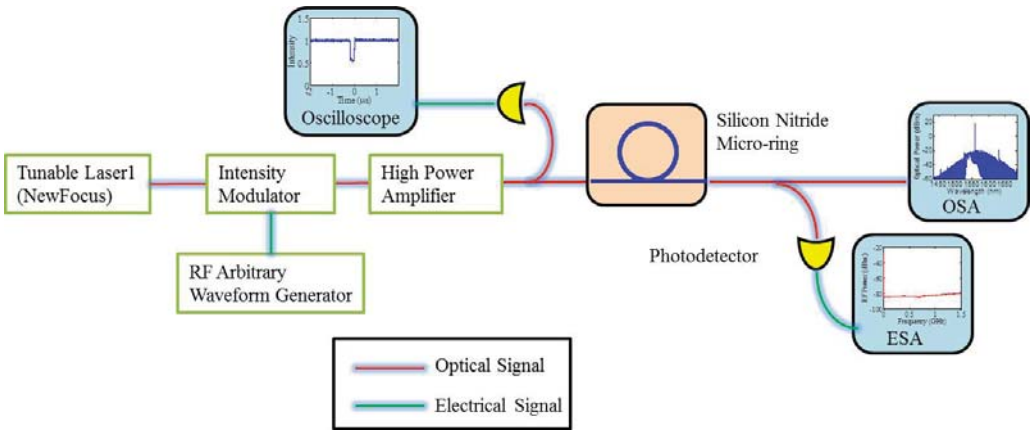

Fig. 5.11. The schematic diagram for soliton initiation process.

It should be noted here that the time scale of the drop ($\approx$ 200 ns) is relatively shorter than the thermal response time of the microresonator, typically in several tens μs range. Therefore, the power drop for soliton formation does not affect the cavity temperature. In addition, the drop period is also much shorter than the response time of the high power EDFA for the amplified pump power, therefore, the intensity modulator could be placed in front of the EDFA, which is operated in saturation regime. High extinction ratio ($\approx$ 17 dB) of the power drop could be achieved (as shown in Fig. 5.12) for the pump power measured before microrings.

Here, to generate cavity solitons, another silicon nitride waveguide resonator with waveguide dimension 2 μm (width) $\times$ 800 nm (height) and ring radius 100 μm is utilized for comb generation, corresponding to an average FSR $\approx$ 228 GHz. Figure 5.13

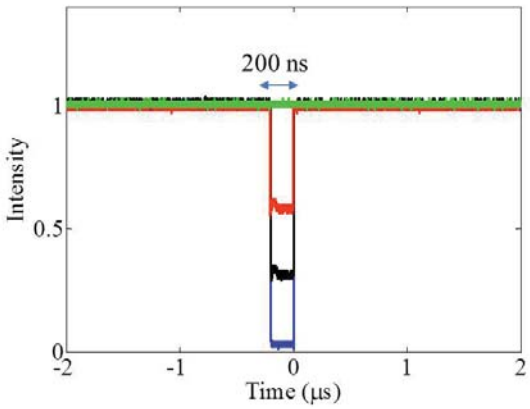

Fig. 5.12. Examples of modulated pump drop for soliton initiation; traces with different colors show different modulation depths. The green trace shows the optical intensity without modulating the pump power.

shows the microscope image of the microring. The ring resonator has anomalous dispersion of 48 ps/nm/km (β_2=-61 ps^2/km) measured by the frequency comb-assisted spectroscopy. Figure 5.14(a) shows the transmission spectrum of a resonance around 1560 nm while Fig. 5.14(b) shows the transmission spectrum by filtering out the pump line using a subsequent pulse shaper. The sweeping speed of the laser is set at 20 nm/s and the pump power for scanning is set at 500mW before the chip, which is later used for comb generation. Clear multiple steps can be observed in the zoom-in spectra from the oscilloscope, corresponding to the evolution of consecutive soliton numbers [35, 38, 40, 78, 82].

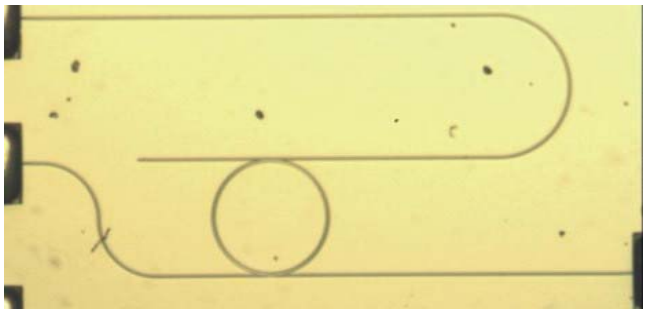

Fig. 5.13. The microscope image of the microresonator for soliton generation.

Figure 5.15 shows the exemplary comb generation before soliton initiation. By fine-tuning the pump wavelength, the comb spectrum first starts with multiple-FSR spacing (Fig. 5.15(a)) and finally yields a smooth spectrum with single FSR spacing (Fig. 5.15(b)). At this stage, a typical type II comb is observed with large intensity noise as shown in Fig. 5.15(d). To kick out the soliton, the pump wavelength is kept in the chaotic regime (e.g. 1560.46 nm in Fig. 5.15(b)) and also close to the dip of the thermally shifted resonance. The soliton initiation process is introduced by a short pump drop as described above. The drop has a period 200 ns and around 3 dB extinction ratio. Figure 5.16(a) shows the comb spectrum after soliton kicking. A smooth comb spectrum with hyperbolic secant ($sech^2(f)$) envelope is observed accompanying with a strong overlapping pump line, which is determined by both the intracavity field coupled from the microring and the pump directly transmitted from

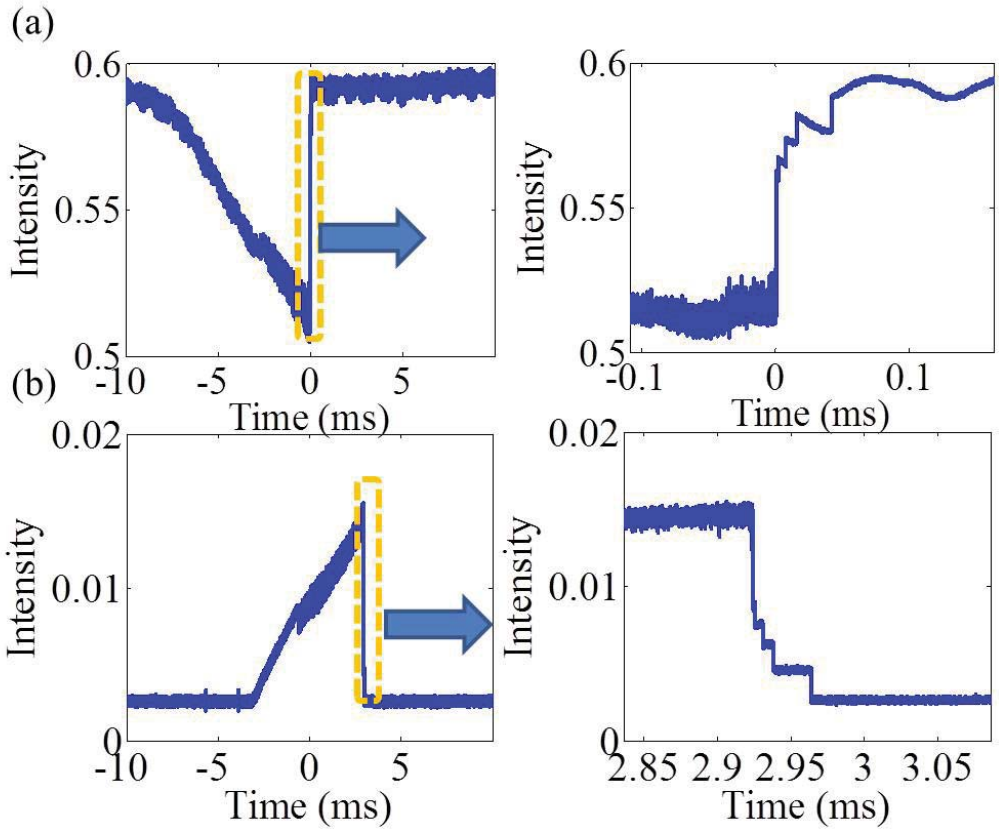

Fig. 5.14. The transmission spectra (a) with and (b) without the pump line. The room-in spectra with multiple soliton steps are shown in the right. The input pump is set at 500 mW before the chip and the scanning wavelength is around 1560 nm.

the bus-waveguide. The comb spectrum agrees well with the single soliton formation simulated in the previous section (Fig. 5.1). Figure 5.16(b) shows the corresponding RF intensity spectrum. Clearly, a noise-free spectrum close to the background noise of the ESA is observed, suggesting a low-noise comb. These spectral properties not only show the noise-free comb operation, but also imply the single soliton formation from this microring. Furthermore, the comb spectrum after soliton locking can remain for several hours without changing the spectrum and the noise features. It should also be noted that the soliton locking demonstrated here cannot be achieved by manually tuning the wavelength in the same device; this implies that a delicate process, such as a short pump drop [38] or pump detuning [90], is needed to initiate the soliton formation.

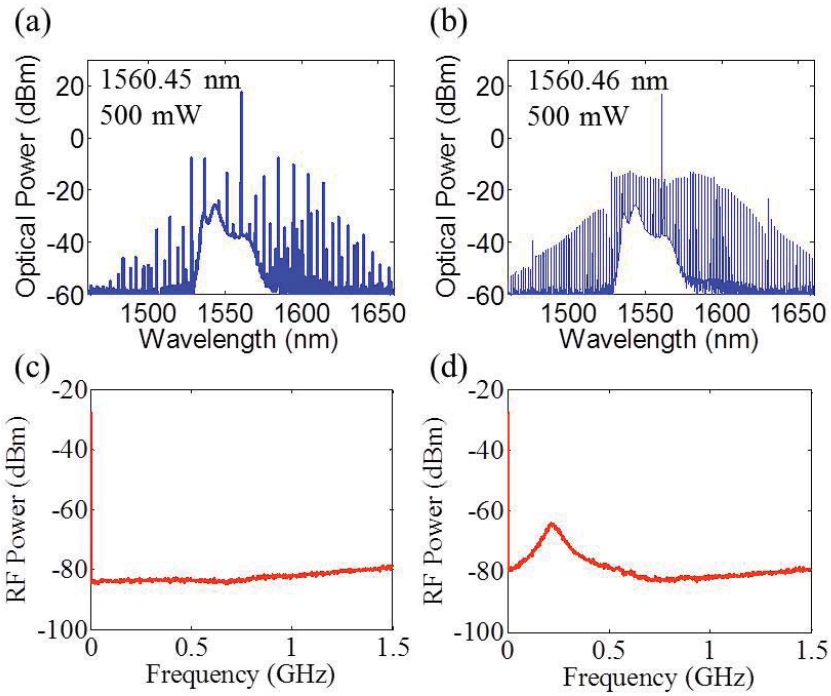

Fig. 5.15. Exemplary comb spectra pumped at (a)1560.45 nm and (b) 1560.46 nm, before soliton initiation process. (c)(d) The corresponding RF intensity noise.

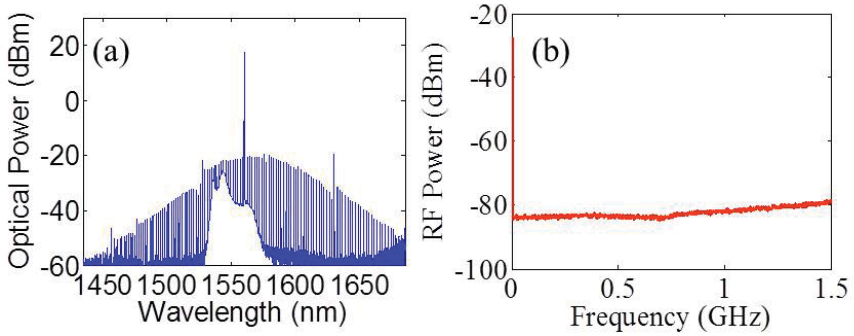

Fig. 5.16. (a) The optical spectrum and (b) the RF spectrum of the comb generation after soliton initiation. The pump wavelength is fixed around 1560.46.

Similar soliton locking transition could be observed in the same device by pumping at a different wavelength. Figure 5.17 shows the soliton transition around 1551 nm using the same initiation protocol. This work helps us to achieve stable soliton operation. By transitioning through the chaotic regime, a smooth, broad, and low-noise comb spectrum could be obtained. It also provides a way to mode-lock a type II comb in anomalous dispersion regime with larger spectral bandwidth compared to the combs in normal dispersion cavity.

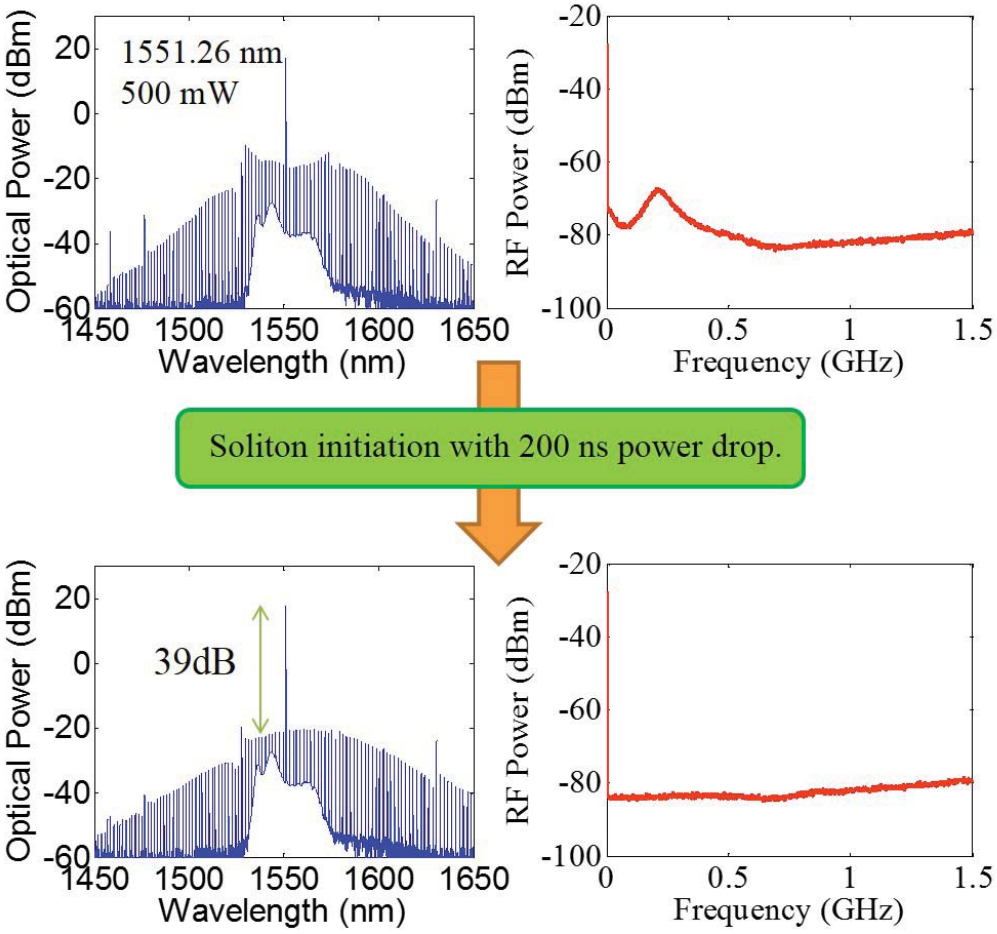

Fig. 5.17. The optical spectrum (left) and RF spectrum (right) of the comb generation before and after soliton initiation. The pump wavelength is fixed around 1551.26 nm

In addition to the power modulation, a recent study shows the possibility to generate soliton through proper pump detuning [90]. The soliton is induced by first forward tuning the laser from blue to red and then backward tuning the laser a few picometers to stabilize the soliton after transitioning from the chaotic state. This method has also been successfully applied in the same microring to achieve the stable single-soliton state.

5.3.2 Drop-port Response and Power Transfer of Soliton Spectra

In an anomalous dispersion cavity, soliton-locked frequency comb generation has been observed in both crystalline resonators [40] and on-chip resonators [78, 91]. Experimentally, a broad and smooth spectrum typically exhibits a single soliton per roundtrip time in the microresonator while, in some cases, periodic-shaped spectra are identified with multiple solitons per round trip in the cavity [78]. However, all of these works characterize the comb generation, time-domain waveform, and the corresponding spectrum based on a resonator bus-waveguide. A strong overlapping pump line and ASE noise are clearly observed in the spectrum similar to those measured in the previous section. As discussed in Chapter 3, the intracavity field in the cavity is not fully characterized due to the coupling at the bus-waveguide; in addition, since the ASE noise from the high power amplifier, it strongly degrades the optical signal-to-noise ratio (OSNR) of the output spectrum. The poor OSNR limits the further studies and applications.

To provide further information on microcavity solitons, drop-port measurements are performed, for which the strong overlapping pump is absent. The gaps between the ring resonator and the through-port and drop-port waveguides are 500 nm and 1000 nm, respectively. As mentioned in Chapter 3, this asymmetric coupling with weaker drop-port coupling minimizes the impact of the drop-port on the loaded quality (Q) factor. Figures 5.18 show the soliton spectra at the drop port with pump wavelengths 1551.26 nm and 1560.45 nm. These noise-free combs are initiated by modulating the

pump as mentioned above. Several significant points could be identified. First, unlike the previous drop-port study implementing a symmetric coupling [37], the detected drop-port spectrum of comb lines (e.g. pumping at 1551.26 nm, Fig. 5.18(a))has a similar envelope but ≈ 15 dB weaker power, compared with that at the through port. Second, since the amplified spontaneous emission (ASE) noise between the resonances is filtered out at the drop, the OSNR of the drop-port combs strongly increases in comparison with the through-port combs, especially around the ASE peak (≈ 1545 nm) from the amplified pump line. This helps to measure the time-domain data later at the drop port, even with the output comb power much lower than the through-port power. Third, the peak of the comb envelope is spectrally red-shifted from the pump due to the Raman induced soliton shift identified in Ref. [83, 84]. Last, as noted above, comparison of through-port and drop-port spectra shows that the intensity of the pump line is much closer to that of the adjacent comb lines at the drop port. For example, by pumping at 1551.26 nm (Fig. 5.18(a)), the pump power measured at the through port is around 43 dB higher than that at the drop port; while the power difference between the pump line and adjacent comb lines reduces from 39 dB at the through port to less than 11 dB at the drop port. This suggests that under soliton operation, most of the strong pump power in the through port is the result of the pump being transmitted directly through the bus-waveguide without coupling into the microring.

Figure 5.19(a) shows the soliton spectra measured at 1551.26 nm, both at through and drop ports. To understand the large difference of the comb power between the through and drop port, the coupling parameters are extracted by fitting the low-power transmission spectra (both the through- and drop-port spectra shown in Figure 5.19(b)), as explained in Sec. 3.2. The through-port and drop-port coupling are $\kappa_e^2 = 4.6\times10^{-4}$ and $\kappa_d^2 = 1.6\times10^{-5}$, respectively, giving the power difference around 14.6 dB at resonance. This is in good agreement with the experimental data (≈ 15 dB) in the coupled comb power. In addition, the intrinsic loss per round trip is $\kappa_p^2 = 1.7 \times 10^{-3}$ suggesting under-coupled condition. To further provide the inforamtion of intracavity

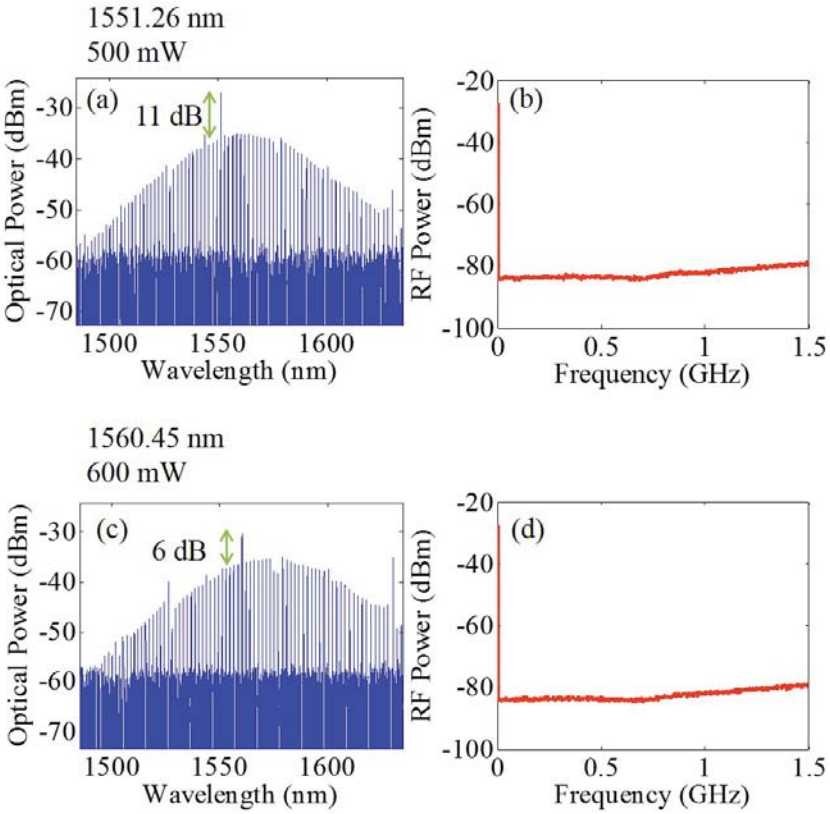

Fig. 5.18. The soliton spectra at the drop port with pump wavelength (a) 1551.26 nm and (c) 1560.45 nm. The corresponding intensity noise is shown in (b) and (d).

powers, Table. 5.2 shows the measured optical powers in the waveguide as well as the corresponding intracavity power for both chaotic and single-soliton state.

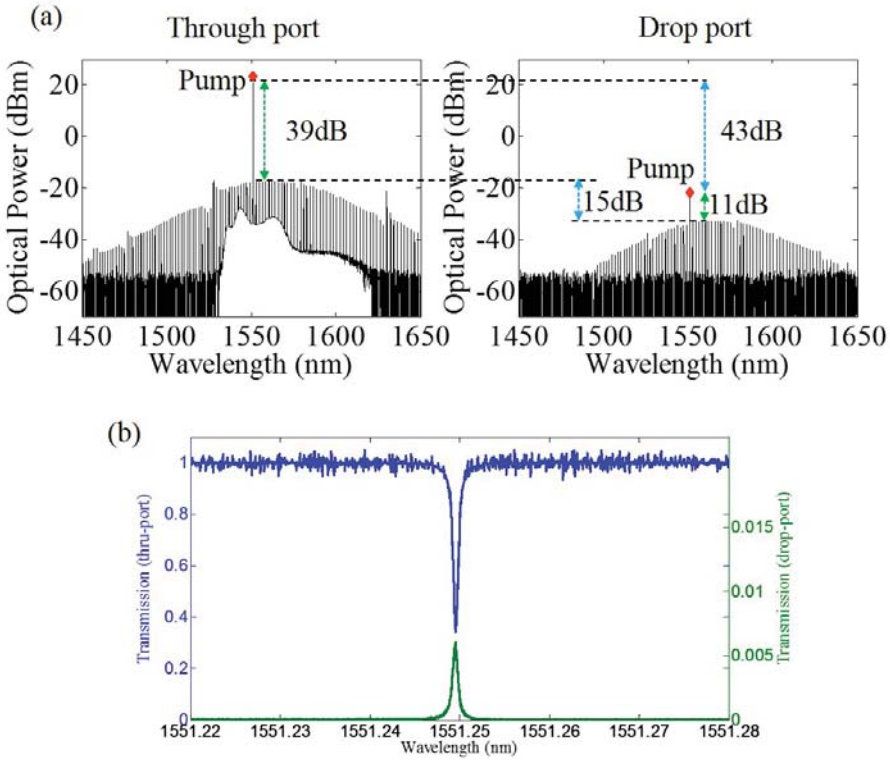

Fig. 5.19. (a) The soliton spectra measured at through and drop ports . (b) The low-power transmission spectra at through (blue trace) and drop (green trace) ports.

By total comb power it means the power integrated over all of comb lines except for the pump line; while the intracavity powers are estimated by dividing the power at drop-port spectrum with the drop-port coupling (κ_d^2). The powers in the waveguides are estimated by using the optical spectra and assuming half of the fiber-to-fiber loss ($\approx$ 6 dB) to both the output and input facets. Clearly, the measured data show low efficiency for comb generation (only 0.5% of the input power transfers to the total comb power at the through and drop port). This can be explained by the observation of the relative low transmission dip (around 0.1 dB) and high transmission at the through-port pump line (244 mW out of 250 mW input power at bus) in the presence

Table 5.2
Pump and comb power at the waveguides and in the microring

Power in the input fiber	loss per facet
500.0 mW	≈ 3dB

Power in the waveguide (chaotic regime)	Pump power	Total comb power
Input port	250.0 mW	
Drop port	124.4 μW	107.8 μW
Through port	206.0 mW	5.9 mW
Cavity power estimated by drop port	7.9 W	6.6 W

Power in the waveguide (soliton regime)	Pump power	Total comb power
Input port	250.0 mW	
Drop port	10.8 μW	30.6 μW
Through port	244.3 mW	1.1 mW
Cavity power estimated by drop port	675.0 mW	1.9 W

of the comb generation - only a small portion of pump power ($\approx$ 6 mW) is coupled into the microring. It emphasizes the idea that identified in the previous chapter, for an initially under-coupled device, the presence of comb generation pushes the microring into severely under-coupled regime and reduces the pump enhancement in the cavity. Meanwhile, the total power loss per round trip inside the cavity is roughly estimated by multiplying the total build-up power ($\approx$ 2.6 W, including both the pump and comb power) with the intrinsic loss (1.7×10^{-3}) which gives a value around 5 mW. This agrees well with the quantification of the observed coupled power; 6 mW coupled pump from the bus-waveguide to the microring results in 1 mW output combs and 5 mW power loss. Due to the large pump power passing through the through port, the overall efficiency of the generated comb is low ($\approx$ 0.5%). However, the intracavity field shows efficient ($\approx$ 75%) power transfer from the pump to the comb in the single soliton regime. Note that the observed efficiency in the chaotic regime is merely $\approx$ 46%, this suggests that, at least for the case here, a single-soliton comb could provide higher power conversion than that in the chaotic regime. Another example, pumping at 1560.45 nm (Fig. 5.18(c)), shows even higher power conversion of the intracavity field up to 85%. Furthermore, by transitioning from the chaotic to the single soliton regime, the pump at the drop port drops more than ten times, whereas the comb drops by only around three times. It results in quite different power balance.

5.3.3 Pump Detuning for Cavity Soliton

The generation of cavity solitons in microresonators is an intriguing feature of microcomb generation. Previously, several studies have focused on investigating solitons with Lugiato-Lefever model [85]. In simulation, the pump detuning is an important parameter to determine the process of soliton evolution [38,88,92,93], either the number of solitons or the transition dynamics between chaotic and stable soliton states. Experimentally, the sign of the pump detuning in soliton formation has been identified in Ref. [38, 82] using Pound-Drever-Hall (PDH) signal [94], while the pump detuning

is also quantitatively identified through a pump-reconstruction process in normal dispersion regime for dark pulses [66]. A previous study estimates the detuning through the dispersion and the pulse width calculated by the optical spectrum [82], and recently a way to measure the effective detuning is introduced by using the modulation response with a vector network analyzer [90]. To further unveil this issue, here the pump detuning for the single soliton operation is estimated by using the effective loss in the presense of comb generation. In addition, the large power difference of the pump line between the through- and drop-port spectra could be explained to a large extent.

To characterize the pump detuning, the direction of detuning is first determined by a PDH measurement. The sign of PDH sign indicates the regime where the pump is effectively blue- or red-detuned. With high pump power (the same used in the soliton formation), the transmission spectrum (blue curve) and its corresponding PDH signal (green curve) are shown in Fig. 5.20. Clearly, stable soliton steps are identified in the effectively red-detuned regime, in agreement with the previous demonstrations [38,82]. The transition from noise to stable soliton steps overlaps the zero crossing point of the PDH signal.

As mentioned in the previous chapter, the comb generation results in addition consumption of the pump power in the cavity. In the presence of comb generation, the effective intrinsic loss at pump ($\kappa^2_{p\_eff}$) could be expressed as:

$$\kappa_p^2 + \frac{P_{comb}}{P_{pump}} \times (\kappa_p^2 + \kappa_e^2 + \kappa_d^2) = \kappa^2_{p\_eff} = 8 \times 10^{-3} \tag{5.2}$$

$$\kappa_{p\_eff} \approx 0.089$$

where κ coefficients are defined as those in Chapter 3. $\frac{P_{comb}}{P_{pump}}$ is the ratio between the total comb power excluding pump and the pump power inside the cavity. Here, this ratio can be simply determined by the drop-port data.

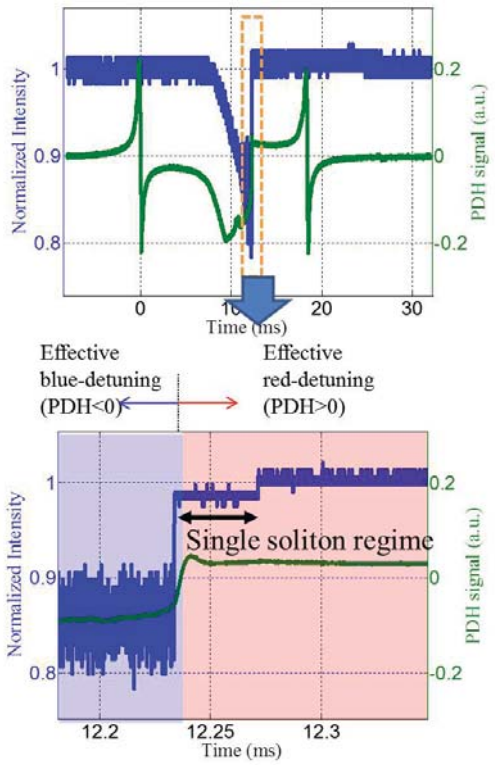

Fig. 5.20. High-power transmission spectrum and its corresponding PDH signal.

.

With comb generation, the transmission response at the through port is expressed as:

$$T_{thru} = \frac{(\omega - \omega_0)^2 + (\frac{FSR_f}{2})^2(\kappa_{p\_eff}^2 + \kappa_d^2 - \kappa_e^2)^2}{(\omega - \omega_0)^2 + (\frac{FSR_f}{2})^2(\kappa_{p\_eff}^2 + \kappa_d^2 + \kappa_e^2)^2} \tag{5.3}$$

where κ_e and κ_d are the waveguide couplings determined by the transmission spectrum in the cold cavity, FSR_f is the free spectral range in frequency, and $(\omega - \omega_0)$ is the effective frequency detuning for comb generation.

This power response can be determined experimentally by comparing the pump line (as forming soliton) at output guide to that at the input guide, which gives a value roughly around -0.1 dB based on Table 5.2. As demonstrated above, the pump frequency is red-detuned with respective to the thermally shifted resonance to achieve single soliton formation. Therefore, the effective frequency detuning is numerically solved $\omega - \omega_0 \approx$ -435 MHz (in red-detuned) while forming the single cavity soliton. It is noteworthy that the effective pump detuning is different from the one used in Lugiato-Lefever model [38, 82], which represents the phase detuning between the pump frequency and the cold-state resonance. Here, the effective pump detuning represents the detuning between the pump frequency and the effectively shifted cavity resonance [66, 90]. With the retrieved pump detuning, the corresponding through-port/drop-port response at pump line is given by:

$$\frac{T_{thru}}{T_{drop}} = \frac{(\omega - \omega_0)^2 + (\frac{FSR_f}{2})^2(\kappa_{p\_eff}^2 + \kappa_d^2 - \kappa_e^2)^2}{(\frac{FSR_f}{2})^2(4\kappa_d^2\kappa_e^2)} = 43.3dB \tag{5.4}$$

which is in good agreement with that observed in Fig. 5.19(a). This well explains the large power difference at the pump frequency in the presence of soliton formation. The strong pump line at through port is therefore explained by several factors: (1) the input bus is under-coupled; (2) power transfer into combs aggravates the under-coupling condition [37]; (3) soliton formation is accompanied by strong red-detuning from the thermally-shifted resonance [38, 82]. This also explains the decrease in resonance dip at through port from around 4 dB (in the cold cavity) to 0.1 dB (in the single soliton regime).

To conclude, the drop-port geometry provides a guideline to identify the power transfer and the spectral properties in the single soliton regime. With directly probing the intracavity spectrum, a way to estimate the effective pump detuning in single soliton regime is introduced. In addition, the relatively smooth spectrum exhibited at the drop port aids in further investigating the time-domain waveform of the generated comb in the following section.

5.4 Time-domain Characterization of a Cavity Soliton

Temporal solitons can emerge in a wide range of nonlinear systems, such as optical fibers and microcavities; and it has also been applied in a variety of fields in optics, medicine, and biology [95]. Theoretically, these solitons are solutions to the Lugiato-Lefever equation [85] as mentioned in the earlier section. The generated spectrum of the cavity soliton may give hints to the number of soliton per round trip inside the microcavity [78]. However, without knowing the spectral phase, smooth spectra (as shown in Fig. 5.16 and Fig. 5.17) do not guarantee the existence of a single soliton. To identify the soliton formation and reveal the time-domain waveform inside the cavity for the case above, a SHG intensity autocorrelator based on a noncollinear, background-free geometry is employed. Figure 5.21 shows the experimental system for time-domain characterization. At the drop port, the ASE noise from the pump line is filtered out between the resonances before the first EDFA. To compensate the system dispersion between the microring and the intensity autocorrelator, a short test pulse ($\approx$ 148 fs FWHM of intensity autocorrelation) is first used as an input source before the system. The system dispersion is minimized by programming a line-by-line pulse shaper with optimized second- and third-order dispersion [77]. The intensity autocorrelation of the test pulse after the entire system is around 256 fs FWHM of intensity autocorrelation (AC) which is close to the simulated bandwidth-limited FWHM (225 fs), calculated by the measured optical spectrum before the autocorrelator (assuming constant spectral phase). The compensated link is well

enough for measuring pulse durations down a few hundred femtoseconds. The further pulse broadening after the entire system results from the limited bandwidth of the EDFAs.

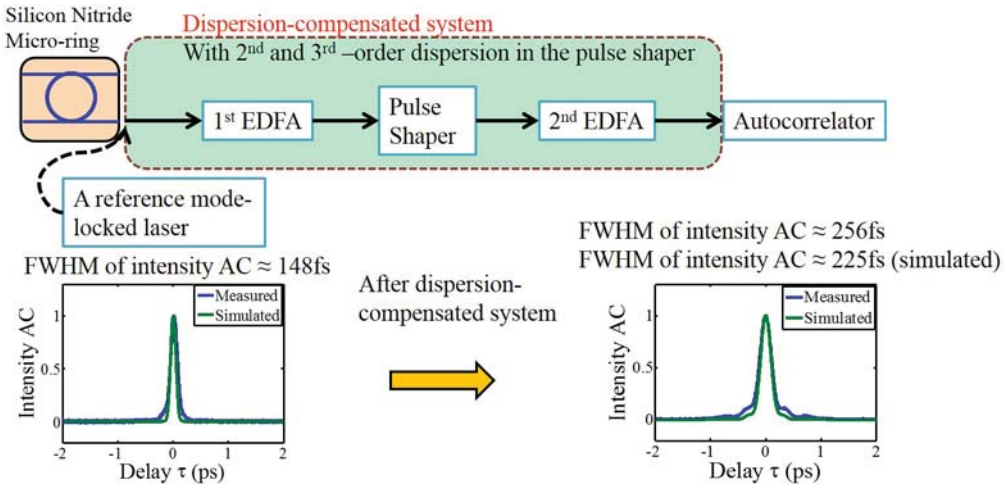

Fig. 5.21. The dispersion-compensated system for the time-domain measurement. A reference laser with FWHM of intensity intensity autocorrelation ≈ 148 fs is used as a test pulse.

For the comb generation in Fig. 5.18(a), the pump and comb lines emerging from the drop port in the range 1535-1575 nm are boosted via EDFAs, but otherwise the spectrum is not modified as shown in Fig. 5.22(a). The clipped spectrum outside of 1527-1568 nm range is due to passband of pulse shaper and we also deliberately attenuate the combs in the range 1527-1535 nm with strongly unequal EDFA response. The ASE noise (after the first EDFA) between the combs is filtered out by the pulse shaper in order to further increase the OSNR. Figure 5.22(b) shows the corresponding measured (blue line) and simulated (green line, assuming constant spectral phase) autocorrelation traces. The measured trace with a FWHM around 327 fs is in close agreement with the calculated trace, suggesting a pulse close to the bandwidth-limit. This time-domain waveform is similar to the single soliton generation previously observed in both crystalline microresonators [38, 40] and photonics chip-based microresonators [35, 82]. However, unlike characterization in a through-

port geometry, there is no need to attenuate the much stronger pump line (≈ 40 dB) at the through-port spectrum for time-domain characterization.

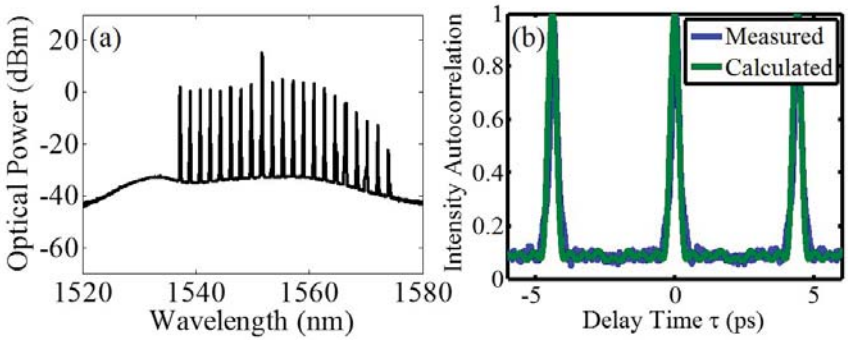

Fig. 5.22. (a) Optical spectrum at the drop port after the dispersion-compensated system. (b) The corresponding measured (blue trace) and calculated (green trace) intensity autocorrelation traces.

Another interesting question left here is the phase relation between the pump line and the generated combs. Theoretically, the phase of the pump line can exhibit an offset in soliton-mode-locked parametric frequency combs [96]. Experimentally, in Ref. [66], the intracavity pump phase and amplitude are reconstructed through a complicated process in a normal dispersion cavity, the reconstructed pump phase shows a significant offset to the phase of the adjacent combs, and the time-domain waveform exhibits a dark pulse. However, few of the previous studies addressed this issue in the single soliton regime, and the information for intracavity field is limited. Here, the drop-port spectrum aids in studying the time-domain waveform in the microring and provides information of the spectral phase and CW background in single soliton formation.

Figure 5.23 shows the optical spectrum and the measured autocorrelation trace by applying π phase shift to the pump line. The peak intensity of the autocorrelation is strongly decreased with increasing CW background, implying the pump phase is significantly out of the comb lines after adding the phase shift. This demonstration not only suggests a coherent comb generation but also reveals that the spectral phase

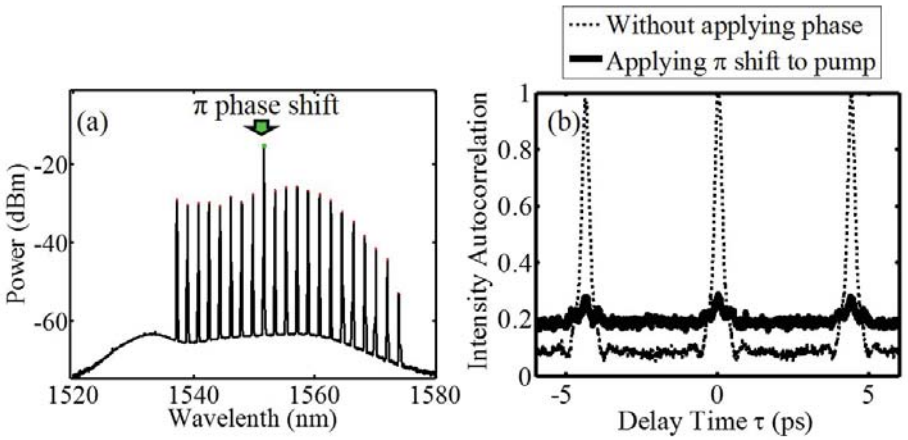

Fig. 5.23. (a) Measured optical spectrum before the autocorrelator (π phase shift is applied at the pump line using a pulse shaper). (b) The measured intensity autocorrelation trace with a π shift at pump. The dashed line shows the measured trace without applying phase to the pump line.

of the pump line is close to that of the generated combs. The dashed line shows the reference measured trace without applying phase to the pump line. Clearly, even with pump line 10 dB higher than the strongest comb line in the spectrum, the mode-locked comb exhibits a much strong peak intensity in autocorrelation, evidencing a bright pulse inside the cavity.

To further address this issue, the visibility curves $V(\delta\phi)$ are studied, defined as [26, 42]:

$$V(\delta\phi) = |\frac{V_0 - V_1}{V_0 + V_1}| \tag{5.5}$$

where V_0 and V_1 are the value of the intensity autocorrelation peak and the value half way between the peaks. $\delta\phi$ is the applied pump phase using the pulse shaper. Figure 5.24(a) shows the measured autocorrelation traces with different applied pump phases while Figure 5.24(b) shows the measured (green and blue dots) and calculated (red trace) visibility data with different pump phases. The pump phase in the visibility data is the complement of the phase applied by the shaper. The simulated visibility is plotted based on the optical spectrum in Fig. 5.23(a), assuming flat spectral phase. Clearly, the measured visibility is close to the simulated curve but with a shift $\approx$ 0.42 rad. This verification suggests that the pump line phase after forming soliton is nearly but not perfectly in phase with the comb, with a discernible phase shift $\approx$ 0.42 rad. Similar results showing small and discernible phase offset at pump are also identified for the case in Fig. 5.18(c). For the experimental measurements the phase is defined in the convention prevalent in ultrafast optics [49], in which $e(t) = Re[a(t)e^{j\omega t}]$ and the complex envelope function in spectrum $A(\omega) = |A(\omega)|e^{\phi(\omega)}$ is related to $1/2\pi \int A(\omega)e^{j\omega t}$. So if comparing the spectral phase $\phi(\omega)$ and the spectral phase offset θ at the pump relative to the mean phase of combs in experiments to that from the standard Lugiato-Lefever equation [86, 96], where $e(t) = Re[a(t)e^{-j\omega t}]$, the measured positive phase offset is equivalent to a negative one from Lugiato-Lefever equation. The phase offset can be attributed to the phase-matching [97] or self-organization in Kerr comb generation [96]. Note here unlike the phase obtained at

through-port data [98], these experiments, for the first time, identify the pump phase offset inside the microring in the single soliton regime.

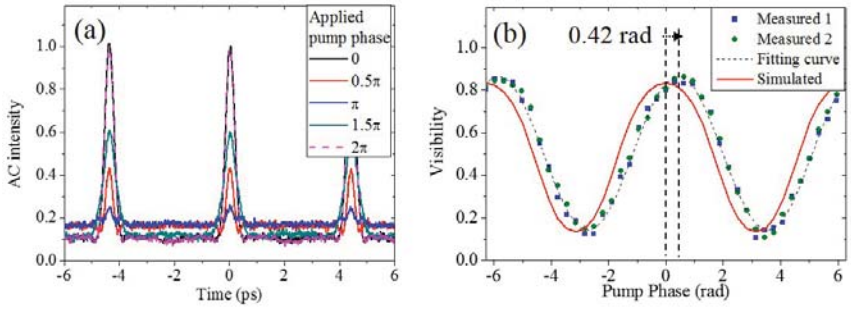

Fig. 5.24. (a) The measured autocorrelation traces with different pump phases applied in the shaper. (b) Simulated (red trace) and measured (green and blue dots) visibility of the autocorrelation traces of the comb in Fig. 5.23(a). The fitting curve of the measured data is shown with a dashed line.

Based on the mode-locked behavior and the retrieved pump phase in the cavity, the intensity profile of the generated soliton pulse inside the cavity can be reconstructed by the measured optical spectrum at the drop port (Fig. 5.25(a)). A bright pulse with a low CW background is evaluated with a pulse width $\approx$ 74 fs, as shown in Fig. 5.25(b). The CW background intensity (blue line), calculated from the intracavity pump alone, is only 0.5% compared with the peak intensity of the pulse. In contrast to the through-port data, this demonstration relays genuine information for single cavity soliton and provides a compelling evidence for the existence of on-chip single soliton operation.

The drop-port spectrum and time-domain studies demonstrated here provide several significant features. First, it increases the OSNR of the comb spectrum. Second, the spectral phase of the pump line is first time identified in the single soliton regime, which is $\approx$ 0.42 rad offset from that of the generated combs. Last, as illustrated before, the pump line is merely around 10 dB higher than the adjacent comb lines, suggesting a much smoother spectrum compared with those measured at the through

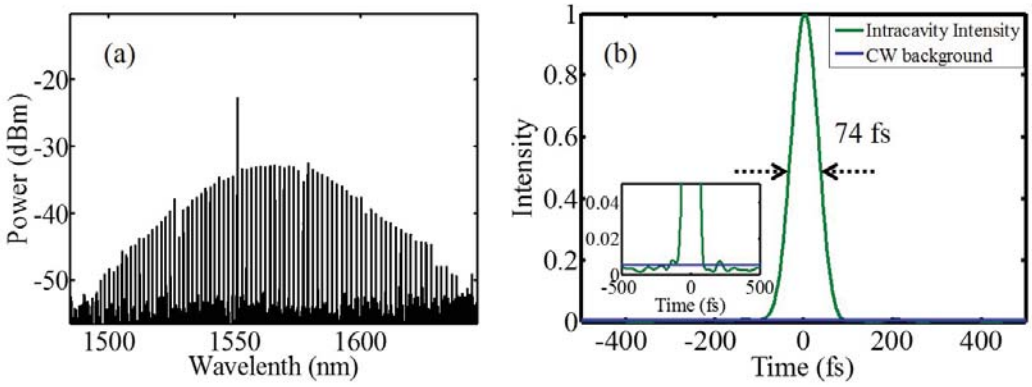

Fig. 5.25. (a) The measured single soliton spectrum at the drop port. (b) The intensity profile of the generated soliton pulse estimated by the measured optical spectrum and the retrieved pump phase.

port [35,38,40,82]. The intracavity field and CW background can be identified at the microresonator drop port, for which the strong overlapping pump is absent.

In conclusion, by transitioning a chaotic comb to a phase-locked comb, the coherent comb generation in anomalous dispersion regime is an essential milestone toward a fully integrated, broadband on-chip comb source. The soliton-locked mechanism could be initiated through pump modulation. Unlike the coherent comb generation in normal dispersion cavities, the on-chip soliton in microresonators potentially provides a path to yield octave comb spectra for broadband applications, such as self-reference, broadband sensing, and optical synthesizers [82]. In comparison with the soliton formation demonstrated at the through-port experiments with a very strong overlapping pump field, here further information about the comb spectrum, power transfer, and time-domain waveform directly in the cavity are provided. The cavity spectrum can be distinguished with pump and comb power in certain. The intracavity field shows efficient ($\approx 75\%$) power transfer from the pump to the comb. A way to estimate the pump detuning for soliton formation is discussed by considering the effective loss after comb generation. In the end, by probing the waveform directly at the drop port, the spectral phase of the pump line is measured nearly but not perfectly in phase with the comb, with a discernible phase shift of order ≈ 0.4 rad, suggesting a pulse close to transform-limited. A bright, short pulse with a FWHM ≈ 74 fs is estimated in the cavity with a weak CW background.

6. CONCLUSIONS

On-chip high Q resonators open a new field of optical frequency comb techniques. By carefully pumping the cavity resonance, intracavity pump power produces comb lines equally spaced in frequency through nonlinear FWM process. Due to its high repetition rate, low-cost, compact design, and simplicity, micro-combs have been widely studied in different materials, such as microdisks, microtoroids, whispering gallery mode resonators, and waveguide resonators. Silicon nitride waveguide resonators are a promising material and geometry for the next generation of microresonator-based frequency combs. The high nonlinearity of silicon nitride, low material absorption in C-band, and CMOS-compatible fabrication attract researchers' attention and may facilitate the comb technology transfer from lab-level studies to industrial applications, especially in high-speed optical communication and integrated photonics. For comb generation in microresonators, type I and type II combs have totally different spectral properties. For a type I comb, where the initial pair of sidebands is spaced by exactly single FSR from the pump line, it has high fidelity in communication performance, low intensity noise, and high temporal coherence; while for a type II comb, where the initial pair of sidebands emerged several FSRs away from the pump and additional lines later filled in, it exhibits poor communication performance, high intensity noise, and low temporal coherence. This identification between routes to comb formation, communication performance, intensity noise, and temporal coherence provides us a way for future designs and micro-comb operation.

In addition, the cavity dispersion and group velocity play an important role to determine the comb generation process. Unlike the modulational instability in anomalous dispersion cavity, frequency comb in a normal dispersion cavity could be initiated through the mode-coupling (avoided mode crossing) between two different mode families. It also exhibits totally different time-domain waveforms in the microcavity. A

dark or bright mode-locked, short pulse could be possibly identified in the normal dispersion with low intensity noise while, in anomalous regime, a mode-locked comb is obtained through transitioning from chaotic regime to soliton formation. A bright, short pulse is clearly identified with a smooth optical spectrum.

To further investigate the properties of microresonator-based combs, the power coupling, comb efficiency, and generation threshold are discussed with the aid of a drop-port geometry. Since the comb generation itself transfers additional power from the pump line in the microcavity, a nonlinear coupling effect is identified both at the drop- and through-port response. In the presence of comb generation, the comb efficiency could be optimized through carefully designing the coupling into over-coupled regime. Furthermore, a drop-port waveguide provides a way to increase signal-to-noise ratio in the output spectrum by filtering out the ASE noise between the adjacent resonances. It also provides purer information of the intracavity waveform by avoiding the strong overlapping pump line at the bus-waveguide. By updating the system with a dispersion-compensated link, the mechanism for comb generation in the cavity could be clearly identified through time-domain studies.

On the other hand, several measurements have been introduced to investigate the microresonator-based combs. A frequency comb-assisted spectrum is used to measure the cavity dispersion through precisely calibrating the FSR variation of individual cavity resonances. The coupling condition between bus-waveguide and microring is distinguished through RF-modulated sidebands and a vector network analyzer. To generate frequency combs with low-noise transition, a laser assisted tuning is used to define the terminating point relative to the noise free regime at the transmission spectrum. By detecting the beating signal from the electrical spectral analyzer, the noise-free combs after transition could be achieved through automatic laser detuning. In the end, a patterned, modulated pump line with a drop period 200 ns is used to initiate the soliton process.

LIST OF REFERENCES

LIST OF REFERENCES

[1] M. J. Thorpe, K. D. Moll, R. J. Jones, B. Safdi, and J. Ye, "Broadband cavity ringdown spectroscopy for sensitive and rapid molecular detection," *Science*, vol. 311, no. 5767, pp. 1595–1599, 2006.

[2] S. A. Diddams, L. Hollberg, and V. Mbele, "Molecular fingerprinting with the resolved modes of a femtosecond laser frequency comb," *Nature*, vol. 445, no. 7128, pp. 627–630, 2007.

[3] A. Schliesser, M. Brehm, F. Keilmann, and D. van der Weide, "Frequency-comb infrared spectrometer for rapid, remote chemical sensing," *Opt. Express*, vol. 13, pp. 9029–9038, Oct 2005.

[4] T. Udem, R. Holzwarth, and T. W. Hänsch, "Optical frequency metrology," *Nature*, vol. 416, no. 6877, pp. 233–237, 2002.

[5] S. A. Diddams, D. J. Jones, J. Ye, S. T. Cundiff, J. L. Hall, J. K. Ranka, R. S. Windeler, R. Holzwarth, T. Udem, and T. W. Hänsch, "Direct link between microwave and optical frequencies with a 300 Thz femtosecond laser comb," *Phys. Rev. Lett.*, vol. 84, pp. 5102–5105, May 2000.

[6] J. Reichert, M. Niering, R. Holzwarth, M. Weitz, T. Udem, and T. W. Hänsch, "Phase coherent vacuum-ultraviolet to radio frequency comparison with a mode-locked laser," *Phys. Rev. Lett.*, vol. 84, pp. 3232–3235, Apr 2000.

[7] I. Coddington, W. C. Swann, and N. R. Newbury, "Coherent multiheterodyne spectroscopy using stabilized optical frequency combs," *Phys. Rev. Lett.*, vol. 100, p. 013902, Jan 2008.

[8] C.-B. Huang, Z. Jiang, D. Leaird, and A. Weiner, "High-rate femtosecond pulse generation via line-by-line processing of phase-modulated CW laser frequency comb," *Electronics Letters*, vol. 42, pp. 1114–1115, September 2006.

[9] D. J. Jones, S. A. Diddams, J. K. Ranka, A. Stentz, R. S. Windeler, J. L. Hall, and S. T. Cundiff, "Carrier-envelope phase control of femtosecond mode-locked lasers and direct optical frequency synthesis," *Science*, vol. 288, no. 5466, pp. 635–639, 2000.

[10] R. Wu, V. R. Supradeepa, C. M. Long, D. E. Leaird, and A. M. Weiner, "Generation of very flat optical frequency combs from continuous-wave lasers using cascaded intensity and phase modulators driven by tailored radio frequency waveforms," *Opt. Lett.*, vol. 35, pp. 3234–3236, Oct 2010.

[11] H. Murata, A. Morimoto, T. Kobayashi, and S. Yamamoto, "Optical pulse generation by electrooptic-modulation method and its application to integrated ultrashort pulse generators," *Selected Topics in Quantum Electronics, IEEE Journal of*, vol. 6, pp. 1325–1331, Nov 2000.

[12] T. Yamamoto, T. Komukai, K. Suzuki, and A. Takada, "Spectrally flattened phase-locked multi-carrier light generator with phase modulators and chirped fibre Bragg grating," *Electronics Letters*, vol. 43, pp. 1040–1042, September 2007.

[13] M. Kourogi, K. Nakagawa, and M. Ohtsu, "Wide-span optical frequency comb generator for accurate optical frequency difference measurement," *Quantum Electronics, IEEE Journal of*, vol. 29, no. 10, pp. 2693–2701, 1993.

[14] D. Armani, T. Kippenberg, S. Spillane, and K. Vahala, "Ultra-high-Q toroid microcavity on a chip," *Nature*, vol. 421, no. 6926, pp. 925–928, 2003.

[15] P. Del'Haye, A. Schliesser, O. Arcizet, T. Wilken, R. Holzwarth, and T. Kippenberg, "Optical frequency comb generation from a monolithic microresonator," *Nature*, vol. 450, no. 7173, pp. 1214–1217, 2007.

[16] I. H. Agha, Y. Okawachi, M. A. Foster, J. E. Sharping, and A. L. Gaeta, "Four-wave-mixing parametric oscillations in dispersion-compensated high-Q silica microspheres," *Phys. Rev. A*, vol. 76, p. 043837, Oct 2007.

[17] P. Del'Haye, O. Arcizet, A. Schliesser, R. Holzwarth, and T. J. Kippenberg, "Full stabilization of a microresonator-based optical frequency comb," *Phys. Rev. Lett.*, vol. 101, p. 053903, Jul 2008.

[18] L. Razzari, D. Duchesne, M. Ferrera, R. Morandotti, S. Chu, B. Little, and D. Moss, "CMOS-compatible integrated optical hyper-parametric oscillator," *Nature Photonics*, vol. 4, no. 1, pp. 41–45, 2009.

[19] P. Del'Haye, T. Herr, E. Gavartin, M. L. Gorodetsky, R. Holzwarth, and T. J. Kippenberg, "Octave spanning tunable frequency comb from a microresonator," *Phys. Rev. Lett.*, vol. 107, p. 063901, Aug 2011.

[20] A. A. Savchenkov, A. B. Matsko, V. S. Ilchenko, I. Solomatine, D. Seidel, and L. Maleki, "Tunable optical frequency comb with a crystalline whispering gallery mode resonator," *Phys. Rev. Lett.*, vol. 101, p. 093902, Aug 2008.

[21] I. S. Grudinin, N. Yu, and L. Maleki, "Generation of optical frequency combs with a CaF_2 resonator," *Opt. Lett.*, vol. 34, pp. 878–880, Apr 2009.

[22] A. A. Savchenkov, A. B. Matsko, W. Liang, V. S. Ilchenko, D. Seidel, and L. Maleki, "Kerr combs with selectable central frequency," *Nature Photonics*, vol. 5, no. 5, pp. 293–296, 2011.

[23] W. Liang, A. A. Savchenkov, A. B. Matsko, V. S. Ilchenko, D. Seidel, and L. Maleki, "Generation of near-infrared frequency combs from a MgF_2 whispering gallery mode resonator," *Opt. Lett.*, vol. 36, pp. 2290–2292, Jun 2011.

[24] C. Wang, T. Herr, P. Del'Haye, A. Schliesser, J. Hofer, R. Holzwarth, T. Hänsch, N. Picqué, and T. Kippenberg, "Mid-infrared optical frequency combs at 2.5 μm based on crystalline microresonators," *Nature communications*, vol. 4, p. 1345, 2013.

[25] I. S. Grudinin, L. Baumgartel, and N. Yu, "Frequency comb from a microresonator with engineered spectrum," *Opt. Express*, vol. 20, pp. 6604–6609, Mar 2012.

[26] S. B. Papp and S. A. Diddams, "Spectral and temporal characterization of a fused-quartz-microresonator optical frequency comb," *Phys. Rev. A*, vol. 84, p. 053833, Nov 2011.

[27] J. S. Levy, A. Gondarenko, M. A. Foster, A. C. Turner-Foster, A. L. Gaeta, and M. Lipson, "Cmos-compatible multiple-wavelength oscillator for on-chip optical interconnects," *Nature Photonics*, vol. 4, no. 1, pp. 37–40, 2009.

[28] F. Ferdous, H. Miao, D. Leaird, K. Srinivasan, J. Wang, L. Chen, L. Varghese, and A. Weiner, "Spectral line-by-line pulse shaping of an on-chip microresonator frequency comb characterization," *Nature Photonics*, vol. 5, pp. 770–776, 2011.

[29] M. A. Foster, J. S. Levy, O. Kuzucu, K. Saha, M. Lipson, and A. L. Gaeta, "Silicon-based monolithic optical frequency comb source," *Opt. Express*, vol. 19, pp. 14233–14239, Jul 2011.

[30] T. Herr, K. Hartinger, J. Riemensberger, C. Wang, E. Gavartin, R. Holzwarth, M. Gorodetsky, and T. Kippenberg, "Universal formation dynamics and noise of Kerr-frequency combs in microresonators," *Nature Photonics*, vol. 6, no. 7, pp. 480–487, 2012.

[31] Y. Okawachi, K. Saha, J. S. Levy, Y. H. Wen, M. Lipson, and A. L. Gaeta, "Octave-spanning frequency comb generation in a silicon nitride chip," *Opt. Lett.*, vol. 36, pp. 3398–3400, Sep 2011.

[32] T. Kippenberg, R. Holzwarth, and S. Diddams, "Microresonator-based optical frequency combs," *Science*, vol. 332, no. 6029, pp. 555–559, 2011.

[33] J. Leuthold, C. Koos, and W. Freude, "Nonlinear silicon photonics," *Nature Photonics*, vol. 4, no. 8, pp. 535–544, 2010.

[34] D. J. Moss, R. Morandotti, A. L. Gaeta, and M. Lipson, "New CMOS-compatible platforms based on silicon nitride and hydex for nonlinear optics," *Nature Photonics*, vol. 7, no. 8, pp. 597–607, 2013.

[35] K. Saha, Y. Okawachi, B. Shim, J. S. Levy, R. Salem, A. R. Johnson, M. A. Foster, M. R. E. Lamont, M. Lipson, and A. L. Gaeta, "Modelocking and femtosecond pulse generation in chip-based frequency combs," *Opt. Express*, vol. 21, pp. 1335–1343, Jan 2013.

[36] P.-H. Wang, F. Ferdous, H. Miao, J. Wang, D. E. Leaird, K. Srinivasan, L. Chen, V. Aksyuk, and A. M. Weiner, "Observation of correlation between route to formation, coherence, noise, and communication performance of Kerr combs," *Opt. Express*, vol. 20, pp. 29284–29295, Dec 2012.

[37] P.-H. Wang, Y. Xuan, L. Fan, L. T. Varghese, J. Wang, Y. Liu, X. Xue, D. E. Leaird, M. Qi, and A. M. Weiner, "Drop-port study of microresonator frequency combs: power transfer, spectra and time-domain characterization," *Opt. Express*, vol. 21, pp. 22441–22452, Sep 2013.

[38] T. Herr, V. Brasch, J. Jost, C. Wang, N. Kondratiev, M. Gorodetsky, and T. Kippenberg, "Temporal solitons in optical microresonators," *Nature Photonics*, vol. 8, no. 2, pp. 145–152, 2014.

[39] A. Coillet, I. Balakireva, R. Henriet, K. Saleh, L. Larger, J. Dudley, C. Menyuk, and Y. Chembo, "Azimuthal turing patterns, bright and dark cavity solitons in kerr combs generated with whispering-gallery-mode resonators," *Photonics Journal, IEEE*, vol. 5, pp. 6100409–6100409, Aug 2013.

[40] T. Herr, V. Brasch, J. D. Jost, I. Mirgorodskiy, G. Lihachev, M. L. Gorodetsky, and T. J. Kippenberg, "Mode spectrum and temporal soliton formation in optical microresonators," *Phys. Rev. Lett.*, vol. 113, p. 123901, Sep 2014.

[41] J. Li, H. Lee, T. Chen, and K. J. Vahala, "Low-pump-power, low-phase-noise, and microwave to millimeter-wave repetition rate operation in microcombs," *Phys. Rev. Lett.*, vol. 109, p. 233901, Dec 2012.

[42] F. Ferdous, H. Miao, P.-H. Wang, D. E. Leaird, K. Srinivasan, L. Chen, V. Aksyuk, and A. M. Weiner, "Probing coherence in microcavity frequency combs via optical pulse shaping," *Opt. Express*, vol. 20, pp. 21033–21043, Sep 2012.

[43] U. Koren, T. Koch, B. Miller, G. Eisenstein, and R. H. Bosworth, "Wavelength division multiplexing light source with integrated quantum well tunable lasers and optical amplifiers," *Applied Physics Letters*, vol. 54, no. 21, pp. 2056–2058, 1989.

[44] A. W. Fang, H. Park, O. Cohen, R. Jones, M. J. Paniccia, and J. E. Bowers, "Electrically pumped hybrid AlGaInAs-silicon evanescent laser," *Opt. Express*, vol. 14, pp. 9203–9210, Oct 2006.

[45] J. Levy, K. Saha, Y. Okawachi, M. Foster, A. Gaeta, and M. Lipson, "High-performance silicon-nitride-based multiple-wavelength source," *Photonics Technology Letters, IEEE*, vol. 24, pp. 1375–1377, Aug 2012.

[46] J. Pfeifle, V. Brasch, M. Lauermann, Y. Yu, D. Wegner, T. Herr, K. Hartinger, P. Schindler, J. Li, D. Hillerkuss, R. Schmogrow, C. Weimann, R. Holzwarth, W. Freude, J. Leuthold, T. J. Kippenberg, and C. Koos, "Coherent terabit communications with microresonator kerr frequency combs," *Nature photonics*, vol. 8, no. 5, pp. 375–380, 2014.

[47] Z. Jiang, C.-B. Huang, D. E. Leaird, and A. M. Weiner, "Optical arbitrary waveform processing of more than 100 spectral comb lines," *Nature Photonics*, vol. 1, pp. 463–467, 2007.

[48] S. Shapiro and D. Auston, *Ultrashort light pulses: picosecond techniques and applications*. Topics in applied physics, Springer-Verlag, 1984.

[49] A. Weiner, *Ultrafast Optics*. Wiley Series in Pure and Applied Optics, John Wiley & Sons, 2009.

[50] D. V. Strekalov and N. Yu, "Generation of optical combs in a whispering gallery mode resonator from a bichromatic pump," *Phys. Rev. A*, vol. 79, p. 041805, Apr 2009.

[51] W. Liang, V. S. Ilchenko, A. A. Savchenkov, A. B. Matsko, D. Seidel, and L. Maleki, "Passively mode-locked raman laser," *Phys. Rev. Lett.*, vol. 105, p. 143903, Sep 2010.

[52] T. Barwicz, M. Popović, P. Rakich, M. Watts, H. Haus, E. Ippen, and H. Smith, "Microring-resonator-based add-drop filters in SiN: fabrication and analysis," *Opt. Express*, vol. 12, pp. 1437–1442, Apr 2004.

[53] Z. Qiang, W. Zhou, and R. A. Soref, "Optical add-drop filters based on photoniccrystal ring resonators," *Opt. Express*, vol. 15, pp. 1823–1831, Feb 2007.

[54] B. Little, S. Chu, H. Haus, J. Foresi, and J.-P. Laine, "Microring resonator channel dropping filters," *Lightwave Technology, Journal of*, vol. 15, pp. 998–1005, Jun 1997.

[55] S. Xiao, M. H. Khan, H. Shen, and M. Qi, "Modeling and measurement of losses in silicon-on-insulator resonators and bends," *Opt. Express*, vol. 15, pp. 10553–10561, Aug 2007.

[56] J. Wang, J. C. Wirth, Y. Xuan, D. E. Leaird, A. M. Weiner, and M. Qi, "Far-field polarization characterization of the fundamental modes of a strip silicon waveguide," *Opt. Lett.*, vol. 38, pp. 4785–4788, Nov 2013.

[57] J. Čtyrokỳ, I. Richter, and M. Šiňor, "Dual resonance in a waveguide-coupled ring microresonator," *Optical and quantum electronics*, vol. 38, no. 9-11, pp. 781–797, 2006.

[58] B. E. Little, J.-P. Laine, and S. T. Chu, "Surface-roughness-induced contradirectional coupling in ring and disk resonators," *Opt. Lett.*, vol. 22, pp. 4–6, Jan 1997.

[59] S. Johnson and J. Joannopoulos, "Block-iterative frequency-domain methods for maxwell's equations in a planewave basis," *Opt. Express*, vol. 8, pp. 173–190, Jan 2001.

[60] T. Carmon, L. Yang, and K. Vahala, "Dynamical thermal behavior and thermal self-stability of microcavities," *Opt. Express*, vol. 12, pp. 4742–4750, Oct 2004.

[61] M. Ebrahimzadeh, G. A. Turnbull, T. J. Edwards, D. J. M. Stothard, I. D. Lindsay, and M. H. Dunn, "Intracavity continuous-wave singly resonant optical parametric oscillators," *J. Opt. Soc. Am. B*, vol. 16, pp. 1499–1511, Sep 1999.

[62] F. G. Colville, M. H. Dunn, and M. Ebrahimzadeh, "Continuous-wave, singly resonant, intracavity parametric oscillator," *Opt. Lett.*, vol. 22, pp. 75–77, Jan 1997.

[63] Y. K. Chembo and N. Yu, "Modal expansion approach to optical-frequency-comb generation with monolithic whispering-gallery-mode resonators," *Phys. Rev. A*, vol. 82, p. 033801, Sep 2010.

[64] F. Monifi, Ş. K. Özdemir, and L. Yang, "Tunable add-drop filter using an active whispering gallery mode microcavity," *Applied Physics Letters*, vol. 103, no. 18, p. 181103, 2013.

[65] S. A. Miller, Y. Okawachi, S. Ramelow, K. Luke, A. Dutt, A. Farsi, A. L. Gaeta, and M. Lipson, "Tunable frequency combs based on dual microring resonators," *Opt. Express*, vol. 23, pp. 21527–21540, Aug 2015.

[66] X. Xue, Y. Xuan, Y. Liu, P.-H. Wang, S. Chen, J. Wang, D. E. Leaird, M. Qi, and A. M. Weiner, "Mode-locked dark pulse Kerr combs in normal-dispersion microresonators," *Nature Photonics*, vol. 9, no. 9, pp. 594–600, 2015.

[67] O. Arcizet, A. Schliesser, P. DelHaye, R. Holzwarth, and T. J. Kippenberg, "Optical frequency comb generation in monolithic microresonators," *Practical Applications of Microresonators in Optics and Photonics, AB Matsko, ed.(CRC Press, 2009)*, 2009.

[68] A. A. Savchenkov, A. B. Matsko, D. Strekalov, M. Mohageg, V. S. Ilchenko, and L. Maleki, "Low threshold optical oscillations in a whispering gallery mode CaF_2 resonator," *Phys. Rev. Lett.*, vol. 93, p. 243905, Dec 2004.

[69] A. B. Matsko, A. A. Savchenkov, and L. Maleki, "Normal group-velocity dispersion Kerr frequency comb," *Opt. Lett.*, vol. 37, pp. 43–45, Jan 2012.

[70] A. A. Savchenkov, A. B. Matsko, W. Liang, V. S. Ilchenko, D. Seidel, and L. Maleki, "Kerr frequency comb generation in overmoded resonators," *Opt. Express*, vol. 20, pp. 27290–27298, Nov 2012.

[71] Y. Liu, Y. Xuan, X. Xue, P.-H. Wang, S. Chen, A. J. Metcalf, J. Wang, D. E. Leaird, M. Qi, and A. M. Weiner, "Investigation of mode coupling in normal-dispersion silicon nitride microresonators for Kerr frequency comb generation," *Optica*, vol. 1, pp. 137–144, Sep 2014.

[72] X. Xue, Y. Xuan, P.-H. Wang, Y. Liu, D. E. Leaird, M. Qi, and A. M. Weiner, "Normal-dispersion microcombs enabled by controllable mode interactions," *Laser & Photonics Reviews*, vol. 9, no. 4, pp. L23–L28, 2015.

[73] A. M. Pérez, C. Santiago, F. Renero, and C. Zuñiga, "Optical properties of amorphous hydrogenated silicon nitride thin films," *Optical Engineering*, vol. 45, no. 12, pp. 123802–123802, 2006.

[74] H.-T. Shang, "Chromatic dispersion measurement by white-light interferometry on metre-length single-mode optical fibres," *Electronics Letters*, vol. 17, pp. 603–605, August 1981.

[75] J. Li, H. Lee, K. Y. Yang, and K. J. Vahala, "Sideband spectroscopy and dispersion measurement in microcavities," *Opt. Express*, vol. 20, pp. 26337–26344, Nov 2012.

[76] P. Del'Haye, O. Arcizet, M. Gorodetsky, R. Holzwarth, and T. Kippenberg, "Frequency comb assisted diode laser spectroscopy for measurement of microcavity dispersion," *Nature Photonics*, vol. 3, no. 9, pp. 529–533, 2009.

[77] C.-C. Chang, H. P. Sardesai, and A. M. Weiner, "Dispersion-free fiber transmission for femtosecond pulses by use of a dispersion-compensating fiber and a programmable pulse shaper," *Opt. Lett.*, vol. 23, pp. 283–285, Feb 1998.

[78] V. Brasch, M. Geiselmann, T. Herr, G. Lihachev, M. H. P. Pfeiffer, M. L. Gorodetsky, and T. J. Kippenberg, "Photonic chip–based optical frequency comb using soliton cherenkov radiation," *Science*, vol. 351, no. 6271, pp. 357–360, 2016.

[79] Y. K. Chembo and C. R. Menyuk, "Spatiotemporal Lugiato-Lefever formalism for Kerr-comb generation in whispering-gallery-mode resonators," *Phys. Rev. A*, vol. 87, p. 053852, May 2013.

[80] P. Del'Haye, K. Beha, S. B. Papp, and S. A. Diddams, "Self-injection locking and phase-locked states in microresonator-based optical frequency combs," *Phys. Rev. Lett.*, vol. 112, p. 043905, Jan 2014.

[81] A. B. Matsko, A. A. Savchenkov, W. Liang, V. S. Ilchenko, D. Seidel, and L. Maleki, "Mode-locked kerr frequency combs," *Opt. Lett.*, vol. 36, pp. 2845–2847, Aug 2011.

[82] X. Yi, Q.-F. Yang, K. Y. Yang, M.-G. Suh, and K. Vahala, "Soliton frequency comb at microwave rates in a high-q silica microresonator," *Optica*, vol. 2, pp. 1078–1085, Dec 2015.

[83] M. Karpov, H. Guo, A. Kordts, V. Brasch, M. Pfeiffer, M. Zervas, M. Geiselmann, and T. J. Kippenberg, "Raman induced soliton self-frequency shift in microresonator kerr frequency combs," *arXiv preprint arXiv:1506.08767*, 2015.

[84] M. H. P. Pfeiffer, A. Kordts, V. Brasch, M. Zervas, M. Geiselmann, J. D. Jost, and T. J. Kippenberg, "Photonic damascene process for integrated high-q microresonator based nonlinear photonics," *Optica*, vol. 3, pp. 20–25, Jan 2016.

[85] L. A. Lugiato and R. Lefever, "Spatial dissipative structures in passive optical systems," *Phys. Rev. Lett.*, vol. 58, pp. 2209–2211, May 1987.

[86] S. Coen, H. G. Randle, T. Sylvestre, and M. Erkintalo, "Modeling of octave-spanning Kerr frequency combs using a generalized mean-field Lugiato-Lefever model," *Opt. Lett.*, vol. 38, pp. 37–39, Jan 2013.

[87] J. Li, H. Lee, T. Chen, and K. J. Vahala, "Low-pump-power, low-phase-noise, and microwave to millimeter-wave repetition rate operation in microcombs," *Phys. Rev. Lett.*, vol. 109, p. 233901, Dec 2012.

[88] J. A. Jaramillo-Villegas, X. Xue, P.-H. Wang, D. E. Leaird, and A. M. Weiner, "Deterministic single soliton generation and compression in microring resonators avoiding the chaotic region," *Opt. Express*, vol. 23, pp. 9618–9626, Apr 2015.

[89] A. Grudinin, D. Richardson, and D. Payne, "Energy quantisation in figure eight fibre laser," *Electronics Letters*, vol. 28, pp. 67–68, Jan 1992.

[90] M. Karpov, H. Guo, E. Lucas, A. Kordts, M. Pfeiffer, G. Lichachev, V. Lobanov, M. Gorodetsky, and T. Kippenberg, "Universal dynamics and controlled switching of dissipative kerr solitons in optical microresonators," *arXiv preprint arXiv:1601.05036*, 2016.

[91] M. R. E. Lamont, Y. Okawachi, and A. L. Gaeta, "Route to stabilized ultrabroadband microresonator-based frequency combs," *Opt. Lett.*, vol. 38, pp. 3478–3481, Sep 2013.

[92] H. Zhou, S.-W. Huang, Y. Dong, M. Liao, K. Qiu, and C. W. Wong, "Stability and intrinsic fluctuations of dissipative cavity solitons in kerr frequency microcombs," *Photonics Journal, IEEE*, vol. 7, pp. 1–13, June 2015.

[93] C. Milián, A. V. Gorbach, M. Taki, A. V. Yulin, and D. V. Skryabin, "Solitons and frequency combs in silica microring resonators: Interplay of the raman and higher-order dispersion effects," *Phys. Rev. A*, vol. 92, p. 033851, Sep 2015.

[94] R. Drever, J. L. Hall, F. Kowalski, J. Hough, G. Ford, A. Munley, and H. Ward, "Laser phase and frequency stabilization using an optical resonator," *Applied Physics B*, vol. 31, no. 2, pp. 97–105, 1983.

[95] A. Ankiewicz and N. Akhmediev, *Dissipative Solitons: From Optics to Biology and Medicine*. Springer, 2008.

[96] Y. H. Wen, M. R. Lamont, I. M. Kloumann, S. H. Strogatz, and A. L. Gaeta, "Self-organization in soliton modelocked parametric frequency combs," *arXiv preprint arXiv:1412.0119*, 2014.

[97] C. Bao and C. Yang, "Mode-pulling and phase-matching in broadband kerr frequency comb generation," *J. Opt. Soc. Am. B*, vol. 31, pp. 3074–3080, Dec 2014.

[98] P. DelHaye, A. Coillet, W. Loh, K. Beha, S. B. Papp, and S. A. Diddams, "Phase steps and resonator detuning measurements in microresonator frequency combs," *Nature communications*, vol. 6, p. 5668, 2015.

VITA

VITA

Pei-Hsun Wang received the B.S. degree in electrical engineering from National Chiao Tung university, Hsinchu, Taiwan, in 2007, and the M.S. degree in photonics and optoelectronics from National Taiwan University, Taipei, Taiwan, in 2009. He is currently pursuing a Ph.D. in electrical and computer engineering at Purdue University, where he conducts research in on-chip frequency comb generation. From 2011-2016, he worked as a Graduate Research Assistant in the Ultrafast Optics and Optical Fiber Communications group at Purdue. Since 2009, he has already coauthored 9 SCI journal papers and 20 conference contributions.

Pei-Hsun Wang is a member of both OSA and IEEE, and serves as a reviewer for Optics Express and Scientific Report. He received several awards for his work in ultrafast optics area. Pei-Hsun Wang is selected as a recipient of Scholarship of the Phi Tau Phi Scholastic Honor Society, Mid-America Chapter, USA, in 2013, Government Scholarship to Study Abroad by the Ministry of Education, Taiwan, in 2012, and the Outstanding Thesis Award from the Physical Society of the Republic of China, Taiwan, in 2009. His research interests include microresonator-based optical frequency combs, ultrafast optics, high-speed optical communication, time-domain signal processing, and silicon photonics design.